学位論文（要約）

Bulk composition of the Moon constrained by the conditions of anorthosite crust formation

(斜長岩質地殻形成条件から制約する月バルク組成)

平成２５年１２月博士（理学）申請

東京大学 大学院理学系研究科 地球惑星科学専攻

酒井　理紗

Abstract

A basic understanding of the inner structure, chemical composition and thermal history of the Moon has been provided from the extensive explorations, including remote sensing and analysis of Apollo samples and lunar meteorites. In particular, the crust of the Moon has been investigated in detail; the lunar highland is inferred to be the ancient anorthosite crust with 35-55 km thickness, which is thought to have been formed by large scale differentiation of a totally molten Moon named as the lunar magma ocean (LMO). In LMO models proposed so far, mafic minerals such as olivine and pyroxene crystallized at first and settled down to form the mantle. After 70-80% of the LMO had crystallized, plagioclase became a liquidus phase and would have been floated in the melt because of the low density. LMO models have been widely supported by geochemical observation such as the chronology of the crustal rocks, the complementarity of Eu anomaly between highland rocks and mare basalts, and the existence of KREEP rocks rich in incompatible elements. The existence of LMO is consistent with the giant impact origin of the Moon by a collision between a protoplanet and the proto Earth and formation of the Moon from the ejecta in the completely molten state at the beginning. Although the giant impact origin of the Moon has become a consensus among most of the researchers, detailed geophysical and geochemical processes still remain unknown, such as chemical evolution during the lunar formation and the efficiency of the crystal separation in the cooling LMO, which is mostly due to a large uncertainty in the bulk composition of the Moon. Previous workers have disputed whether the chemical composition of the bulk Moon is similar to or richer in FeO and/or Al_2O_3 contents than those of the Earth. The FeO and Al_2O_3 contents play a key role in the evolution of the Moon; the FeO content affects density and viscosity of melt, which control separation of minerals from the LMO, and chemical composition of olivine and pyroxenes. The Al_2O_3 content is also crucial in evolution of the LMO, because it affects the stability of anorthite, the major constituent of the highland crust. In this study, we will estimate the bulk composition of the Moon by developing a differentiation model through thermodynamic and fluid dynamic consideration and by

constraining relevant parameters to reproduce the physical and chemical conditions to form the observed anorthosite crust.

The model we developed is a polybaric incremental fractionation model with initial compositions and the efficiency of crystal separation as parameters, the latter being represented by the limit fraction of suspended crystals X_{scfl}. The essential part of the model is thermodynamic equilibrium among melt and crystallizing phases, and was calculated with MELTS/pMELTS program. The initial bulk composition of the LMO was varied by modifying composition of bulk silicate Earth (BSE) with variable FeO and refractory element (Al_2O_3 and CaO) contents. Previous models on LMO differentiation are classified into two types in terms of crystal differentiation: fractional crystallization all through the crystallization process and equilibrium crystallization followed by fractional crystallization. The actual differentiation process, however, should have been somewhere in between maximum fractional crystallization and equilibrium crystallization, although it is difficult to know the actual efficiency of crystal accumulation. In this study, a single parameter has been introduced to reproduce the efficiency of crystal separation from LMO, in order to model chemical evolution due to differentiation.

The model calculation showed important knowledge of the differentiation of the LMO. A general crystallization sequence before anorthite crystallization is olivine followed by orthopyroxene for the various bulk compositions of the LMO. Clinopyroxene and/or spinel, which contain large amounts of refractory elements such as Al_2O_3 and CaO, join the crystallization sequence particularly for a melt rich in Al_2O_3. The chemical composition of the LMO at the first appearance of anorthite as a liquidus phase is strongly dependent on the initial FeO content. Higher initial abundance of FeO results in an increase of FeO content in the residual melt of anorthite saturation, which remarkably increases the density of melt. The degree of LMO solidification before the anorthite appearance is non-linearly related to the initial Al_2O_3 content, which is lowest for melt with the initial Al_2O_3 content ~1.5 times of BSE and increases for the higher and lower values of the initial Al_2O_3. This is because the Al_2O_3 content of melt at the anorthite appearance increases with increasing initial Al_2O_3 content up to ~1.5 times BSE and decreases for further increase of the initial Al_2O_3 content owing to the enhancement of spinel crystallization. The limit fraction of suspended crystals, X_{scfl}, does not significantly affect the chemical composition and physical properties of

the residual melt at the time of anorthite appearance except for the low initial Al_2O_3 content (~BSE) and the low degree of LMO solidification except for the intermediate Al_2O_3 content (1.5-2.0 times of BSE).

The calculated LMO compositions at the appearance of anorthite are examined if they satisfy the following condition; (1) the mass of anorthite crystallized from the residual melt is abundant enough to form the observed crustal thickness, (2) the density and viscosity of the melt are appropriate to segregate anorthite from a turbulent LMO, (3) the Mg# (= molar Mg/(Mg+Fe)) of mafic minerals crystallized with anorthite is consistent with that observed in the lunar highland rocks, and (4) the rare earth element (REE) composition of the LMO is consistent with that observed in the parent magma of lunar highland rocks.

The lower limit of the FeO content is constrained by the condition for anorthite separation in a turbulent LMO, which lies ~1.2 to 1.5 times of BSE being almost independent of the initial Al_2O_3. Density contrast between anorthite and melt has the fundamental importance on the anorthite separation from the LMO, and consequently, FeO plays a critical role. The upper limit of the FeO content is defined by the condition to be consistent with the observed Mg# of mafic minerals in anorthosite. The upper limit is strongly dependent on the initial Al_2O_3 content and X_{scfl} for the cases with low Al_2O_3 content. The lower and upper limits of the initial Al_2O_3 content are constrained by the observed thickness of the crust as 0.8-2.3 times of BSE, which is very wide. The tighter upper limit of initial Al_2O_3 content is constrained by the rare earth element (REE) composition of plagioclase in ferroan anorthosite (FAN rocks), which is 1.1 times of BSE. The REE patterns estimated for the parent magmas of FAN rocks exhibit slight enrichment of light ERRs relative to the middle REEs, which suggests limited fractionation of clinopyroxene from the LMO.

Combining all the constraints, a plausible range of the FeO and Al_2O_3 contents of the initial LMO is narrowed down to a region 1.2-1.8 times of BSE in FeO and 0.8-1.1 ×BSE in Al_2O_3. This estimate is based on extensive data available so far from geophysical and geochemical observations of the lunar crust, which is strongly linked to the global LMO differentiation. Therefore, it is highly reliable being independent of local or late-stage events took place after the LMO solidification. The constrained LMO composition, rich in FeO and BSE-like in Al_2O_3, implies that the most of the lunar disk materials were originated from the impactor because of

evaporation/condensation-related fractionation in the disk orbiting around the earth cannot explain the chemical features. The estimated bulk composition of the Moon lies between those of the Earth and Mars, which is rather closer to the Earth, and would imply that the impactor that formed the Moon was orbiting between the Earth and Mars.

Acknowledgements

First of all I wish to express my special gratitude to my supervisor Professor Hiroko Nagahara for her continuous supports and helpful advices. I am positively influenced by her way of thinking for science. Her instructive and appropriate guidance always motivate me and improved my study.

Secondly, I am extremely grateful to Professor Kazuhito Ozawa, who has supported me throughout my postgraduate research with his fruitful advices and great knowledge about petrology, fluid dynamics, and magmatism. Without their lots of help, this thesis would not be written.

I sincerely thank Professor emeritus Ikuo Kushiro of Univ. of Tokyo for his expert knowledge and comments on lunar science. He provides the opportunity for me to study in this field when I was an undergraduate student.

I am deeply grateful to Dr. Shogo Tachibana for many valuable comments. His appropriate advices and continuous encouragements always motivate me to advance my research.

I wish to thank Prof. Yutaka Abe of Univ. of Tokyo for many constructive comments and fruitful discussions for geophysics and thermodynamics of magma ocean.

I am grateful to Prof. Takehiro Koyaguchi of Univ. of Tokyo for critical and insightful comments improved this dissertation greatly.

I appreciate many constructive comments and fruitful discussions for improving this dissertation from Prof. Seiji Sugita of Univ. of Tokyo.

I wish to thank Dr. Makiko Ohtake and Dr. Yuzuru Karouji of Japan Aerospace Exploration Agency (JAXA) for many valuable comments for improving this study.

I wish to thank Dr. Tomokatsu Morota, Dr. Yoshiaki Ishihara, Dr. Makoto Hareyama, Dr. Shunichi Kamata, Dr. Hiroshi Nagaoka, and Mr. Yuichiro Cho and the other members of the research group on Formation and evolution of lunar crust for constructive comments and fruitful discussions with them.

Special thanks go to Dr. Aki Takigawa of Kyoto Univ. who is always willing to help and giver her best suggestions for years. Her continuous supports and appropriate advices encourage me to continue and improve my research.

I would also like to thank Dr. Eiichi Tajika, Dr. Masahiro Ikoma, Dr. Hidenori Genda, Dr. Tsuyoshi Iizuka, Dr. Takashi Mikouchi, Dr. Keiko Hamano, and the other members in L-seminar and Planet differentiation seminar for their constructive comments on this study.

I am grateful to all colleagues including 720 members, Mr. Kouki Idehara, Mr. Taichi Nozu, Mr. Takanori Kodama, Ms. Ayaka Tokumaru, Ms. Hiroko Suzuki, Ms. Yukari Miyazaki, Ms. Ayako Hori, Mr. Syunsuke Kurokawa, and Mr. Hikaru Nitta for their understanding, encouragements, and great supports.

Finally, I deeply thank my parents, Takehisa and Mariko, my brother Takeru, and my husband Ryoji for their daily supports.

The freely available software package MELTS/pMELTS and Adiabat_1ph (http://melts.ofm-research.org/ and http://magmasource.caltech.edu/adiabat_1ph/, respectively) is used for large parts of Chapter 3. I thank the Japan Society for the Promotion of Science (JSPS) for awarding me (#9425) a Research Fellowship for Young Scientists.

Table of Contents

Chapter 1. Introduction

The fundamental objective of lunar science is to reveal the origin and evolution of a planet other than the Earth and to understand the peculiarity and generality of the Earth. The Moon preserves records of early geologic events on its surface owing to its small size and the absence of atmosphere and ocean, though such records had been erased on the Earth. The origin and evolution of the Moon are fundamental to understand the initial evolution of terrestrial planets and the formation of the Earth-Moon system.

Extensive explorations in the last five decades provided us basic understanding of the interior structure, chemical composition, and thermal history of the Moon. Through combination of remote sensing, surface exploration and sample return, the Apollo missions (1961-1975), provided a general picture of the lunar interior and suggested the concept of a lunar magma ocean (LMO). The discovery of anorthosite in the returned samples led to the concept that a large portion of the Moon was initially molten, and that crystallization of LMO had left mafic cumulates that made up the mantle and anorthosite cumulate that made up the crust by anorthite flotation (Smith et al., 1970; Wood et al., 1970). LMO model is widely supported by geochemical observation such as the chronology of the crustal rocks (Nyquist et al., 1977; Nyquist and Shih, 1992), the complementarity of Eu anomaly between highland rocks and mare basalts (Haskin et al., 1981; Morse, 1982; Ryder, 1982), and the existence of KREEP rocks rich in incompatible elements (Dowty et al., 1976; Shih, 1977; Warren and Wasson, 1979). The Apollo samples have limitation in that they are from particular regions near side of the Moon. Lunar meteorites somewhat overcome the limitation by providing information on various locations of the lunar surface including far-side.

Remote sensing missions of the 1990s, Clementine and Lunar Prospector, for the first time obtained near-global compositional data sets that enabled us to assess the nature of materials on the surface of the Moon. By combining the lunar samples and geophysical constraints by the orbital data, understanding of the interior structure of the Moon has been much improved from the Apollo era. Other remote sensing missions were carried out since 2003: SMART-1 launched by the ESA (Europe) in 2003,

SELENE by JAXA (Japan) in 2007, Chang'e 1 and 2 by China in 2007 and 2010, Chandrayaan-1 by India in 2008, and LRO and GRAIL by NASA (USA) in 2009 and 2011. The accurate and detailed data sets obtained by these explorations has improved the preceding understanding, but raise new questions, particularly about the mineral distribution on the lunar surface, the water content in the Moon, and the thickness of the lunar crust.

The detailed and immense observations from the Apollo samples, remote sensing and meteorites have deepen our understanding on the origin and formation processes of the LMO because the lunar surface and internal structure have a close relation to the LMO as its outcome product. From this point, we sequentially review our current knowledge and questions of the internal structure, the thermal history and the bulk composition of the Moon.

1.1 Internal structure of the Moon

The lunar crust has the most direct evidence for a major differentiation event that took place in the early stage of the Moon. Because the crust is easily accessible by both remote-sensing observations and sample analysis, there are abundant and accurate data about the composition and structure of the lunar crust. These data provides us with the two-dimensional information of lunar crustal surface. Some observations, however, provided information from the deep crust, such as rocks brought to the surface from the depth by impact cratering, and from even the deeper part, such as the seismology by four of the seismometers placed in an approximate equilateral triangle during Apollo missions and the detailed gravitational field of the Moon from recent remote sensing missions.

The surface of the Moon is divided into the area with high albedo called “highland” that is composed of anorthosite and the areas with low albedo called "mare” that is compounded from basaltic lavas and related volcanic rocks (Warren, 1993; Papike et al., 1998). Mare basalts with the formation ages ranging from about 3.16 to 3.8 Ga (summarized by Taylor, 1982; Nyquist and Shih, 1992; Hiesinger et al., 2000) were formed by ancient volcanic eruptions and filled impact basins. They are younger than the highland rocks with formation ages ranging from about 4.3 to 4.5 Ga (e.g. Borg et al., 1999, 2002; Boyet and Carlson, 2007; Nyquist et al., 1995, 2010). The highland rocks, referred to as the pristine igneous rocks, are almost exclusively anorthosite consisting mostly of anorthite (calcic plagioclase, $CaAl_2Si_2O_8$). The pristine igneous rocks are subdivided into four rock types according to their major mineral compositions: the ferroan anorthosite, the magnesian suite rocks, alkali suite, and KREEP basalts (Fig. 1.1.1). The ferroan anorthosite (FAN) is the main component of the crustal rocks whose plagioclase is highly calcic (anorthite content generally > 94) (Korotev, 2000; Wieczorek and Zuber, 2001; Taylor et al., 2006b) and whose mafic silicates, orthopyroxene and olivine, have relatively high Fe/Mg values (Fig. 1.1.1). The FAN rocks are isotopically very primitive and extremely old yielding 4.44-4.54 Ga Sm-Nd ages (Carlson and Lugmair, 1988; Norman et al., 2003; Nyquist et al., 2010). This age range provides strong basis for the inference that crystallization of the FAN rocks is related to the early stage of differentiation of the Moon (Taylor, 1982; Warren,

1990). Rocks belonging to the magnesian suite contain mafic silicate minerals with a wide range of Mg# (= Mg/(Fe+Mg)) from ~0.60 up to ~0.90 and the average value higher than that of FAN rocks, and plagioclase with lower and variable anorthite content (100 xCa/(Ca+Na)) ranging from 80 to 96 and the average lower than that of FAN rocks (Fig. 1.1.1). The alkali suite is a minor rock type, of which Na and K contents are higher than those of the magnesian suite. The rocks of the magnesian suite and alkali suite yield younger ages (Nyquist and Shih, 1992) than the FAN rocks and are inferred to have formed through secondary igneous processes that took place after the initial crustal formation. The KREEP rocks have high concentration of incompatible elements that do not fit into the crystal structure of the major rock-forming minerals. KREEP is an acronym for K (potassium), REE (rare earth elements), and P (phosphorous) along with Th (thorium) and U (uranium). Large regions of the near-side lunar Maria are enriched in these incompatible elements. These characteristics show that the KREEP rocks would have been derive from the last liquid to solidify from entirely molten Moon (see below).

Until recently, the Apollo seismic data were interpreted for estimation of the crustal thickness around the equator in the nearside to be 60 km and global average thickness ~73 km (Taylor, 1982). Recent detailed reanalysis of the Apollo seismic data set and the accurate global remote sensing data of the lunar gravitational field suggest that the average thickness of the crust is 45-60 km (Lognonné et al., 2003; Wieczorek 2006; Ishihara et al., 2009) or 34 km for most recent estimate by GRAIL (Wieczorek et al., 2013).

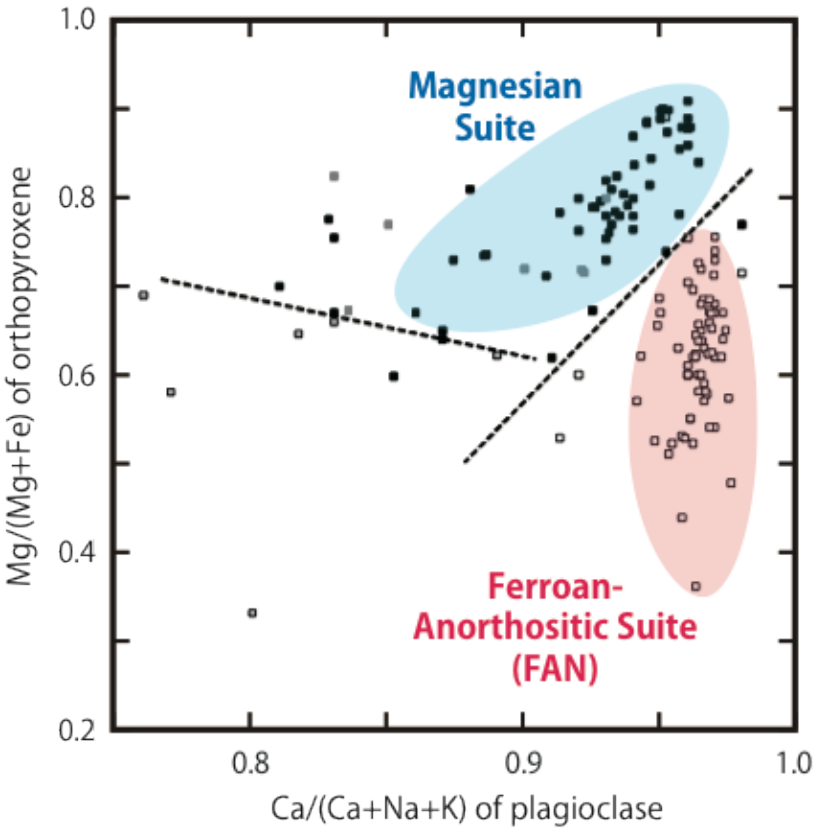

Fig. 1.1.1
Mg/(Mg+Fe) of orthopyroxene plotted against Ca/(Ca+Na+K) (anorthite content) of coexisting plagioclase in lunar crustal igneous rocks. Ferroan-anorthositic suite (FAN) and magnesian suite are identified in the plot. The diagram is modified after Fig. 3.2 of Wieczorek et al. (2006) based on data from Warren (1993) and Papike et al. (1998).

1.2 Initial magmatic evolution: Magma Ocean

1.2.1 *Magma ocean hypothesis and its geochemical evidence*

At the time of the first Apollo sample studies, the lunar highland crust was characterized by the occurrence of anorthositic rocks, composed mostly of calcic plagioclase (anorthite). The occurrence of such anorthite-rich rocks led to the idea that a large-scale differentiation event may have formed the lunar crust by flotation of anorthite from an extensively molten state of the Moon (Smith et al., 1970; Wood et al., 1970). Later dating shows that anorthositic rocks are oldest among the rocks from the highland crust, supporting the inference that the highland crust formation took place during the Moon's early evolution. This is the lunar magma ocean (LMO) hypothesis. The term "magma ocean" was defined as "a global near-surface shell of magma, tens or hundreds of kilometers thick" (Warren, 1985). In this hypothesis, the Moon was almost completely molten from the surface to the depth more than a few hundred kilometers. This hypothesis was also supported by REE data. Rare earth element (REE) pattern of the anorthosites is complementary to that of the mare basalts (Fig. 1.2.1). KREEP basalts, which are older than the mare basalt activity, are highly enriched in REE with a strong negative Eu anomaly (Fig. 1.2.1). Incompatible elements are progressively enriched in the magma as crystallization progressed. These REE data is, therefore, consistent with the model that crystallization and fractionation of the LMO produced mantle with low REE and negative Eu anomaly, crust with high REE and positive Eu anomaly, and extremely REE-enriched final residual melt as KREEP magma that may have been sandwiched between the crust and mantle (Fig. 1.2.1).

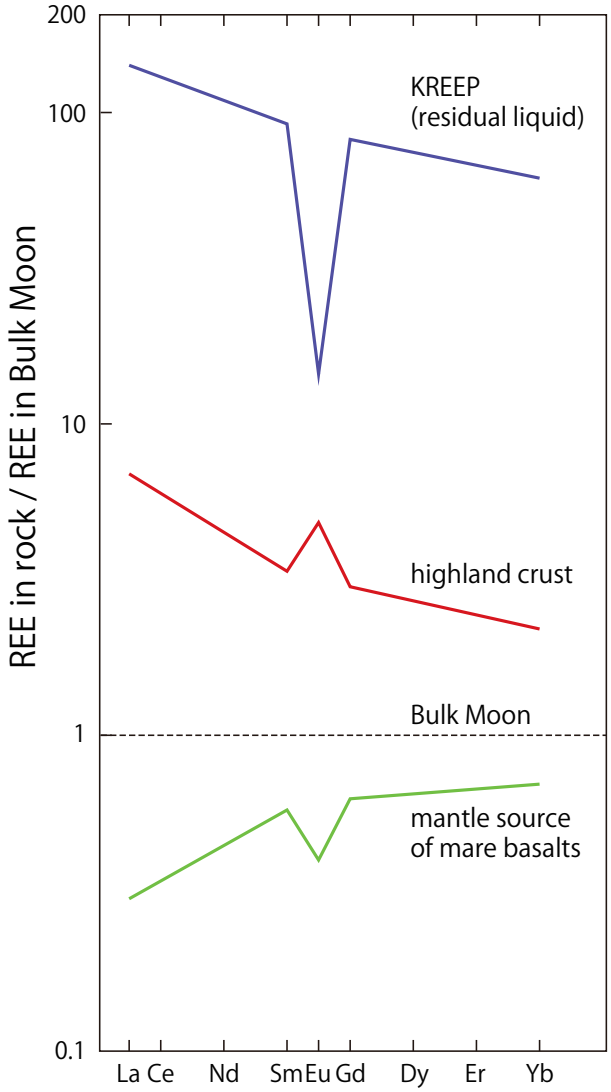

Fig. 1.1.2
Rare earth element (REE) patterns representing three important lunar materials: mantle source of mare basalts, highland crust, and KREEP, normalized by the bulk moon. They show distinctive REE patterns, particularly average concentrations, Eu anomalies, and LREE/HREE ratios. The diagram is modified after Taylor et al. (2006a).

1.2.2 *Thermal structure of a convecting magma ocean*

Although LMO hypothesis assumes that the Moon was extensively molten just after its birth, the depth of LMO has not been constrained well. Solomon and Chaiken (1976) proposed a 500km (about half lunar volume) deep LMO on the basis of little sign of any topographic features of the expansion or contraction, which are expected if LMO was totally molten. In this model, the deeper part of the Moon is composed of undifferentiated material of bulk lunar composition. Warren (1985) and Longhi (2006) proposed a totally molten LMO (~1738 km deep) on the basis that the entirely molten Moon is required to generate the thick anorthosite crust. They argued that the absence of any topographic features for the expansion or contraction is not a useful constraint on the depth of the magma ocean because the liquid free surface may have been retained before anorthite begins to crystallize at the last stage of the cooling LMO (Prichard and Stevenson, 2000; Elkins-Tanton et al., 2011). An entirely molten Moon would be reasonable given the origin of the Moon was by a giant impact as reviewed below.

Convection of LMO is expected to be extremely turbulent because of a very high Rayleigh number and low Prantle number (Tonks and Melosh, 1990). The Rayleigh number is a dimensionless parameter measuring the competition of buoyancy force and viscous resistance. It characterizes the vigor of convection and defined as follows:

$$Ra = \frac{\alpha g (T_{\mathrm{m}} - T_{\mathrm{s}}) L^3}{\kappa \nu},$$

where $\boldsymbol{T_{\mathrm{m}}}$ is the potential temperature of the magma ocean, $\boldsymbol{T_{\mathrm{s}}}$ is the surface temperature, α is the thermal expansion coefficient, $\boldsymbol{g}$ is the gravitational acceleration, $\boldsymbol{L}$ is the depth of convecting cell (LMO), $\boldsymbol{\kappa} = \boldsymbol{k}/\boldsymbol{\rho C_p}$ is the coefficient of thermal diffusivity, and $\boldsymbol{\nu} = \boldsymbol{\eta}/\boldsymbol{\rho}$ is the kinematic viscosity. Additional parameters are: $\boldsymbol{k}$ is the coefficient of thermal conductivity, $\boldsymbol{C_p}$ is the isobaric heat capacity, $\boldsymbol{\rho}$ is the density, and $\boldsymbol{\eta}$ is the dynamic viscosity. The Prantle number is a dimensionless parameter measuring the importance of thermal diffusion in regulating the flow and defined as follows:

$$Pr = \frac{\nu}{\kappa}.$$

Convection with very high Rayleigh numbers and low Prantl number such as those in the magma ocean is called hard turbulence, which is driven by inertial force. Tonks and Melosh (1990) used the turbulent mixing-length theory by Kraichnan (1962) to describe a hard-turbulent LMO regime, where the following relationship is satisfied,

$$Ra^{1/3} \geq 35 Pr^{1/1},$$

which is barely fullfilled for 1 km deep magma chamber but is unconditionally fullfilled for LMOs envisaged above since Ra=$10^{24\text{-}29}$ and Pr~5. Kraichnan (1962) also proposed the relationship between Ra and Nusselt number (Nu= h / h_c), which is the ratio of the convective heat flux at the surface (h) relative to the conductive flux giving the same temperature gradiant across the horizontal boundaries of the system (h_c), as follows:

$$Nu = 0.089 Ra^{1/3}.$$

Spera (1992) made experimental and simulation studies combined with a dimensional analysis, and suggested the relationiship of $Nu \propto \mathrm{Ra}^{2/7}$ rather than the traditional $\mathrm{Nu} \propto \mathrm{Ra}^{1/3}$ scaling. As shown by Spera (1992), calculation of a LMO surface temperature and a cooling rate from the two different scaling laws leads to significantly different results. More experimental work on the relationship between Nu and Ra for convection of a magma ocean with a high Ra is required to further constrain the evolution of a turbulent LMO.

Physical properties of silicate melt control dynamics of a magma ocean and its evolution. The typical values of these parameters by Solomatov (2000) are listed in Table 1.1. Viscosity is of a particularly importance, because viscosity of silicate melt is known to vary in a very broad range for terrestrial magmas. Experimental and theoretical studies suggest that the viscosity of near-liquidus ultramafic silicate melt at low pressure is $\eta \sim 0.1$ Pa s (Bottinga and Weill, 1972; Shaw, 1972; Kushiro, 1986;

Dingwell et al., 2004). Although there are limited experimental data for the viscosity at high-pressures corresponding to the mantle conditions, viscosity of a completely depolymerized melt slightly increases with pressure (Andrade, 1952; Gans, 1972; Sakai et al., 2010). Thus, viscosity of 10^{-1} Pa s may be applied at all the depths of a magma ocean that are at near liquidus temperatures (Solomatov 2000). Viscosity of silicate melt significantly increases by the presence of crystals and the viscosity of the melt-crystal mixture is approximately described by the Einstein-Roscoe equation:

$$\eta = \frac{\eta_l}{(1-\Phi/\Phi_m)^{2.5}},$$

where Φ is the volume fraction of solids, Φ_m is the maximum packing crystal fraction, and η_l is the viscosity of melt without crystals. The value of Φ_m for the close-packed structure of uniform spheres is about 0.74. Experimental studies at high temperatures with a rotational viscometer, however, showed that a crystal network forms at the crystal fraction as low as 30-40 % depending on the composition and the shape of crystals (Marsh, 1981; Rutter and Neumann, 1995; Philpotts and Carroll, 1996; Sato 2005). The above equation suggests that the viscosity becomes sharply infinite when the crystal fraction reaches Φ_m (Solomatov and Stevenson, 1993). This is the important physical aspect of a two-phase system consisting of crystals and silicate melt. In other words, transition from fluid-like behavior to solid-like behavior occurs in a rather narrow range of crystal fraction, which is called the "rheological transition" by Solomatov (2000). At Φ only slightly smaller than Φ_m, viscosity is not much different from that of pure melt, whereas at $\Phi > \Phi_m$, the rheological behavior of magma containing crystals is controlled by the solid viscosity.

During the early stages of crystallization of the magma ocean, the viscosity is small and convection is extremely turbulent. In a vigorously convective system, temperature distribution is nearly adiabatic and isentropic. The equation for an adiabat is given by:

$$\frac{dT}{dP} = \frac{\alpha T}{\rho C_p},$$

where T is temperature, P in pressure, α is the thermal expansion, C_p is the isobaric specific heat, and ρ is the density of melt. The depth range where crystallization progresses in a magma ocean is suggested by the relationship between adiabat and liquidus/solidus temperatures. Tonks and Melosh (1990) discussed that the effect of gravitational acceleration on the slopes of the solidus, liquidus, and adiabatic temperature profiles is an important factor to cause the difference in geochemical evolutionary paths between the Earth and Moon. Solidification of a large igneous body with a large pressure range, such as in the Earth, would begin at the bottom because the steeper slope of the solidus temperature in the pressure-temperature space, which is highly oblique to the slope of the adiabat (Fig. 1.2.2a). In small bodies with small pressure ranges, such as the Moon, nearly entire magma ocean would have an equal crystal fraction, because the adiabat lying between the liquidus and solidus is only slightly gentler than the liquidus and solidus for all depth (Fig. 1.2.2b). The relationship between the liquidus/solidus slopes affects the melt fraction in the two-phase region and thus contour of Φ_m near the rheological transition. The structure of a magma ocean may thus depend significantly on planet size as Tonks and Melosh (1990) noted and discussed. Because of this, it is usually assumed in the previous studies that crystallization took place at all depths of LMO with adiabat slopes lying between the liquidus and solidus (Spera, 1992; Elardo et al., 2011; Elkins-Tanton, 2012).

Table 1.1
Typical values of physical parameters for a lunar magma ocean in the early stage of crystallization adopted from Solomatov (2000). Heat flux is that of the initial LMO in the hard turbulence convection regime.

Thermal expansion, α	5×10^{-5} K^{-1}
Heat capacity, C_p	10^3 J kg^{-1} K^{-1}
Gravitational acceleration, g	1.62 m s^{-2}
Heat Flux, F	5×10^5 J m^{-2} s^{-1}

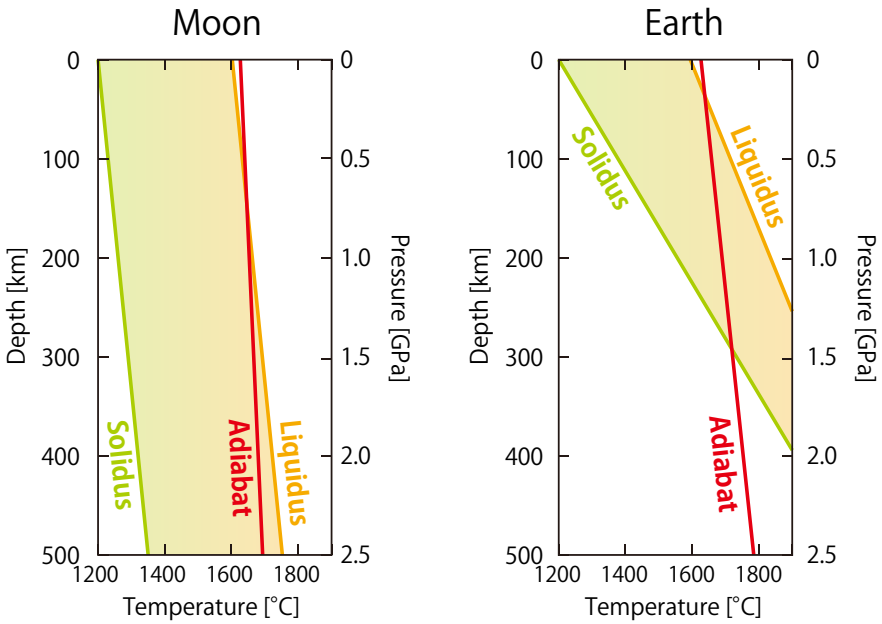

Fig. 1.2.2
Depth variations in degree of melting of magma oceans expected for the Earth (right) and Moon (left) along an adiabat with ~1610°C potential temperature crossing melting regions near the surface of the planets. Steeper liquidi and solidi for the Earth than for the Moon results in the contrasting structure of the magma oceans, because of the difference in size of the planets. This diagram is modified after Elkins-Tanton et al. (2011) and Tonks and Melosh (1990).

1.2.3 *Coupling of physics and chemistry in LMO*

Evolution of LMO is not only highly dependent on bulk LMO composition and heat transportation mechanisms, but also these two aspects are strongly coupled to make its understanding very difficult. Compositional evolution of a crystallizing LMO was modeled based on the thermal and petrological views (Taylor and Jakes, 1974; Longhi 1977, 1981; Taylor, 1982; Snyder et al., 1992; Elardo et al., 2011). Standard scenario adopted in these studies is as follows. Crystallization starts with olivine followed by orthopyroxene ± olivine, and clinopyroxene ± olivine + plagioclase, and the residual melt becomes richer in FeO as crystallization proceeds. After 70-80% of the magma ocean is crystallized, plagioclase becomes a liquidus phase, and it can float in the iron-rich melt because of its low density. The residual melt becomes extremely rich in FeO by further crystallization and incompatible and heat-producing elements is extremely concentrated in the magma ocean when it is crystallized 90%, and it may be sandwiched between the crust and mantle, forming a KREEP-like magma. Dense Ti-bearing phases such as ilmenite may crystallize from this residual melt (Hess and Parmentier, 1995; Van Orman and Grove, 2000). In simple models of magma ocean crystallization, the cumulate phases are sequentially accumulated on the bottom of the magma ocean. Because the mantle cumulates become increasingly rich in FeO with decreasing the depth, the cumulus pile becomes gravitationally unstable and induces global overturn to a stable configuration (Solomon and Longhi, 1977; Snyder et al., 1992; Elkins-Tanton et al., 2011).

Cumulate assemblages in the interior of the Moon and timing of crustal formation, that is, degree of crystallization at the first anorthite appearance as a liquidus phase, predicted by previous models of crystallization of LMO, depend on its initial bulk composition. Variable bulk Al_2O_3 contents of the Moon, for example, result in different cumulate assemblages, (Snyder et al., 1992; Elardo et al., 2011). The initial bulk LMO composition with < 5wt% Al_2O_3 leaves olivine and orthopyroxene as mantle cumulate phases, and plagioclase crystallizes when 70-80 % of the LMO is solidified. If the LMO is richer in Al_2O_3, garnet and spinel join the cumulus phases in addition to olivine and orthopyroxene, and plagioclase appears earlier at ~60 % solidification. The bulk FeO content is also crucial for the formation of the lunar internal structure. The FeO content affects the timing and scale of overturn and the efficiency of the

anorthosite crust formation, because the density of the residual melt and Mg# of the mantle minerals strongly depend on the FeO content of the LMO.

Another important factor to be examined is efficiency of crystal separation (equilibrium versus fractional crystallization). It is difficult to quantitatively evaluate the efficiency of crystal accumulation because it involves physics of crystal transportation and separation coupled with crystallization. Previous models on LMO differentiation are classified into two types with regard to the mode of crystal fractionation: fractional crystallization all through the crystallization process (Taylor and Jakes, 1974; Warren and Wasson, 1979; Longhi, 2003) and equilibrium crystallization up to a certain solidification fraction (e.g., 50-80 %) followed by fractional crystallization (Snyder et al., 1992; Elardo et al., 2011). The latter scheme is based on fluid dynamics of the LMO, which is thought to be too turbulent to allow efficient separation of growing crystals, of which convective velocity is thought to be much larger than effective terminal velocity of crystals (Martin and Nokes, 1989; Tonks and Melosh, 1990). The actual differentiation process should have been somewhere in between maximum fractional crystallization and equilibrium crystallization, which may or may not affect the evolution trends of the LMO. This is not critically examined in previous studies and efficiency of crystal separation is one of the unresolved problems in LMO modeling.

Physics of heat transportation and crystal separation depends on chemical aspect of a LMO, that is, the bulk composition of the Moon. Therefore, a coupled model of geochemistry and fluid dynamics of the cooling LMO is required to understand the evolution of the Moon.

1.3 Origin of the Moon

The Moon has several unique geophysical and geochemical features: (1) small iron core estimated from the low bulk density, (2) depletion of volatile elements, (3) coincidence of the oxygen isotopic composition with the Earth, and (4) the high angular momentum of the Earth-Moon system. A model for the origin and evolution of the Moon should be consistent with these features. Until 1970s, three models had been proposed for the origin of the Moon, all of which well explain one of the above aspects, however, none of them satisfies all of the aspects. The first model, known as the "*Capture theory*", explains that the Moon was formed elsewhere in the solar system and was gravitationally captured by the Earth. This model does not well explain the iron depletion in the bulk Moon and it appeared unlikely because of low probability for capture accidentally. The second model, known as the "*Co-formation theory*", discusses that the Moon was formed from material that had been captured into the orbit around the Earth after the Earth was mostly formed. This model hardly explains both the depletion of iron and the angular momentum of the Earth-Moon system. The third model, known as "*Fission theory*", argues that a part of the Earth was spun out to become the Moon. This model, however, has to raise the Earth-Moon angular momentum by several times than the present, which appears to be implausible.

In the mid 70th, a novel idea was proposed; Hartmann and Davis (1975) pointed out that the Earth had suffered massive collisions by other bodies, which produced a circum-Earth disk from which the Moon was accreted. Cameron and Ward (1976) suggested that a collision with a planet with the mass larger than Mars was needed to form the Earth-Moon system with the present angular momentum. The "*Giant impact theory*" has emerged as a plausible model for the origin of the Moon because of possible explanations for all the observations shown above.

The "*Giant impact theory*" has been studied with the calculation technique called smoothed particle hydrodynamics (SPH) (Benz et al., 1986, 1987, 1989), which is a technique to describe a fluid by an aggregate of particles with the Lagrangian concept and which is applied to numerical simulation of fluid dynamics in three dimensions. One of the well-known results of the giant impact simulation is that 84-92 % of the materials in the circum-Earth disk was derived from an impactor if an impactor collided

obliquely and slowly (<1.1 times of the escape velocity) (Benz et al., 1987; Canup et al., 2001; Canup, 2004), which is called "*standard model*". The results showed that the Moon underwent total melting and loss of volatile elements (Canup, 2004), which is in accordance with the lunar magma ocean model proposed from the observations of the lunar composition and internal structure. Other new dynamical models have been suggested for the giant impact. Ćuk and Stewart (2012) proposed a model, in which an impactor hit a rapidly rotating proto-Earth (called the "*fast-spin model*"), whereas Canup (2012) suggests a giant impact between two objects with half Earth's mass (called the "*sub-Earth model*"). The disks of the fast-spin model and sub-Earth model are hotter to vaporize larger fraction of the Earth (~ 80-90 % vapor) than the standard model (~ 20 %) (Nakajima and Stevenson, 2014). Most of the disk materials are estimated to be derived from the impactor in the *standard model*, whereas from the upper mantle of the proto-Earth in *fast-spin* and *sub-Earth models*. These new models well explain the oxygen isotopic similarity between the Earth and Moon, although extensive mixing between the circum-Earth disk and Earth's magma ocean is needed in the*standard model* (Pahlevan and Stevenson, 2007). The time scale of accretion of the Moon is estimated to be a few months to a year from a solid-rich disk (Ida et al., 1997; Kokubo et al., 1998). Whereas a vapor-rich disk is shown to induce several shocks propagating through the disk owing to the density heterogeneity with a large contrast, and it is hard to form a Moon from such a vapor-rich disk (Wada et al., 2006).

The enrichment of refractory components in the Moon has been often regarded as the evidence for high temperature by a giant impact since Cameron and Word (1976). However, it is arguable whether the timescale is long enough to fractionate refractory element in the lunar formation disk. Therefore, the bulk composition of the Moon is the key issue for the origin and interior evolution of the Moon.

1.4 Bulk composition of the Moon

The bulk chemical composition plays a key role on the evolution of the Moon, among which FeO and Al_2O_3 contents are specifically important: the FeO content affects (1) density and viscosity of melt, which control separation of minerals from the LMO, (2) chemical composition of olivine and pyroxenes, and (3) the bulk density and the moment of inertia, which depends on the amount of FeO in the mantle and the size of the metallic core. The Al_2O_3 content is also crucial in evolution of the LMO, because it affects the stability of anorthite, the major constituent of the highland crust, in the evolving LMO.

Previous workers have disputed whether the FeO and Al_2O_3 contents of the bulk Moon are similar to or richer than those of the Earth. Table 1.2 compares the previously estimated bulk silicate Moon, BSE, and CI-chondrite compositions. Although there are apparently insignificant differences among the estimations, the degree of enrichment of Al_2O_3 and FeO contents relative to the Earth shows considerable variations.

Longhi (2006) carried out mass balance calculations to estimate the bulk composition of the Moon on the basis of melting experiments (Longhi, 1992, 2003, 2005). The bulk Al_2O_3 content is estimated to be ~4 wt% being consistent with the source mantle composition for a low-Al_2O_3 magma, the green picritic glass, and is similar to the Earth's upper mantle. He also argued that the Mg# of the Moon is comparable to that of the Earth to generate the rocks of the magnesian suite. The bulk composition that Longhi estimated is called as Lunar Primitive Upper Mantle (LPUM). The estimate may be true for the mare basalts on the nearside of the Moon, but it is not known whether this estimation is applicable to the ancient magma ocean or the far side.

Taylor (1982) was the first who proposed that the Moon was more enriched in refractory elements than the Earth, which is called as Taylor Whole Moon (TWM). Using the bulk U content (~0.033 ppm) estimated from the heat flow measurement at the Apollo 15 and 17 sites (Langseth et al., 1976; Keihm and Langseth, 1977), Taylor estimated the Al_2O_3 content of the Moon to be 6.1 wt%. The FeO content was estimated to be 10-11 wt% from petrological requirements to generate the highland crust and the source regions of the mare basalts (Taylor and Bence, 1975; Longhi, 2005). This estimation may be valid only for the nearside of the Moon, which is known to be strongly concentrated in the heat source elements relative to the farside (Jolliff et al., 2000).

Warren (2005) estimated the bulk Al_2O_3 content of the Moon from the bulk Th content, which comes from the revised calibration of the Lunar Prospector gamma-ray data. On the basis of mass balance calculation using the compositional structure and thickness of the lunar crust, he estimated the Al_2O_3 contents to be 3.8 wt%, which was poorer than previous estimations. The value, however, may contain a considerable uncertainty, because the estimation is strongly dependent on the Th distribution in the lunar crust. The FeO content was estimated to be 9-10 wt% in order to be consistent with the high Mg# of olivine in the magnesian suite (0.87-0.90) (Warren, 1993). The magnesian suite, however, is a minor component of the Moon compared with the ferroan anorthosite, and it is not very convincing to argue that this magma intruded into the lunar crust from the LMO cumulates without any assimilation or melting. Warren (1990) was the first to emphasize the importance of FeO enrichment in the parent magma for anorthite flotation and argued that the ferroan anorthosite is really the magma ocean flotation product.

Khan et al. (2006) developed an inversion method to estimate mineralogy, mineral modal abundances, and thermal structure by using seismic data, lunar mass, and moment of inertia. They obtained a higher FeO content and lower Mg# than other estimations. The Al_2O_3 content is estimated to be ~4 wt%, which is similar to the terrestrial mantle, because a LMO composition with Al_2O_3 more than ~5 wt% produces a more aluminous phase resulting in higher seismic velocity that is in disagreement with the seismic model (Kuskov and Kronrod, 1998). The results, however, may contain considerable errors, as the authors themselves point out, due to uncertainties in the electric conductivity measurements in spite of the highly sophisticated inversion method.

There are several other estimations as listed in Table 1.2. Ringwood and Kesson (1977) and Ringwood (1979) estimated the bulk composition of the Moon by comparing MORB and lunar basalts and discussed that the Moon is a partial condensates from gas totally evaporated from the molten Earth. O'Neill (1991) and Jones and Delano (1989) estimated the bulk Moon composition on the basis of geochemical evolution of the Moon. Lognonné et al. (2003) reevaluated the Apollo lunar seismic data and estimated seismic velocity, density, temperature structures, and the bulk composition of the Moon by optimizing mixing ratios of several assumed distinct chemical reservoirs. Buck and Toksöz (1980) used seismic velocities of the crust and mantle, crustal thickness, and other geophysical data combined with a simple evolution models to estimate the bulk composition of the Moon. Snyder et al. (1992) modified the estimate of Buck and Toksöz

(1980) to be consistent with the crustal thickness. These estimates are more or less dependent on formation models that make many unverified assumptions.

The bulk composition controls phase relations and separation of phases crystallized, which further controls residual melt composition, that is, evolution of the LMO. The effectiveness of crystal-melt separation is controlled by physical properties of phases, particularly those of melt. Therefore, it is important to estimate the bulk abundances of FeO and Al_2O_3 simultaneously and by global constraints, although they have been estimated independently and/or on the basis of local geochemical data in previous work.

Table 1.2
Bulk compositions of the Moon estimated in previous studies. The compositions of the bulk silicate Earth (BSE) and a solar abundance are also shown for a comparison.

	SiO_2	Al_2O_3	FeO	MgO	CaO	Mg#	FeO[*3] [×BSE]	Al_2O_3[*4] [×BSE]
Longhi (2006)	46.1	3.9	7.6	38.3	3.2	0.90	0.9	0.9
Taylor (1982)	44.4	6.1	10.9	32.7	4.6	0.84	1.4	1.4
Warren (2005)	46.2	3.8	9.1	35.6	3.0	0.87	1.1	0.8
Khan et al. (2006)	45.5	4.1	12.5	34.6	3.3	0.83	1.5	0.9
Buck & Toksöz (1980)	48.4	5.0	12.9	29.0	3.8	0.80	1.5	1.3
Lognonné et al. (2003)	53.5	6.4	13.3	21.9	4.9	0.75	1.4	1.2
Jones & Delano (1989)	42.6	3.7	13.6	37.1	3.0	0.83	1.8	0.9
O'Neill (1991)	44.6	3.9	12.4	35.1	3.3	0.83	1.6	0.9
Ringwood (1979)	44.8	4.2	13.9	32.7	3.7	0.81	1.7	0.9
Snyder et al. (1992)	48.4	5.0	12.0	29.9	3.8	0.82	1.4	1.0
BSE[*1]	45.0	4.5	8.1	37.9	3.5	0.89	1.0	1.0
Solar abundance[*2]	34.4	2.5	34.4	23.5	2.0	0.55	5.6	0.7

[*1]McDonough and Sun (1995), [*2]Lodders (2003), n.d. : not determined, [*3, 4] Enrichment factor compared to the Earth

1.5 Purpose of this study

Lunar explorations including sample return by the Apollo missions, remote sensing, and lunar meteorite studies have been conducted since 1960s and provided us abundant information on the internal structure and thermal history of the Moon. The anorthosite-rich crust supports that a giant impact and subsequent global magma ocean are responsible for the origin and evolution of the Moon. The bulk composition of the Moon, particularly Al_2O_3 and FeO contents, has a significant importance for the origin and evolution of the Moon as discussed above.

In this study, we will estimate the bulk composition of the Moon by carefully examining conditions for anorthositic crust formation to satisfy both physical and chemical constraints for anorthite crystallization and their separation from the LMO through thermodynamic and fluid dynamic considerations. A new approach to constrain the REE patterns of the LMO is also proposed in this study.

The estimation procedure is as follows. At first, an initial composition is assumed, for which fractional crystallization calculation with various crystal separation modes is performed to determine the melt composition of first saturation with anorthosite. Then, chemical composition and physical properties of the magma at the time of anorthite crystallization are calculated. Finally, it is evaluated whether the generated crust and crust formation processes satisfy the following constraints: (1) the mass of anorthite crystallized from the residual melt is abundant enough to form the observed crustal thickness, (2) the density and viscosity of the melt are appropriate to segregate anorthite from a turbulent LMO, (3) the Mg# (= molar Mg/(Mg+Fe)) of mafic minerals crystallized with anorthite is consistent with that observed in the lunar highland rocks, and (4) the rare earth elements (REE) composition of the LMO is consist with that observed in the parent magma of the lunar highland rocks. The model has potential strength in that it depends on highly reliable global observations by recent explorations, but it does not depend on the local information.

Chapter 2. Differentiation Model

2.1 Concept of the model

To examine the chemical evolution of the lunar magma ocean (LMO) until the lunar crust formation, we constructed an incremental polybaric fractionation model with a parameter for the efficiency of crystal separation from LMO until anorthite begins to crystallize (Sakai et al., 2014). This model assumes differentiation of the LMO through crystallization of mafic minerals in the vigorously convecting main part and their settling and accumulation on the bottom of the LMO (Fig. 2.1). Essential model assumptions are: (1) the initial depth of the magma ocean is 1000 km; (2) Batch (equilibrium) crystallization takes place at the middle depth of the cooling LMO; and (3) Mafic minerals are instantaneously separated to the bottom of the LMO to form a cumulate pile when a crystal fraction in melt reaches a critical value. Differentiation mechanisms involving double diffusive convection or compositional convection could have been operated in the LMO differentiation as proposed by Mores (1982). The role of such mechanisms in the chemical evolution of the LMO will be critically evaluated later in section 4.6.1.

Thermodynamic calculation is performed with MELTS and pMELTS algorithms (Ghiorso and Sack, 1995; Asimow and Ghiorso, 1998; Ghiorso et al., 2002; Smith and Asimow, 2005). The melt composition at the time of anorthite appearance was evaluated whether it satisfies the following conditions: (1) the mass of anorthite crystallized from the residual melt is abundant enough to form the observed crustal thickness, (2) the density and viscosity of the melt are appropriate to segregate anorthite from a turbulent LMO, (3) the Mg# (= molar Mg/(Mg+Fe)) of mafic minerals crystallized with anorthite is consistent with that observed in the lunar highland rocks, and (4) the rare earth elements (REE) composition of the LMO is consistent with that observed in the parent magma of the lunar highland rocks. The evaluation was carried

out for a wide range of initial bulk compositions, and a plausible range of the FeO and Al_2O_3 contents in the initial LMO was estimated.

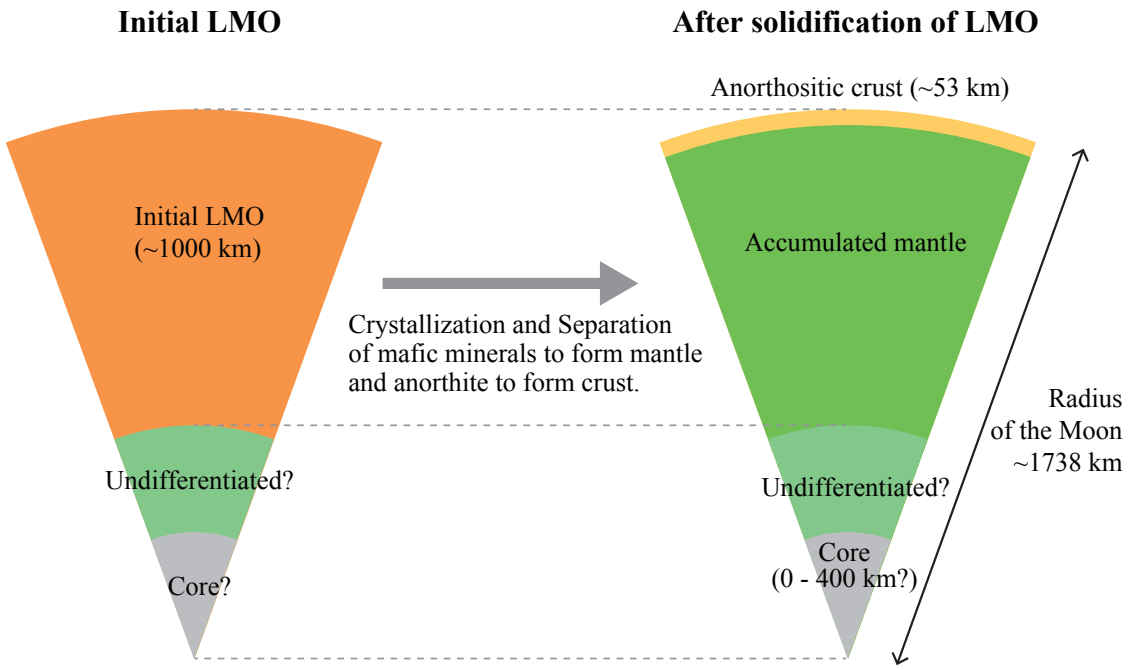

Fig. 2.1
Schematic illustration of the internal structure of the initial LMO assumed in this study (left) and of the current Moon (right). The initial LMO is assumed to have been 1000 km deep over the floor consisting of undifferentiated mantle and/or core. Mafic minerals such as olivine and pyroxenes crystallized in the LMO settled down to form a cumulus pile, while anorthite crystallized very late stage of the LMO solidification and floated to form the lunar crust, which resulted in the internal structure of the current Moon, shown on the right. It should be noted that the lunar crust occupies 8.9% of the assumed initial LMO in volume.

2.2 Calculation schemes

Figure 2.2 shows our calculation procedure outlined as a flowchart. First, we set the depth of initial LMO to the assumed value of 1000 km (#1 in Fig. 2.2). Then, we choose a set of values for compositional parameters for the initial LMO and parameter for efficiency of fractionation from the LMO, suspended crystal fraction limit, "X_{scfl}" (#2 in Fig. 2.2). How we set up compositional parameters, implications of the parameter representing fractionation efficiency, and how these parameter values are varied are explained below in detail. Next, we calculate the crystallization pressure, which is assumed to be the middle depth of LMO (#3 in Fig. 2.2). According to this pressure, we choose pMELTS algorithm for thermodynamic calculations if P_{LMO} > 1GPa or MELTS algorithm if P_{LMO} < 1GPa (#3 in Fig. 2.2). We prepare an input file containing the melt composition (C_{LMO}) and P_{LMO} to feed to the MELTS/pMELTS program (#4 in Fig. 2.2). The batch (closed-system) crystallization calculation of cooling LMO is performed until the crystal fraction in the melt reaches the suspended crystal fraction limit, X_{scfl}, by decreasing the temperature of LMO (T_{LMO}) from the liquidus at intervals of one degree Celsius under the chosen pressure (#5 in Fig. 2.2). During this calculation, T_{LMO}, C_{LMO}, and crystal fractions are monitored (#6 in Fig. 2.2). If the calculation fails before X_{scfl} is achieved (#7 in Fig. 2.2), we performed recalculation revising the melt composition by adding 0.05 wt% Fe_2O_3 (branching from #7 to return to #4 in Fig. 2.2), which is because the main reason for the calculation failure is too high FeO/(FeO+Fe_2O_3) ratio compared to the applicable compositional range for MELTS/pMELTS calculations. Next, we check whether anorthite crystallizes before X_{scfl} is achieved (#8 in Fig. 2.2). If not, we keep reducing T_{LMO}. After reaching a given X_{scfl}, the residual melt composition is passed to the next incremental stage after revising the depth of the LMO consisting of the crystal-free residual melt (#9 in Fig. 2.2). This presumes that crystals were instantaneously separated to the bottom of the LMO to form a cumulate pile without trapped melt.

The procedure of batch crystallization and crystal separation (#3-#9 in Fig. 2.2) is repeated until anorthite begins to crystallize. If anorthite begins to crystallize before X_{scfl} is achieved, the results of temperature, pressure, composition of melt, and total crystal fraction of the initial LMO at the time of anorthite appearance are output to a

file (#10 in Fig. 2.2). Further calculation after the plagioclase saturation near the solidus (> ~80% solidification) was mostly unsuccessful with MELTS/pMELTS, and we stop the calculation when anorthite appears in melt as a liquidus phase and use chemical conditions of the melt to constrain the initial bulk LMO composition in the following discussion.

The procedure from #3 to #9 in Fig. 2.2 was repeated 12-19 times for X_{scfl} = 0.1 and 3-4 times for X_{scfl} = 0.4 until anorthite appears as a liquidus phase. The pressure change at the middle depth of LMO with the progress of differentiation is shown in Fig. 2.3 for the cases of four X_{scfl}. A small X_{scfl} gives a small pressure jump between adjacent fractionation stages, and a large X_{scfl} a large pressure jump. The pressure jumps is one of the artifacts of our polybaric incremental model. Fortunately, the pressure jumps decrease with advance of the LMO solidification to 0.04 GPa for X_{scfl}=0.1 and 0.25 GPa for X_{scfl}=0.4, reducing effects of the artifact on anorthite crystallization.

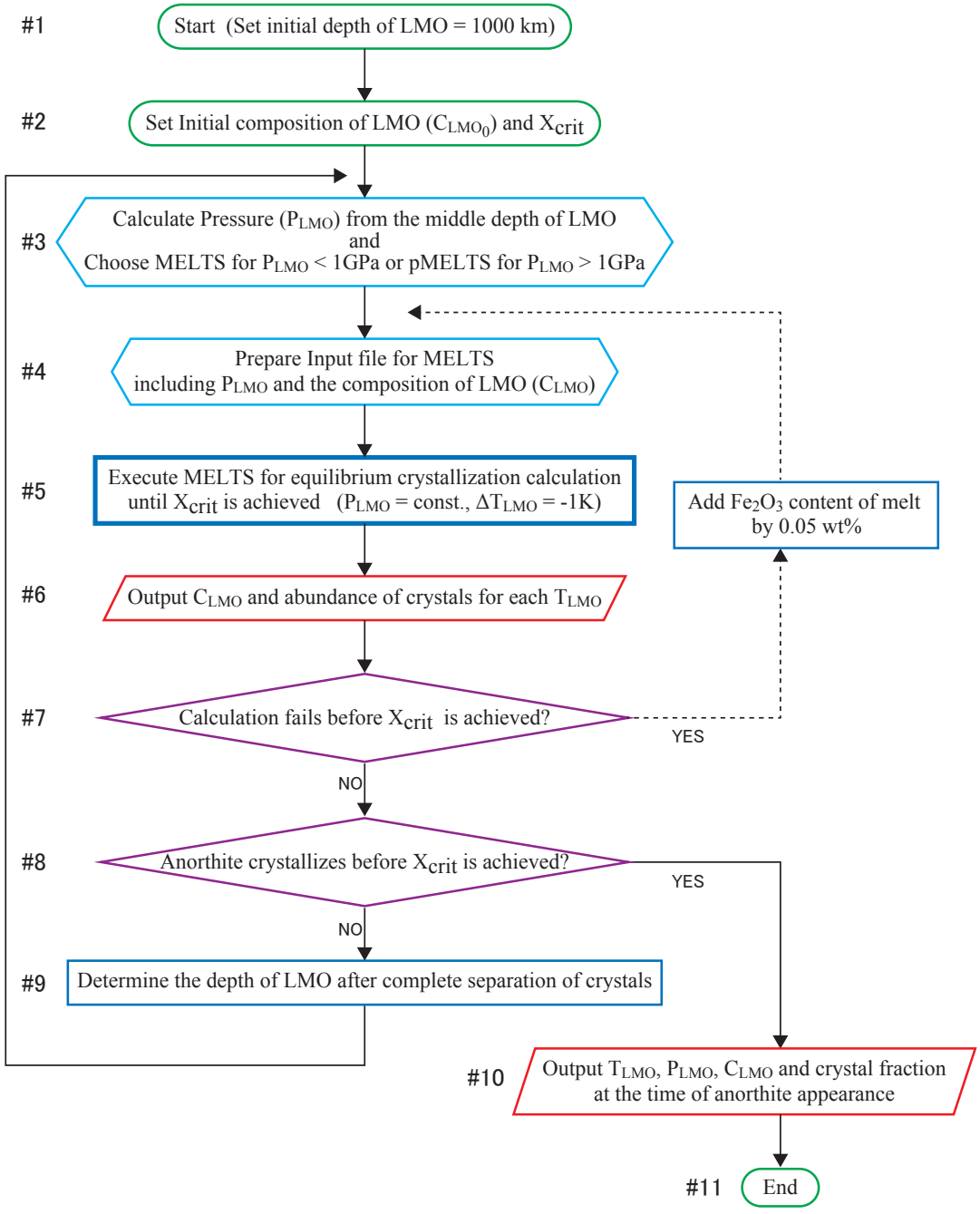

Fig. 2.2
Calculation procedures for incremental polybaric fractionation model developed in this study. The procedures are implemented in Shell and Perl scripts, which automatically perform these computation steps.

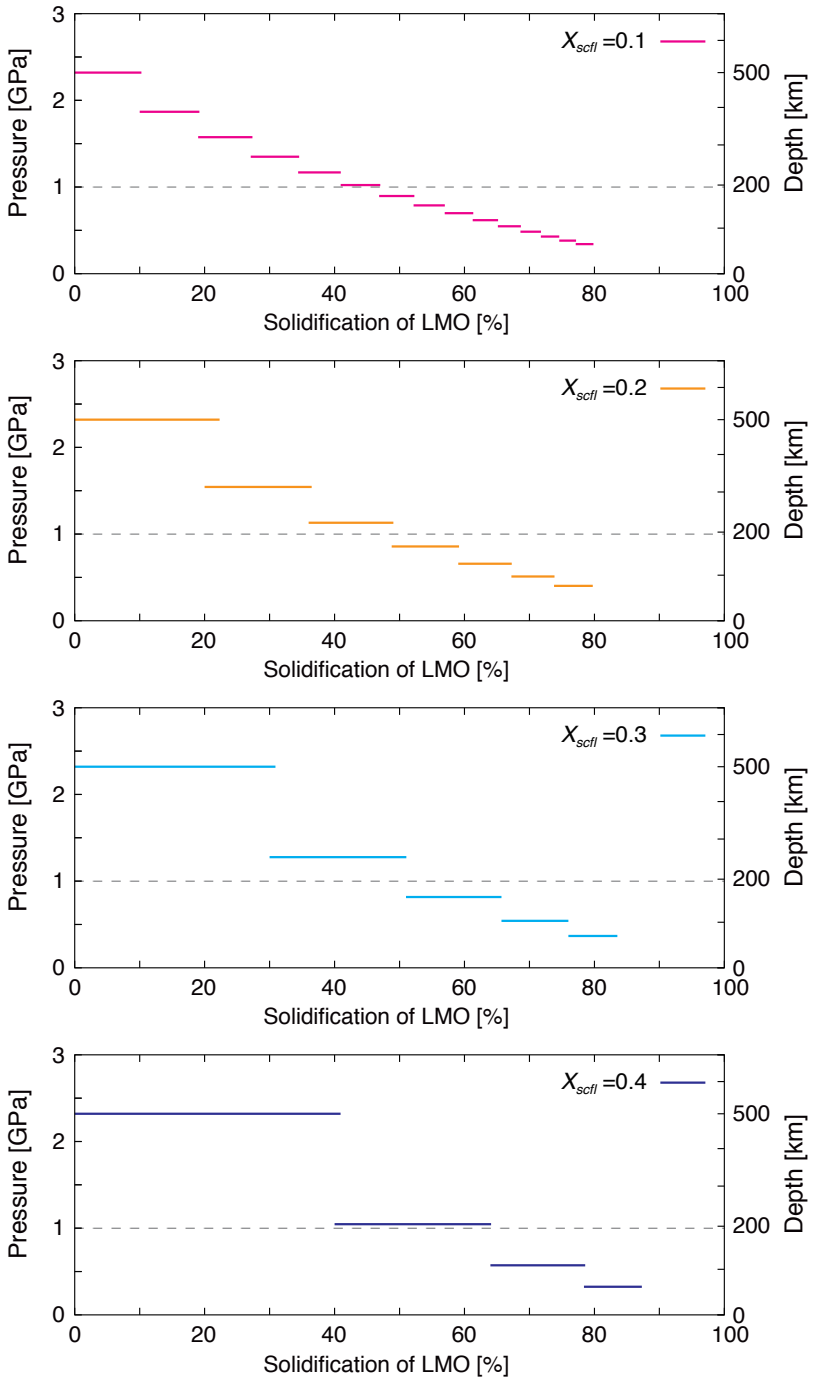

Fig. 2.3
Pressure change at the middle depth of the LMO with the progress of differentiation for the cases of four values of suspended crystal fraction limit, X_{scfl} (=0.1, 0.2, 0.3, and 0.4). A small X_{scfl} implies effective fractional crystallization, and a large X_{scfl} implies a condition closer to batch (or equilibrium) crystallization.

2.3 Calculation conditions

2.3.1 *Initial composition of LMO*

Examined compositions are shown in 3rd - 8th columns of Table 2.1, which fully covers the range of the bulk composition of the Moon proposed in previous studies (Table 1.2). The considered model system is a five components system: SiO_2-Al_2O_3-FeO-MgO-CaO. The Fe_2O_3, TiO_2, and Na_2O contents were set to be as small as possible to be able to run the MELTS/pMELTS program. Other elements, such as K, U, and Th, are ignored, because they are low in abundance and do not affect the phase relations and overall mass balance, although they are important as a heat source. For appropriate estimation of the LMO composition, we need a strategy to reduce number of compositional parameters covering possible compositional ranges. The initial composition of the magma ocean was prepared by setting FeO and Al_2O_3 contents as parameters (1st and 2nd columns in Table 2.1) based on the composition of the bulk silicate Earth (BSE). In order to determine the bulk LMO composition by these two parameters, the chondritic CaO/Al_2O_3 and the BSE-like MgO/SiO_2 are assumed, the justification for which is explained below.

Elements consisting of the Moon and other planets are classified in cosmochemistry into 6 categories based on volatility (Wasson, 1985; Lodders, 2003); super refractory, refractory, moderately refractory, moderately volatile, volatile and very volatile. Relative abundances of elements in the same category are maintained nearly constant in evaporation and condensation processes responsible for planet formation. Table 2.2 shows the classification of elements relevant to our study. Our study assumes that the ratios of MgO/SiO_2 and Al_2O_3/CaO are the same as that of BSE (1.25 in molar ratio) and CI chondrite (0.69 in molar ratio), respectively (McDonough and Sun, 1995).

The assumption of a constant Al_2O_3/CaO would be justified, because the ratio does not vary between BSE and chondrites (molar Al_2O_3/CaO ~0.69) (Table 1.2). The MgO/SiO_2 ratio of the BSE and CI chondrite, however, is not the same. The MgO/SiO_2 of bulk Earth (molar MgO/SiO_2 ~1.25) is significantly larger than that of the solar abundance or CI chondrite (molar MgO/SiO_2 ~1.07) (e.g. Ringwood, 1989; Allégre et al., 1995; McDonough and Sun, 1995; Lyubetskaya and Korenaga, 2007). In this study, the MgO/SiO_2 ratio of the LMO is assumed to be the same as that of BSE.

This assumption does not affect the overall mass balance between crust and mantle, which is the most important aspect in the present model, though it affects the mantle composition. Although Fe content also has similar volatility to Mg and Si, the FeO content strongly depends on the redox state during a process of planet formation, and its variation must be considered.

We thus have two compositional parameters. One is (Al_2O_3, CaO)/SiO_2, and the other is FeO/SiO_2. The initial composition (SiO_2, Al_2O_3, FeO, MgO and CaO contents) of the LMO in this study is obtained by varying these two parameters with fixed MgO/SiO_2 and Al_2O_3/CaO and the constant sum constraint (Table 2.1). According to this, the abundance of CaO varies in accordance with the variation of Al_2O_3 content. In order to avoid redundancy, we refer only Al_2O_3 for the initial LMO composition unless it is needed to refer CaO content explicitly.

Table 2.1
Compositions of the initial lunar magma ocean (LMO) examined in the present study. The composition of the bulk silicate Earth (BSE) (McDonough and Sun, 1995) is taken as the standard (bold), which were recalculated with varying degree of enrichment of FeO and Al_2O_3 contents to be 100 total wt%. The CaO content is assumed to keep the solar abundance ratio with Al_2O_3.

Enrichment (×BSE)		Initial Composition of the LMO (wt%)					
FeO	Al_2O_3	SiO_2	Al_2O_3	FeO	MgO	CaO	Mg#
0.8	0.8	47.1	3.72	6.74	39.5	2.97	0.91
0.8	1.0	46.3	4.58	6.62	38.9	3.65	0.91
0.8	1.3	45.2	5.81	6.46	37.9	4.63	0.91
0.8	1.5	44.5	6.60	6.36	37.3	5.26	0.91
0.8	1.8	43.4	7.73	6.22	36.5	6.17	0.91
0.8	2.0	42.8	8.46	6.12	35.9	6.75	0.91
1.0	0.8	46.3	3.66	8.28	38.9	2.92	0.89
1.0	**1.0**	**45.5**	**4.50**	**8.14**	**38.2**	**3.59**	**0.89**
1.0	1.3	44.5	5.72	7.95	37.3	4.56	0.89
1.0	1.5	43.8	6.49	7.83	36.7	5.18	0.89
1.0	1.8	42.8	7.61	7.65	35.9	6.07	0.89
1.0	2.0	42.1	8.33	7.54	35.4	6.65	0.89
1.0	2.3	41.2	9.37	7.37	34.6	7.48	0.89
1.0	2.5	40.6	10.0	7.26	34.1	8.01	0.89
1.3	0.8	45.2	3.57	10.5	37.9	2.85	0.87
1.3	1.0	44.4	4.40	10.3	37.3	3.51	0.87
1.3	1.3	43.4	5.58	10.1	36.5	4.45	0.87
1.3	1.5	42.8	6.34	9.94	35.9	5.06	0.87
1.3	1.8	41.8	7.44	9.72	35.1	5.94	0.87
1.3	2.0	41.2	8.15	9.58	34.6	6.50	0.87
1.3	2.3	40.3	9.17	9.37	33.8	7.31	0.87
1.3	2.5	39.7	9.82	9.24	33.4	7.84	0.87
1.5	0.8	44.4	3.52	11.9	37.3	2.81	0.85
1.5	1.0	43.8	4.33	11.7	36.7	3.45	0.85
1.5	1.3	42.8	5.50	11.5	35.9	4.39	0.85
1.5	1.5	42.1	6.25	11.3	35.4	4.98	0.85
1.5	1.8	41.2	7.33	11.1	34.6	5.85	0.85
1.5	2.0	40.6	8.03	10.9	34.1	6.41	0.85
1.5	2.3	39.7	9.04	10.7	33.4	7.21	0.85
1.5	2.5	39.2	9.69	10.5	32.9	7.73	0.85

Table 2.1 *continue*

1.8	0.8	43.4	3.43	14.0	36.4	2.74	0.82
1.8	1.0	42.7	4.23	13.8	35.9	3.37	0.82
1.8	1.3	41.8	5.37	13.5	35.1	4.29	0.82
1.8	1.5	41.2	6.11	13.3	34.6	4.87	0.82
1.8	1.8	40.3	7.17	13.0	33.8	5.72	0.82
1.8	2.0	39.7	7.86	12.8	33.4	6.27	0.82
1.8	2.3	38.9	8.85	12.5	32.7	7.06	0.82
2.0	0.8	42.7	3.38	15.3	35.9	2.70	0.81
2.0	1.0	42.1	4.16	15.1	35.3	3.32	0.81
2.0	1.3	41.2	5.29	14.7	34.6	4.22	0.81
2.0	1.5	40.6	6.02	14.5	34.1	4.80	0.81
2.0	1.8	39.7	7.07	14.2	33.4	5.64	0.81
2.0	2.0	39.2	7.75	14.0	32.9	6.18	0.81
2.3	1.0	41.2	4.07	16.9	34.6	3.25	0.78
2.3	1.3	40.3	5.18	16.6	33.8	4.13	0.78
2.3	1.5	39.7	5.89	16.3	33.3	4.70	0.78
2.3	1.8	38.9	6.92	16.0	32.7	5.52	0.78
2.5	1.0	40.6	4.01	18.1	34.1	3.20	0.77
2.5	1.3	39.7	5.11	17.8	33.3	4.07	0.77
2.5	1.5	39.2	5.81	17.5	32.9	4.63	0.77

Table 2.2
Grouping of elements based on volatility, which is represented by a temperature of ~50% condensation of the elements from gas with the solar composition at total pressure of 10^{-4} bar (Wasson, 1985; Lodders, 2003).

Refractory		Moderately refractory		Volatile	
	T (K)		T (K)		T (K)
Al	1680	**Fe**	1360	K	1000
Ca	1630	**Mg**	1340	Na	970
Ti, Th	1600	**Si**	1300		
U	1570				

2.3.2 *Initial depth of LMO and depth of crystallization*

Because of the smaller size and lower mean density of the Moon than the Earth, its gravitational acceleration is 1/6 of the Earth, and thus the Moon has a depth-pressure relationship distinct from the Earth. The depth-pressure relationship can be estimated with the assumption of hydrostatic equilibrium. The pressure change dP with a depth change dz is given by:

$$\mathrm{d}P = \rho g \mathrm{d}z\,, \tag{2.1}$$

where ρ is the density (the mean density of the Moon = 3344 kg/m^3) and gravitational acceleration, g, is given by:

$$\begin{aligned} g(z) &= G\frac{\frac{4}{3}\pi\rho(R_{\mathrm{moon}}-z)^3}{(R_{\mathrm{moon}}-z)^2} \\ &= \frac{4}{3}\pi G\rho(R_{\mathrm{moon}}-z)\,, \end{aligned} \tag{2.2}$$

where G is the gravitational constant (= 6.67x10^{-11} m^3/(kg s^2)), R_{moon} is the radius of the Moon (= 1738 km), and z is the depth from the surface of the Moon. We obtain the pressure at the depth H by integrating eq. (2.1) from 0 to H with respect to the depth (z):

$$P(H) = \frac{2}{3}\pi G\rho^2\left\{(R_{\mathrm{moon}})^2-(R_{\mathrm{moon}}-H)^2\right\}. \tag{2.3}$$

Figure 2.4 shows the calculated pressure profile of the Moon by assuming constant density of 3344kg/m^3 by using eq. (2.3). The pressure at the center of the Moon (= 1738 km) is 4.7 GPa, which corresponds to the depth of 150 km in the Earth. As pointed out in previous studies, it is very essential that the pressure gradient in the Moon is significantly lower than in the Earth.

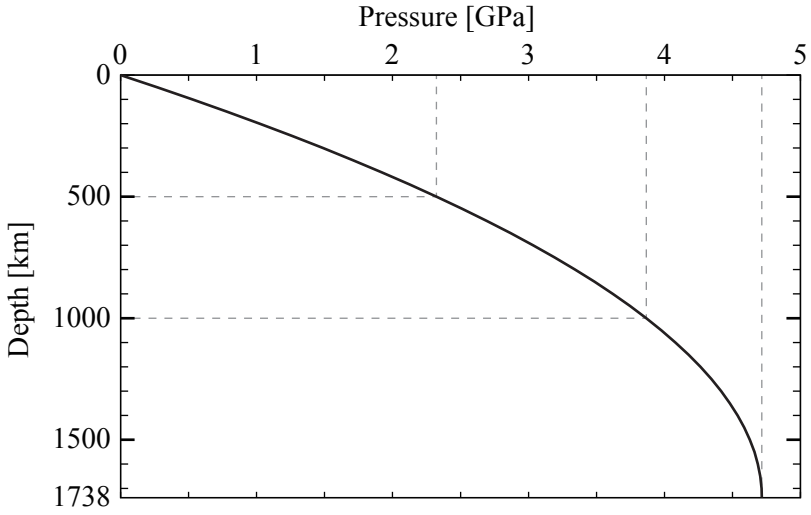

Fig. 2.4
Calculated pressure profile of the Moon based on the assumption of hydrostatic equilibrium and constant density (~3344 kg/m^3) (eq. 2.3). Pressure at the middle depth of LMO (~500 km), the bottom depth of LMO (~1000 km), and the center of the Moon (~1738 km) are 2.3, 3.9, and 4.7 GPa, respectively.

The depth where crystallization takes place strongly affects the chemical and physical evolution of the LMO. Previous study showed that the Moon was almost completely molten by a giant impact (Pritchard and Stevenson, 2000) and crystallization is thought to have taken place at all depths in the LMO (Tonks and Melosh, 1990).

This study assumed the initial LMO depth to be 1000 km as mentioned above. This is the depth of deep moonquakes, which is considered to be the boundary between the bottom of the initial LMO and the primitive lower mantle in previous studies (Nakamura et al., 1973; Khan et al., 2000; Lognonné, 2005; Elkins-Tanton et al., 2011). In order to justify our adoption of the initial depth of 1000km, we have performed calculation with variable depths of the initial LMO. The computation shows that the initial depth does not affect the results as far as it ranges from 800 km to 1738 km (half radius and the whole Moon, respectively).

In order to simulate crystallization at all depths in LMO, thermodynamic calculations were performed at a pressure of the middle depth of the solidifying LMO, which is the simple but plausible assumption for a small body where the pressure

effects on phase relation are not so crucial. This assumption is justified as far as: (1) the LMO is turbulent and well mixed, which is supported by previous studies (e.g., Tonks and Melosh, 1990), (2) the adiabat lies between the solidus and liquidus at all depths in the LMO owing to the smaller pressure dependence of the liquidus and solidus, and (3) the first liquidus phase is almost always olivine for all depth in the LMO. The second condition is examined below.

The phase relation of the initial LMO is evaluated from the pressure structure shown in Fig. 2.4. We conducted thermodynamic calculations by using the MELTS and pMELTS program (see below) from liquidus temperature to solidus temperature at the pressure of 500, 1000 and 1500 km. Figure 2.5 shows the phase relation for the initial LMO of the BSE composition. Although the low-pressure phase relation is consistent with the result of the experimental study (Elardo et al., 2011), there are few essential discrepancies with experiments. For example, the first liquidus phase is always olivine in experiments on the BSE-like composition (e.g., Takahashi, 1986), which is due to destabilization of olivine relative to orthopyroxene and garnet in pMELTS. This is discussed later in the discussion chapter. The thermal gradient of an adiabat is given by:

$$\frac{\mathrm{d}T}{\mathrm{d}P} = \frac{\alpha}{\rho C_\mathrm{p}} T \quad , \tag{2.4}$$

where T is the temperature, α is thermal expansion coefficient, C_p is isobaric heat capacity. By integrating (2.4) from the surface to a pressure P at depth z, adiabatic temperature of melt without crystallization is given by:

$$\ln T = \frac{\alpha}{\rho C_\mathrm{p}} P + \ln T_0 \quad , \tag{2.5}$$

where T_0 is the potential temperature. The first liquidus phase at pressure <2.5GPa, relevant pressure range in this study, is olivine liquidus. The adiabat and olivine liquidus is nearly parallel and solidus is much steeper. Therefore, it is reasonable to assume that the crystallization of LMO takes place at all depths at pressure <2.5GPa (Fig. 1.2.2). This relationship between adiabat and liquidus/solidus is valid for all the

calculations performed in this study.

In order to perform thermodynamic calculation based on our polybaric incremental fractionation model, we must determine the middle depth and pressure before calculation at each crystallization increment to advance calculations (#9 and #3 in Fig. 2.2). First, our method to calculate crystallization depth is explained. The volume of residual LMO (V'_{LMO}) after crystal separation is given as follows:

$$V'_{LMO} = (1 - X_{\mathrm{crit}}) \left\{ \frac{4}{3} \pi \left(R_{\mathrm{moon}} - H_{\mathrm{LMO}} \right)^3 \right\}, \tag{2.6}$$

$$V'_{\mathrm{LMO}} = \frac{4}{3} \pi \left(R_{\mathrm{moon}} - H'_{\mathrm{LMO}} \right)^3, \tag{2.7}$$

where H_{LMO} is the depth of LMO before crystal separation and H'_{LMO} is the depth of LMO after crystal separation. From eqs. (2.6) and (2.7), H'_{LMO} is calculated as follows (#9 in Fig. 2.2):

$$H'_{\mathrm{LMO}} = R_{\mathrm{moon}} - \sqrt[3]{1 - X_{\mathrm{crit}}} \left(R_{\mathrm{moon}} - H_{\mathrm{LMO}} \right). \tag{2.8}$$

The temperature and/or pressure dependence of the density of melt and minerals is not considered in calculation of the depth of LMO. The volume changes of melt and minerals are expected even in the lunar interior if their compressibility and thermal expansion cannot be neglected. We evaluated this using the Birch-Murnaghan equation of state for minerals and melts and an appropriate thermal structure of the moon. We found that they are only ~3-5% denser at the moon center than at surface, which is negligible in the evaluation of the LMO depth. Given the melt density of the initial LMO of ~3000 kg/m^3 (calculated by MELTS/pMELTS), the radius of the totally molten Moon just after its birth would be ~1800 km (larger by 3.6% than that of the current Moon of ~1738 km). We applied the constant radius of ~1738 km in our model because the differentiation of LMO progressed from the bottom of the LMO and the pressure gradient of the inner Moon is small.

If we know the depth of crystallization, we can determine the pressure of

crystallization (P_{LMO}) according to eq. (2.3). By inserting $H'_{\mathrm{LMO}}/2$ (middle depth of the LMO after the complete separation of crystal) into H in eq. (2.3), we obtained the pressure of crystallization as following (#3 in Fig. 2.2):

$$P_{\mathrm{LMO}} = \frac{2}{3}\pi G\rho^2 \left\{ \left(R_{\mathrm{moon}}\right)^2 - \left(R_{\mathrm{moon}} - \frac{H'_{\mathrm{LMO}}}{2} \right)^2 \right\}, \tag{2.9}$$

The liquidus temperature of orthopyroxene rapidly increases with increasing pressure and becomes almost the same as that of olivine at ~3 GPa according to MELTS (Fig. 2.5 for the BSE-like LMO). If this is the case, the depth of crystallization, which is assumed to be the mid depth of the LMO in this study, notably affects the amount of fractionated orthopyroxene relative to olivine before the first crystallization of anorthite, resulting in a shift in the melt composition at the first appearance of anorthite. This effect is not extensively examined in this study, but the effect may be small because more suppressed stability of orthopyroxene at high pressure than MELTS calculations has been demonstrated in melting experiments, such as Takahashi (1986).

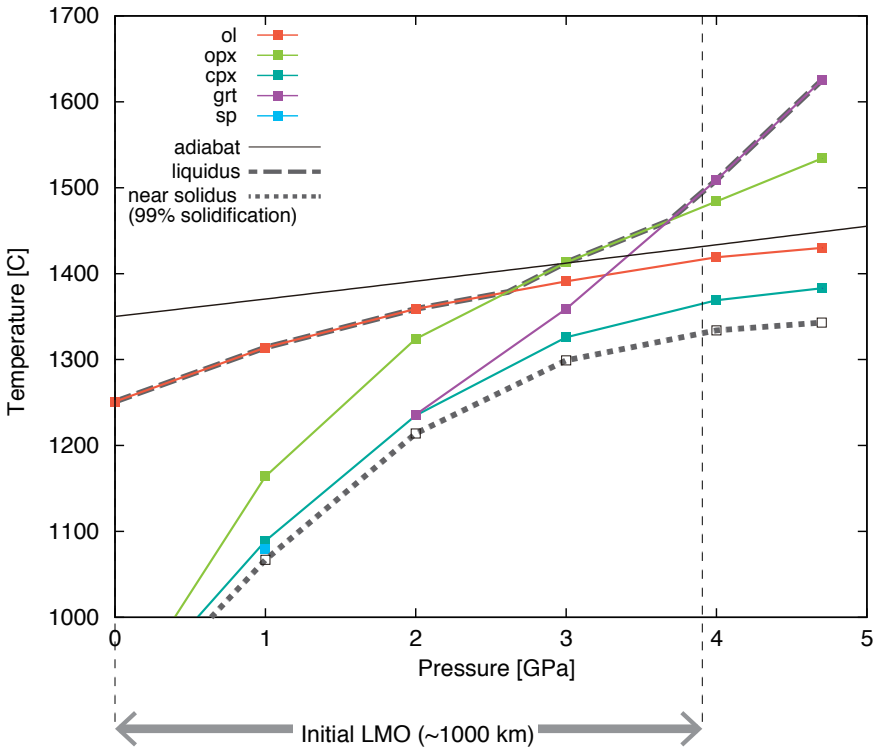

Fig. 2.5
Liquidus temperature of relevant phases plotted against pressure for the initial LMO of the BSE composition calculated with the MELTS/pMELTS program. Liquidus, near solidus (99% solidification), and an adiabat with potential temperature of ~1350 °C is also shown (dashed gray line, dotted gray line, and thin solid line, respectively). Note that the adiabat and the liquidus of olivine (red line) are almost parallel. The region of garnet appearance at a higher pressure (purple line) is negligibly small (< 2 wt%) for LMO with the initial depth of 1000km (~3.9 GPa).

2.3.3 *Efficiency of crystal/melt separation*

In order to model chemical evolution LMO, we have adopted an incremental polybaric fractionation model by introducing a parameter, suspended crystal fraction limit (X_{scfl}), to represent the efficiency of crystal separation from a convecting and crystallizing magma ocean. We assume that crystal separation takes place when the fraction of crystals (X = crystals/(crystals+melt) in weight) reaches a critical value, X_{scfl}. The efficiency of crystal separation is controlled by competition between time scales of crystallization and crystal separation, where the time scale of crystallization is dependent on cooling rate of LMO and the timescale of crystal separation on the grain size of crystals and the density and viscosity of the melt. Efficiency of crystal separation in a vigorously convective magma body has been experimentally and theoretically investigated by Martin and Nokes (1989) and Solomatov et al. (1993). They concluded that crystal separation takes place in a boundary layer instead of the main molten body and the efficiency is dependent on the grain size of crystals, viscosity of the melt and the density difference between melt and crystals. In the present model, the efficiency of crystal separation is treated by a simple parameter X_{scfl}.

The parameter, X_{scfl}, can be regarded as the efficiency of chemical fractionation of LMO, which can reproduce any mode of differentiation from fractional to equilibrium crystallization. A large X_{scfl} implies a condition closer to equilibrium, where crystals are retained in the magma ocean until large amounts of crystals appear (Tonks and Melosh, 1990); X_{scfl} =1 means no crystal separation and thus perfect equilibrium crystallization. On the other hand, a small X_{scfl} implies effective fractionation, where crystals are easily separated from the melt; X_{scfl} =0 represents the maximum fractionation and thus instantaneous separation of all crystals.

We present results for X_{scfl} ranging from 0.1 to 0.4 with 0.1 increments in the following sections, but we have examined X_{scfl} as small as 0.03 to extrapolate it to the near perfect fractional case (X_{scfl} ~0). We also examined X_{scfl} as large as 0.8 to examine near equilibrium crystallization case (X_{scfl} ~1). The reasons why we focused on X_{scfl} = 0.1 to 0.4 are (1) near fractional cases (X_{scfl} <0.1) are irrelevant to the turbulent LMO (Tonks and Melosh, 1990), (2) experiments show that viscosity of partially molten basaltic melt-crystal systems dramatically increases at the crystal fraction ~0.35 (Philpotts and Carroll, 1996; Sato, 2005), and (3) melt compositions at

the first appearance of plagiocase are similar for $X_{scfl} > 0.4$ as explained below. Previous models of LMO that assume equilibrium crystallization up to a certain solidification fraction (e.g., 50-80 %) followed by fractional crystallization (Snyder et al., 1992; Elardo et al., 2011) can be reproduced by our model as cases of small X_{scfl}. The significance of X_{scfl} is evaluated in Discussions.

2.4 MELTS program

LMO differentiation was modeled with the MELTS and pMELTS algorithm, which in based on Gibbs free energy minimization for liquid-solid equilibria in magmatic systems at high temperature and pressure. MELTS and pMELTS were based largely on an extended experimental data especially for the composition of MORB and alkalic mafic magmas, and optimized for mantle composition of the Earth at relatively low pressure (500-2000 °C, < 2 GPa) and high temperature and pressure (1000-2500 °C, 1-3 GPa), respectively.

We switch model calculation from the pMELTS algorithm to MELTS algorithm at 1 GPa (~200 km depth of the Moon). This introduces a discontinuity in temperature at ~1 GPa, but the melt composition changes smoothly and no inconsistency in phase assemblage occurs as shown below. Since we are concerned with chemical aspects of the LMO solidification process, the smooth compositional change and consistent phase appearance justify the combined usage of MELTS and pMELTS. This is because the switch takes place at 40-50 % solidification, where the phase relation is very simple being dominated by olivine with lesser amounts of orthopyroxene.

The Fe_2O_3, TiO_2 and Na_2O contents were set to be as small as possible to be able to run the MELTS/pMELTS program. In this study, the calculations for the FeO-rich composition (> ~2.3 ×BSE) failed before X_{scfl} is achieved and required the recalculation with adding Fe_2O_3 content. If a calculation fails before X_{scfl} is achieved, we performed recalculation with the melt composition by adding these minor elements. The maximum value of the Fe_2O_3 content in the initial LMO became 0.45 wt % for the initial FeO of ~2.5 ×BSE. This procedure has a negligible effect on the results because of the minor Fe_2O_3 relative to the initial FeO content.

Comparing Figs. 2.4 and 2.5, the abundance of garnet crystallized until the solidus temperature is achieved at the first crystallization depth of 500km is only ~1-2 vol% of the initial LMO. Therefore, we may assume that garnet scarcely affects the present calculation. The composition of silicate melts and the phase boundary between olivine and pyroxenes do not change within the pressure range of the Moon because of the small pressure dependence of the Mg-Fe distribution coefficient between melt and mafic minerals (Kushiro, 2001).

Uncertainty of the estimation could come from the chemical equilibrium calculation with MELTS/pMELTS. Although MELTS/pMELTS have been widely used, considerable degree of inconsistency has been pointed out for FeO-rich melt (Hirschmann et al., 1998; Ghiorso et al., 2002; El Maarry et al., 2009), where MELTS/pMELTS gives liquidus temperature of orthopyroxene higher by ~100 °C than experimental results for Martian magma (Bertka and Holloway, 1994). These systematic deviations were examined to find lower density and viscosity of melt by <1 % and ~50 %, respectively for the most FeO rich compositions. The effect of this uncertainly by MELTS/pMELTS calculations on the results of this study will be discussed in Discussion.

Chapter 3. Results

This chapter presents the results of the polybaric incremental fractionation modeling with thermodynamical calculation for the 200 cases; the 50 initial compositions of LMO as listed in Table 2.1 with varying X_{scfl} from 0.1 to 0.4 at 0.1 interval.

In the first section of this chapter, we will show the results for one case, bulk silicate Earth (BSE) composition and X_{scfl}, of 0.1, as an example. We further outline the entire results referring to pressure, temperature, and melt composition when anorthite first appeared as a liquidus phase. Then, we explain how initial FeO and Al_2O_3 contents and X_{scfl} affect the chemical composition of LMO when plagioclase first appears as a liquidus phase, based on which we will try to constrain the initial LMO composition in Discussion.

3.1 Calculation results

Figure 3.1 shows the change of melt composition by fractionation (a), fraction of phases crystallized and separated (b), and pressure before appearance of anorthite in a cooling LMO (c) for the initial composition of BSE and the suspended crystal fraction limit of X_{scfl} = 0.1. The melt becomes richer in Al_2O_3, CaO and FeO, poorer in MgO, and SiO_2 is kept almost constant with the progress of crystallization (Fig. 3.1a). Olivine is the first liquidus phase all through the process, which is followed by orthopyroxene and clinopyroxene (Fig. 3.1b). Olivine starts to crystallize at ~1640°C at the middle depth of the initial LMO (500km), which corresponds to 2.3 GPa in pressure. Orthopyroxene appears at 0.9 GPa and ~1630 °C, and clinopyroxene at 0.5 GPa and ~1360 °C. Anorthite appears at 0.34 GPa and ~1250 °C, when 77 wt% of LMO is solidified.

The entire crystallization sequence before anorthite crystallization is olivine followed by orthopyroxene and further by clinopyroxene and/or spinel with various

abundance depending on the bulk composition and pressure. This is consistent with previous experimental studies such as Elardo et al. (2011) and Snyder et al. (1992). For explanation purpose, the differentiation process of LMO from the liquidus to the first appearance of anorthite into 4 according to liquidus phase assemblage: Stage-1 olivine, Stage-2 olivine and orthopyroxene, and Stage-3 olivine, orthopyroxene, and clinopyroxene and/or spinel, and Stage-4 anorthite presence.

In the Stage-1 (0-47 wt% solidification of LMO in Fig. 3.1), only olivine crystallizes. The melt becomes richer in Al_2O_3, CaO and FeO, and poorer in MgO because of selective incorporation of Mg into olivine. The Mg# of melt steadily decreases all though this stage.

In the Stage-2 (47-71 wt%), orthopyroxene crystallizes along with olivine. The SiO_2 content in the melt slightly decreases. The trends of other oxide contents are similar to the Stage-1 because of the similarity in distribution coefficient of elements between orthopyroxene-melt and olivine-melt except for SiO_2. The Mg# of melt notably decreases in this stage.

In the Stage-3 (71-77 wt%), clinopyroxene crystallize because of the enrichment of CaO in the residual melt, suppressing the increase of CaO in the melt. The MgO content in the melt is steeply declined, the FeO content slightly increases, and the SiO_2 content follows the similarly decreasing trend as the Stage-2. Extreme enrichment of Al_2O_3 causes crystallization of spinel [$(Mg, Fe^{2+})(Al, Fe^{3+})_2O_4$], which suppresses the enrichment of Al_2O_3 in the residual melt, delaying crystallization of plagioclase. In the case shown in Fig. 3.1, spinel does not crystallized and enrichment of Al_2O_3 in the melt is further enhanced in this stage. Further decrease in Mg# of melt is notable.

In the Stage-4 (77wt%-), anorthite begins to crystallize from the residual LMO, which causes the Al_2O_3 content in the melt to decrease and the CaO content to stay nearly constant (Fig. 3.1). The decrease in MgO up to the Stage-3 ceases and an increase in FeO is more enhanced. The calculation with the MELTS program terminates at the solidification of ~80 % due to highly fractionated melt composition.

Tables 3.1-3.3 summarize results of model calculation for various initial FeO and Al_2O_3 compositions and X_{scfl}. The pressure and temperature at anorthite appearance range from 0.33 to 0.49 GPa and from ~1230 to ~1280 °C, respectively, depending on the initial composition and the mode of differentiation (Table 3.1). The composition of the LMO at the time of anorthite appearance is mostly 39-47 wt% SiO_2, 13-19 wt%

Al_2O_3, 10-16 wt% CaO, and 8-12 wt% MgO depending on the initial composition and the parameter X_{scfl}. The results are also illustrated in Figs. 3.2-3.5. Figures 3.2 and 3.3 show the melt composition at the time of anorthite crystallization, amounts of minerals fractionated, and density and viscosity of the residual melt plotted against the initial FeO content, for BSE-like and refractory-enriched initial LMO compositions, respectively. These results are also plotted against the initial Al_2O_3 content in Figs. 3.2 and 3.3 for BSE-like and FeO-enriched initial LMO compositions, respectively. The effects of the initial FeO and Al_2O_3 contents and X_{scfl} on the chemical and physical evolution of the LMO differentiation are discussed in the following sections by using these diagrams.

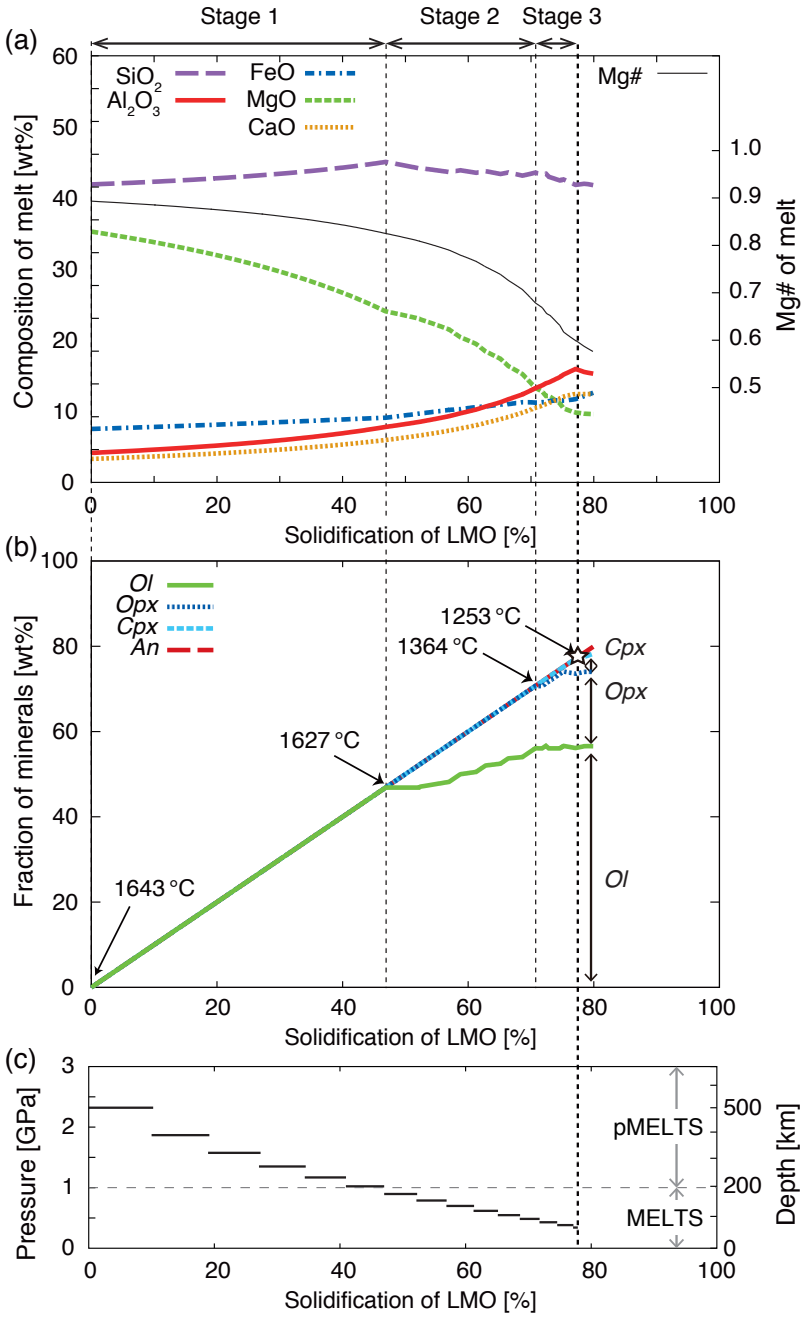

Fig. 3.1
Changes of (a) melt composition of the lunar magma ocean (LMO), (b) amount of minerals crystallized, and (c) pressures, with progress of LMO solidification reproduced in the incremental polybaric fractionation model based on thermodynamic calculations with the MELTS/pMELTS. An example shown here is for initial composition of the bulk silicate Earth (BSE) and X_{scfl} =0.1.

Table 3.1
Chemical composition of the lunar magma ocean (LMO) at the first appearance of anorthite as a liquidus phase for the assumed initial compositions shown in Table 2.1 and various values of suspended crystal fraction limit, X_{scfl}. Abbreviation; Mg# = molar Mg/(Mg+Fe)

Assumed conditions			Melt composition at the time of anorthite crystallization					
FeO (×BSE)	Al_2O_3 (×BSE)	X_{scfl}	SiO_2 (wt%)	Al_2O_3 (wt%)	FeO (wt%)	MgO (wt%)	CaO (wt%)	Mg#
1.0	1.0	0.1	45.6	17.4	12.8	10.7	13.5	0.60
1.0	1.0	0.2	45.6	17.8	12.2	10.8	13.6	0.61
1.0	1.0	0.3	46.1	17.6	11.5	10.9	13.9	0.63
1.0	1.0	0.4	45.5	18.1	10.9	11.3	14.2	0.65
1.0	1.5	0.1	45.0	19.3	9.9	11.6	14.2	0.68
1.0	1.5	0.4	44.6	19.1	10.5	11.6	14.2	0.66
1.0	2.0	0.1	44.4	18.8	10.0	11.8	15.0	0.68
1.0	2.0	0.4	44.3	19.2	10.3	11.2	15.0	0.66
1.0	2.5	0.1	42.5	17.0	12.6	11.9	16.1	0.63
1.0	2.5	0.4	42.5	17.9	11.2	11.4	17.0	0.65
1.5	1.0	0.1	43.1	15.9	19.2	9.6	12.2	0.47
1.5	1.0	0.4	43.2	17.2	16.6	10.4	12.7	0.53
2.0	1.0	0.1	40.9	14.7	24.5	8.7	11.2	0.39
2.0	1.0	0.4	41.2	16.0	21.3	9.7	11.8	0.45
2.5	1.0	0.1	39.8	14.0	27.9	7.9	10.4	0.34
2.5	1.0	0.4	40.0	14.9	24.9	9.0	11.2	0.39
1.5	1.5	0.1	43.0	17.6	15.6	10.5	13.3	0.55
1.5	1.5	0.4	43.0	17.9	15.7	10.1	13.2	0.54
2.0	2.0	0.1	38.5	13.0	26.7	8.9	12.9	0.37
2.0	2.0	0.4	39.4	14.5	22.6	9.2	14.4	0.42

Table 3.2
Amount of minerals fractionated from LMO until anorthite starts to crystallize for the assumed initial compositions shown in Table 2.1 and various values of suspended crystal fraction limit, X_{scfl}. Abbreviations; ol: olivine, opx: orthopyroxene, cpx: clinopyroxene, sp: spinel.

Assumed conditions			Amount of minerals fractionated (wt%)			
FeO (×BSE)	Al_2O_3 (×BSE)	X_{scfl}	ol (wt%)	opx (wt%)	cpx (wt%)	sp (wt%)
1.0	1.0	0.1	45.6	17.4	12.8	10.7
1.0	1.0	0.2	45.6	17.8	12.2	10.8
1.0	1.0	0.3	46.1	17.6	11.5	10.9
1.0	1.0	0.4	45.5	18.1	10.9	11.3
1.0	1.5	0.1	45.0	19.3	9.9	11.6
1.0	1.5	0.4	44.6	19.1	10.5	11.6
1.0	2.0	0.1	44.4	18.8	10.0	11.8
1.0	2.0	0.4	44.3	19.2	10.3	11.2
1.0	2.5	0.1	42.5	17.0	12.6	11.9
1.0	2.5	0.4	42.5	17.9	11.2	11.4
1.5	1.0	0.1	43.1	15.9	19.2	9.6
1.5	1.0	0.4	43.2	17.2	16.6	10.4
2.0	1.0	0.1	40.9	14.7	24.5	8.7
2.0	1.0	0.4	41.2	16.0	21.3	9.7
2.5	1.0	0.1	39.8	14.0	27.9	7.9
2.5	1.0	0.4	40.0	14.9	24.9	9.0
1.5	1.5	0.1	43.0	17.6	15.6	10.5
1.5	1.5	0.4	43.0	17.9	15.7	10.1
2.0	2.0	0.1	38.5	13.0	26.7	8.9
2.0	2.0	0.4	39.4	14.5	22.6	9.2

Table 3.3

Degree of solidification of the LMO (Φ_{LMO}), Physical condition (Temperature and Pressure), and physical properties of melt (density, ρ and viscosity, η) of the lunar magma ocean (LMO) at the first appearance of anorthite as a liquidus phase for the assumed initial compositions shown in Table 2 and various values of suspended crystal fraction limit, X_{scfl}.

Assumed conditions			Solidification degree	Physical conditions		Melt properties	
FeO (×BSE)	Al_2O_3 (×BSE)	X_{scfl}	Φ_{LMO} (wt%)	T (°C)	P (GPa)	ρ (kg/m^3)	η (Pa s)
1.0	1.0	0.1	77.2	1254	0.34	2840	4.2
1.0	1.0	0.2	78.7	1260	0.40	2830	4.2
1.0	1.0	0.3	77.4	1258	0.37	2820	4.4
1.0	1.0	0.4	79.2	1262	0.33	2820	4.5
1.0	1.5	0.1	68.8	1277	0.49	2820	3.9
1.0	1.5	0.4	78.4	1270	0.33	2820	4.1
1.0	2.0	0.1	69.3	1277	0.49	2830	3.8
1.0	2.0	0.4	77.9	1285	0.57	2840	3.3
1.0	2.5	0.1	77.2	1258	0.34	2870	4.0
1.0	2.5	0.4	78.6	1269	0.33	2850	3.9
1.5	1.0	0.1	75.9	1238	0.38	2950	2.0
1.5	1.0	0.4	79.2	1249	0.33	2900	2.4
2.0	1.0	0.1	74.8	1223	0.38	3030	1.4
2.0	1.0	0.4	78.9	1236	0.33	2980	1.7
2.5	1.0	0.1	73.0	1213	0.43	3090	1.1
2.5	1.0	0.4	78.7	1223	0.33	3030	1.4
1.5	1.5	0.1	68.7	1262	0.49	2910	2.3
1.5	1.5	0.4	78.4	1260	0.33	2890	2.3
2.0	2.0	0.1	77.3	1207	0.34	3080	1.3
2.0	2.0	0.4	78.4	1229	0.33	3010	1.9

3.2 Effect of the initial FeO content

Figures 3.2 and 3.3 show that the melt composition at the time of saturation in anorthite is strongly dependent on the initial FeO content: higher initial FeO abundance results in higher FeO content in the residual melt, which are almost linearly related. This is because olivine and orthopyroxene, which are the only two major phases fractionated before anorthite, have the similarly large distribution coefficients of Mg between them and silicate melt.

Among the fractionated minerals forming the mantle, olivine is dominant ranging from 55 to 70 wt%, and the abundance increases with increasing initial FeO content (green lines in Fig. 3.2b and 3.3b). The amount of orthopyroxene is complementary to that of olivine, that is, the lower initial FeO content tends to crystallize larger amount of orthopyroxene (blue line in Fig. 3.2b), which is particularly the case for the initial Al_2O_3 of ~1.0 ×BSE. This tendency is explained by the difference in the (Mg+Fe)/Si ratio in olivine and orthopyroxene, and the compensation causes little change of the total minerals separated to form the mantle (black lines in Fig. 3.2b and 3.3b). This also subdues the pressure effect on relative stability of orthopyroxene and olivine in our arbitrary choice of the crystallization depth at the middle of LMO.

The density and viscosity of the residual melt is highly dependent on the initial FeO content (Fig. 3.2c and 3.3c). In accordance with the increase in the FeO content, the density is higher for the higher initial FeO content. The viscosity is lower for the higher initial FeO content, which is partly attributed to the decrease in the SiO_2 content in the melt. These tendencies are scarcely dependent on other parameters, such as the initial Al_2O_3 in LMO and X_{scfl}.

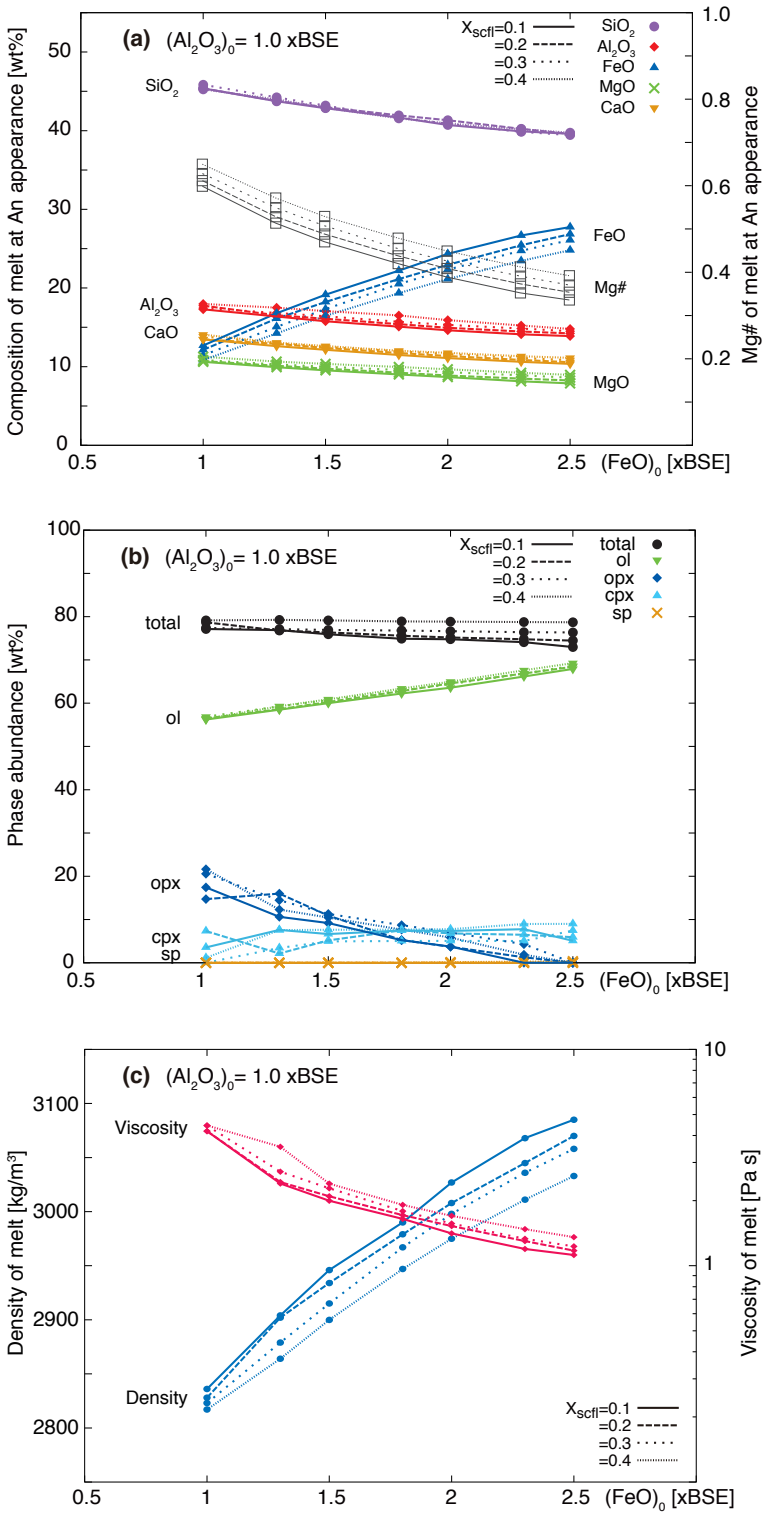

Fig. 3.2. Composition (a) and density (c) of the LMO melt at the first appearance of anorthite (An) and the amounts of crystals and their sum fractionated before the anorthite appearance (b) plotted against the initial FeO for BSE-like abundance of refractory elements. The initial Al_2O_3 content of the LMO is fixed at 1.0 ×BSE.

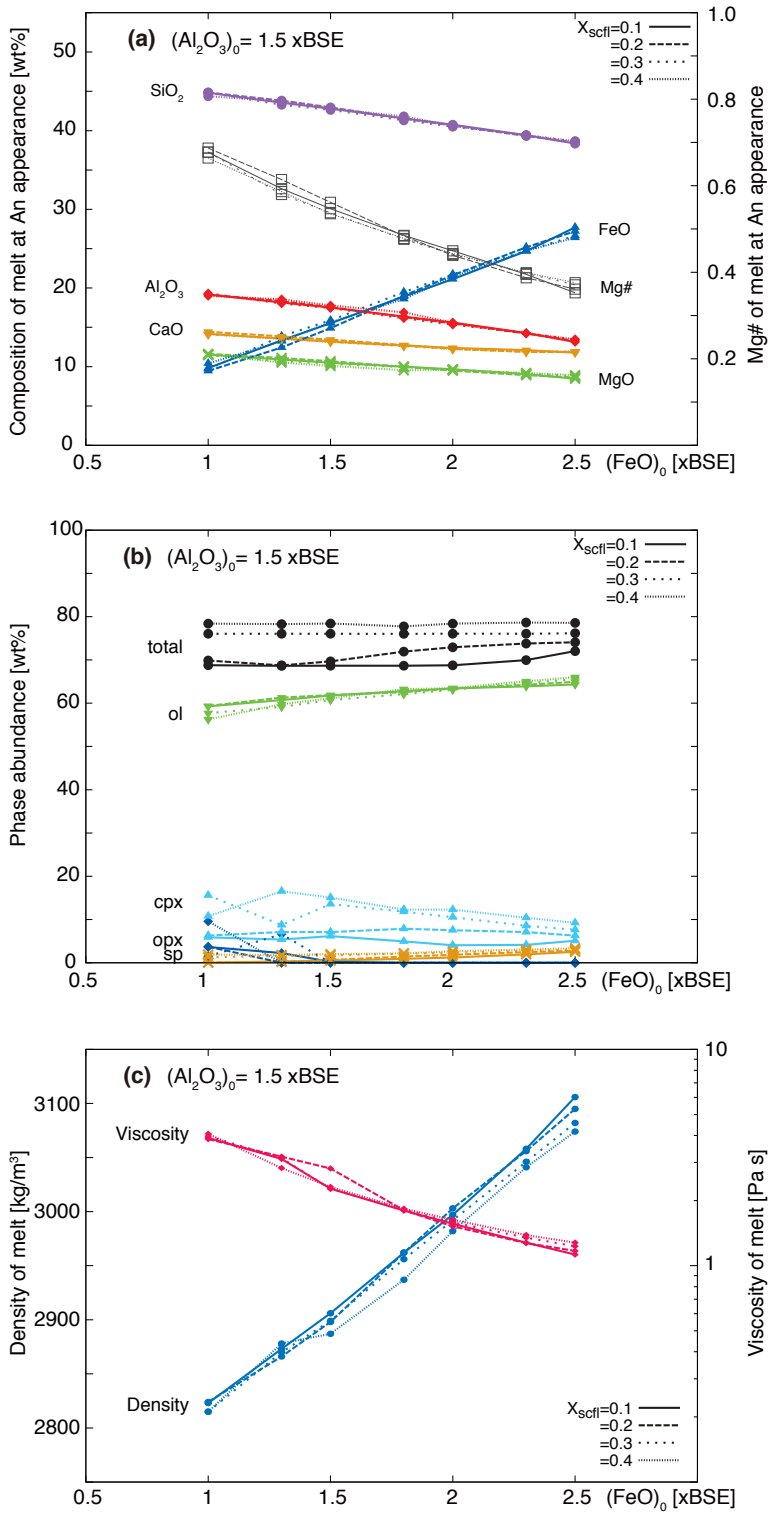

Fig. 3.3. Composition (a) and density (c) of the LMO melt at the first appearance of anorthite (An) and the amounts of crystals and their sum fractionated before the appearance of anorthite (b) plotted against the initial FeO for a case with enrichment in refractory elements. The initial Al_2O_3 is fixed at 1.5 ×BSE.

3.3 Effect of the initial Al_2O_3 content

Melt composition at the time of saturation in anorthite has weaker dependent on the initial Al_2O_3 content than the initial FeO content (cf., Figs. 3.2 and 3.4 or Figs. 3.3 and 3.5). Another feature of the effect of initial Al_2O_3 content notable in Figs. 3.4 and 3.5 is convex or concave upward variation patterns (e.g., Al_2O_3 and FeO contents and Mg#), which is very weakly shown or absent in Figs. 3.2 and 3.3 for the initial FeO variation. The tendency is more conspicuous when the initial FeO content is high (c.f., Fig. 3.4 and 3.5). The dependence of the initial Al_2O_3 content on the degree of solidification of the LMO (and that on fractionated olivine abundance) at the time of first appearance of anorthite is convex downwards (black lines in Fig. 3.4b and 3.5b) particularly for small values of X_{scfl}. The degree of the LMO solidification is similar irrespective of X_{scfl}, if the initial Al_2O_3 content is very high (e.g., 2.5 ×BSE) or very low (e.g., BSE), but strongly depends on X_{scfl} at a intermediate value of the initial Al_2O_3 content (1.5-2.0 ×BSE) (Figs. 3.4b and 3.5b). It is worth noting that the fraction of solidification of LMO when anorthite appears as a liquidus phase is variable from 70 to 90 wt% (Fig. 3.4b and 3.5b). This plays a very important role in controlling the amount of FeO and Mg# of the melt at anorthite appearance.

The amount of fractionated clinopyroxene has strong relationship to the initial CaO content; that is, more clinopyroxene is crystallized when the initial CaO content is high (Fig. 3.4b and 3.5b). Please note that CaO/Al_2O_3 ratio of the initial LMO is kept constant, and higher Al_2O_3 implies higher CaO. Spinel crystallizes when the initial content of Al_2O_3 is >1.5 times of BSE, which suppresses enrichment of Al_2O_3 in the residual melt, and consequently, anorthite appearance particularly when the initial FeO content is high or X_{scfl} is small (Fig. 3.4b and 3.5b).

The density of melt is not affected by the initial Al_2O_3 content unless the initial LMO is Al_2O_3-rich (> 1.5 times of BSE), in which the density of melts increases because of the FeO enrichment due to the high degree solidification of LMO (Fig. 3.4c and 3.5c). The viscosity of melt is not affected by the initial Al_2O_3 content because the SiO_2 content of LMO at the first appearance of anorthite is almost constant with the various initial Al_2O_3 content.

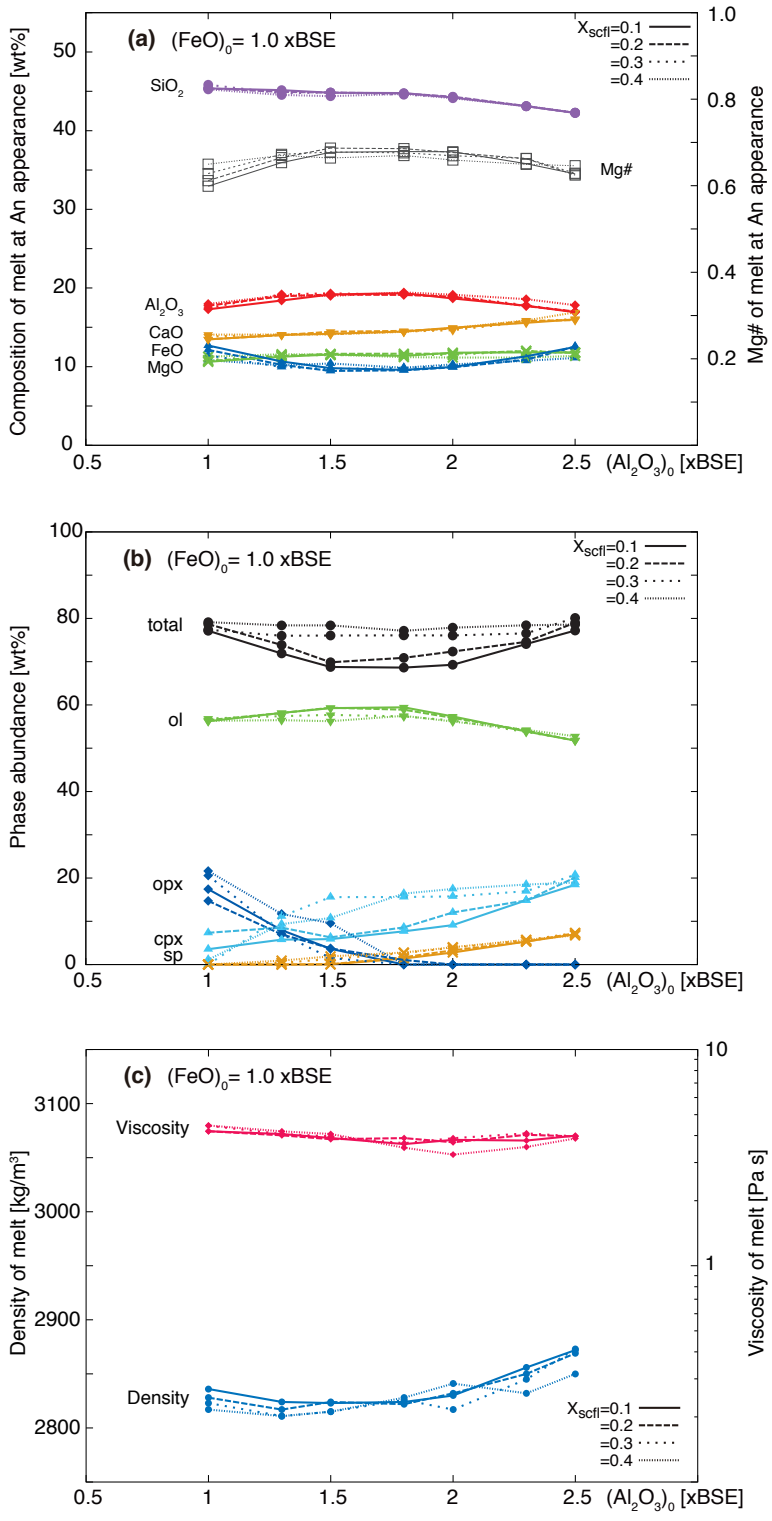

Fig. 3.4. Composition (a) and density (c) of the LMO melt at the first appearance of anorthite (An) and the amounts of crystals and their sum fractionated before the anorthite appearance plotted against initial Al_2O_3 for BSE-like abundance of FeO. The initial FeO content in the initial LMO melt is fixed at 1.0 ×BSE.

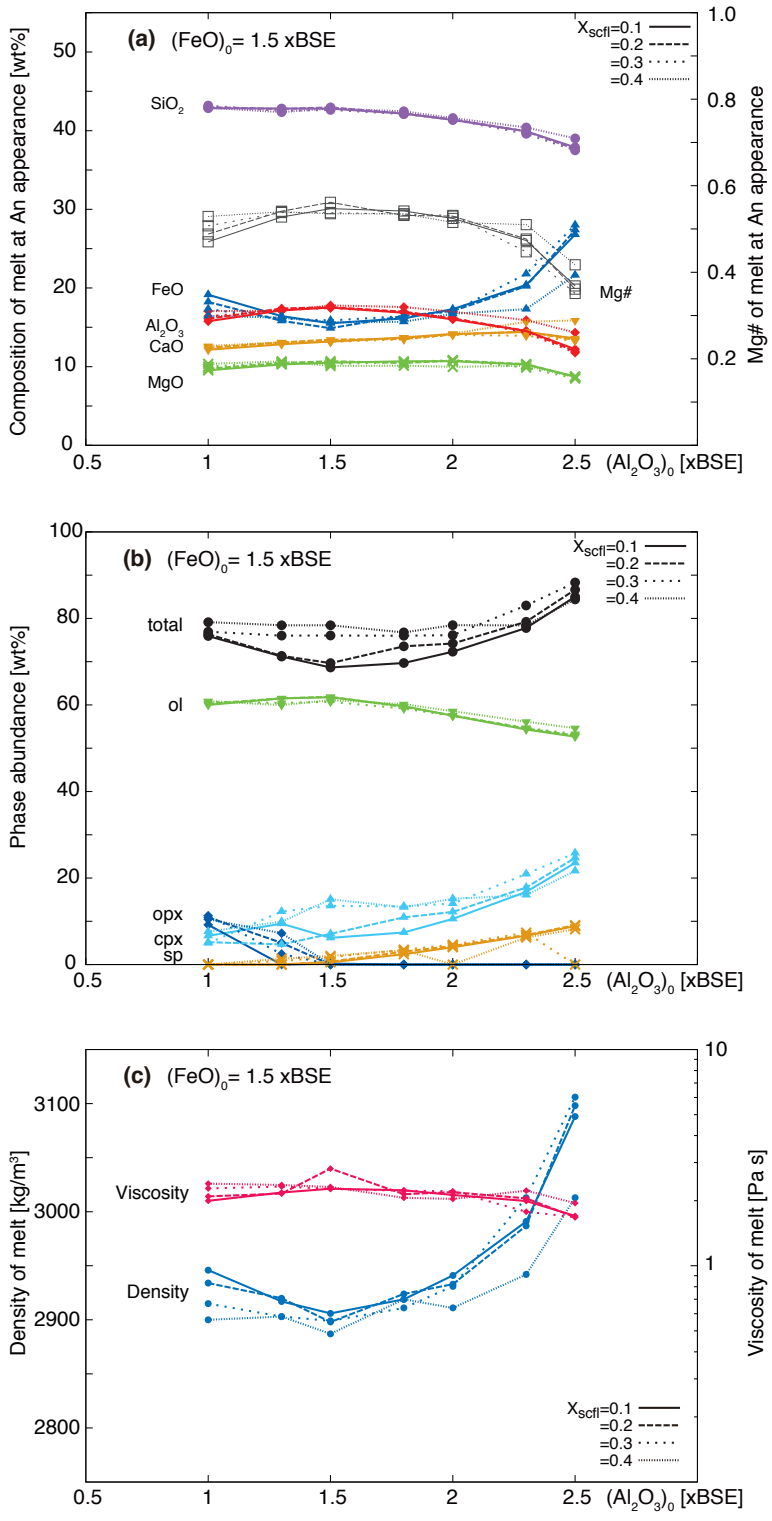

Fig. 3.5. Composition (a) and density (c) of the LMO at the first appearance of anorthite (An) and the amounts of crystals and their sum fractionated before the anorthite appearance plotted against initial Al_2O_3 for Fe-enriched case. The initial FeO content in the LMO is fixed at 1.5 ×BSE.

3.4 Effect of the suspended crystal fraction limit, X_{scfl}

Figures 3.2-3.5 show that X_{scfl} does not significantly affect the composition of the melt at the time of anorthite appearance. Contrary to this, the amounts of mafic minerals crystallized before anorthite saturation conditionally depends on X_{scfl}. Figure 3.6 shows the same results shown in Figs. 3.2-3.5, but chosen parameters plotted against X_{scfl}. These diagrams show that the FeO content and Mg# of the residual melt is dependent on the X_{scfl} if the initial Al_2O_3 content is as low as that of the BSE (solid lines). On the other hand, the degree of solidification is dependent on X_{scfl} regardless of the Al_2O_3 content. The dependence is uniquely determined at high X_{scfl}, but variable at low X_{scfl} with a higher degree of solidification for low initial Al_2O_3 content than for high initial Al_2O_3 content.

The dependence or independence of residual melt composition on X_{scfl} can be explained by the pressure of anorthite crystallization. Anorthite crystallizes from a broad compositional range at low pressures (~0.5 GPa), but only from an Al_2O_3-rich melt at high pressures (> ~1 GPa) (Kushiro, 1969; Presnall et al., 1978, 1979). Because the enrichment of Al_2O_3 in residual melt occurs in the early stage for the initial Al_2O_3 as high as ~1.5 times of BSE, anorthite can crystallize at low solidification degree at high pressures. Note that solidification degree and crystallization pressure hare negatively correlated in our model (Figs. 2.2 and 3.1c). The enrichment of Al_2O_3 is easily achieved by near maximum fractional crystallization (= small X_{scfl}) compared to that by near batch crystallization (= large X_{scfl}), which results in anorthite crystallization at an early stage of LMO differentiation and at high pressure. In high-Al_2O_3 melt, X_{scfl} affects the degree of LMO solidification and does not affect the composition of melt at the time of anorthite appearance because the condition of anorthite crystallization is governed mainly by the enrichment of Al_2O_3 content in melt (Fig. 3.6c). On the other hands, the LMO with the initial Al_2O_3 of BSE-like content cannot make anorthite crystallize at high pressure because of the weak enrichment of Al_2O_3 content in melt. Anorthite crystallizes from the melt with broad compositional range of Al_2O_3 content if pressure is low enough. In low-Al_2O_3 melt, X_{scfl} affects the composition of melt and does not affect the degree of LMO solidification at the time of anorthite appearance because the condition of anorthite crystallization is governed

mainly by the decrease of pressure with differentiation (Fig. 3.6a and 3.6b). The overall results, however, indicates that X_{scfl} does not significantly affect the composition of the melt and the degree of LMO solidification at the time of anorthite appearance, which is contrasting to the effects of the initial FeO and Al_2O_3 contents.

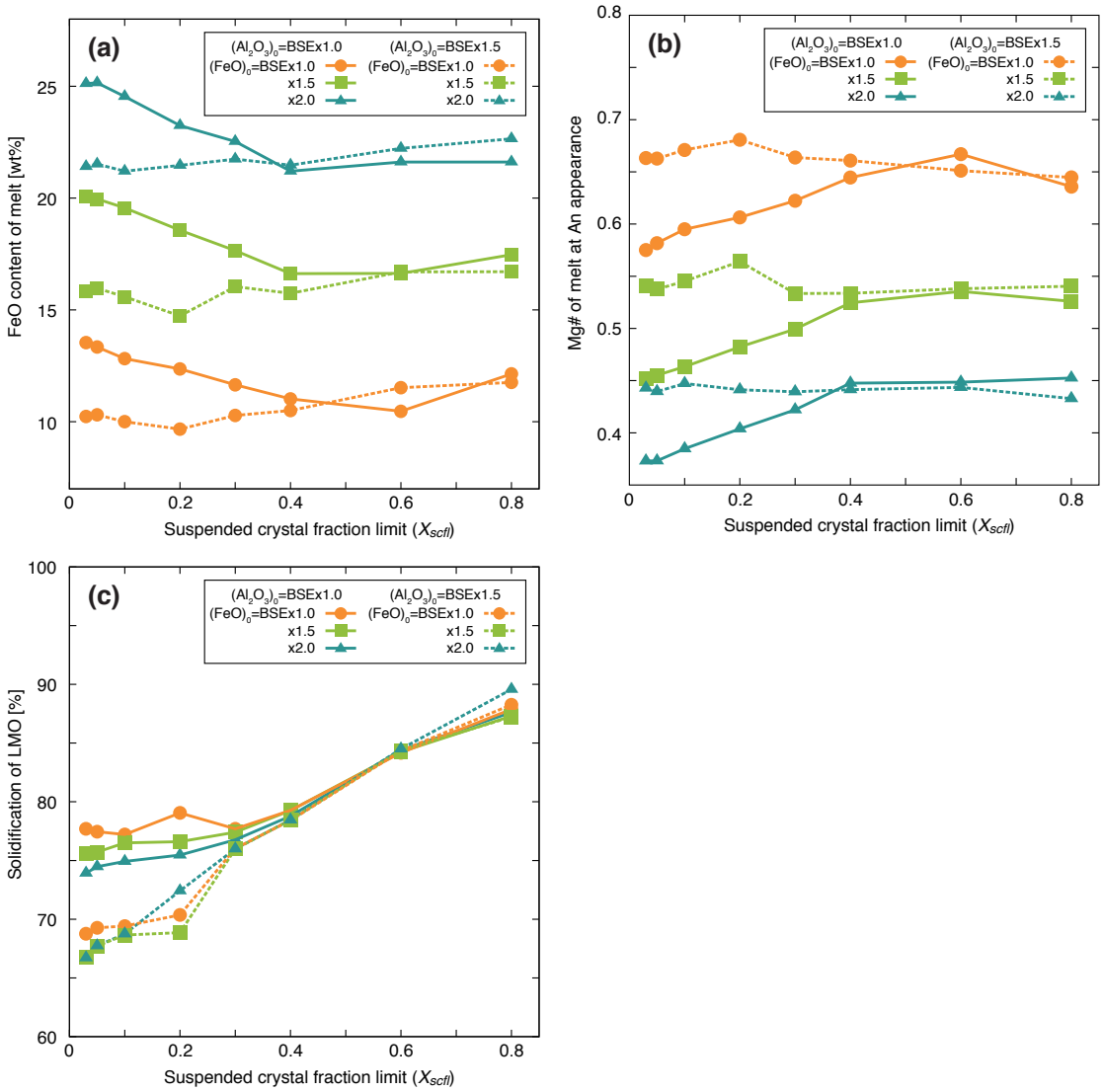

Fig. 3.6

FeO content (a), Mg# (Mg/(Mg+Fe)) (b), and degree of solidification (c) of the lunar magma ocean (LMO) at the first appearance of anorthite (An) plotted against the suspended crystal fraction, X_{scfl}. The parameter X_{scfl} represents the fraction of crystals up to which crystals are retained in the LMO. Symbols connected by lines are for various initial FeO contents with fixed initial Al_2O_3 content at 1.0 ×BSE, and those connected by dashed lines are for various initial FeO contents with fixed initial Al_2O_3 content at 1.5 ×BSE. It is notable, as shown in panes (a) and (b), that the anorthite-saturated melt compositions do not depend on X_{scfl}, if X_{scfl} is greater than 0.4 or if the initial Al_2O_3 content is ~1.5 ×BSE. The degree of solidification notably depends on X_{scfl}, irrespective of the initial Al_2O_3 content as shown in (c).

3.5 Summary

We conducted thermodynamic calculations to model polybaric incremental fractionation in LMO for the 200 cases by varying the initial composition and the efficiency of crystal separation. The main results of the calculation are summarized as follows:

(a) The chemical composition of LMO at the first anorthosite crystallization is strongly dependent on the initial FeO content. Higher initial abundance of FeO causes an increase of density of melt because of enrichment of FeO in the residual melt.

(b) The Mg# of melt has a negative correlation with the initial FeO content, which is most conspicuous for the initial Al_2O_3 content ~1.5 times of BSE.

(c) Clinopyroxene and/or spinel, which contain large amounts of refractory elements such as Al_2O_3 and CaO, crystallize from a melt rich in Al_2O_3 and CaO.

(d) The degree of LMO solidification is affected by the initial Al_2O_3 content, which is lowest for melt with the initial Al_2O_3 content ~1.5 times of BSE. This is because the Al_2O_3 content of melt at the anorthite appearance increases with increasing initial Al_2O_3 content up to ~1.5 times BSE and decreases for further increase in the initial Al_2O_3 content, because anorthite crystallization is suppressed by spinel crystallization.

(e) The suspended crystal fraction limit, X_{scfl}, does not significantly affect the chemical composition and thus physical properties of the residual melt at the time of anorthite appearance except for low Al_2O_3 content (~BSE). The degree of LMO solidification before anorthite saturation varies from 70 to 90%, and is controlled by X_{scfl}, particularly when the initial Al_2O_3 content is ~1.5 ×BSE.

The four conditions for the anorthosite crust formation were evaluated based on the above results: (1) thickness of lunar crust, (2) conditions for anorthite separation in a turbulent magma ocean, (3) major element composition of mafic minerals in crust and (4) rare earth element composition of crustal rocks.

Chapter 4. Discussions

The differentiation model discussed above should satisfy the observations features of the highland crust. We, as mentioned above, examine the following four constraints: (1) the thickness of the anorthosite crust, (2) anorthite flotation in a turbulent magma ocean, (3) Mg/(Mg+Fe) of mafic minerals co-crystallized with anorthosite, and (4) Rare earth element composition of crustal rocks. They are discussed in this order on the basis of modeling results presented in Chapter 3.

4.1 Constraint 1: Thickness of the lunar crust

In this section, the amount of anorthite crystallized from the residual melts is estimated, and we will evaluate whether it is abundant enough to achieve the average highland crustal thickness.

Although there have been many lunar missions providing precise topographic and gravity data, the thickness of the crust is very difficult to be constrained because of the lack of absolute average density of the lunar crust and mantle, which requires more seismic observations (e.g., Kamata et al., 2013). The observations by the Apollo seismic, Lunar Prospector and Kaguya data show that the thickness of the anorthosite crust is approximately 45 to 60 km (Lognonné et al., 2003; Wieczorek et al., 2006; Ishihara et al., 2009). The most recent observation by GRAIL show that the thickness of the anorthosite crust is 34 to 43 km (Wieczoreck et al., 2013) from the average density of crust and mantle with the values of 2550 and 3150-3220 kg/m^3, respectively. These densities are, however, lower than the pure anorthite density of ~2700 kg/m^3 and the lunar bulk density of 3344 kg/m^3. We therefore use the average thickness of 53 km by Kaguya (Ishihara et al., 2009) in the following discussions. Previous estimates for the Al_2O_3 content of the crust range from 26 to 30 wt% based on geophysical,

remote sensing, and sample analyses data (Korotev, 2000; Wieczorek and Zuber, 2001; Taylor et al., 2006b). This composition of ~28 wt% Al_2O_3 on average corresponds to ~78 % anorthite by mass or about ~82 % by volume, although these values may represent a shallower part of the lunar highland crust. We assume that the crust consists of 100 % anorthite, because Kaguya observation reported pure anorthosite globally, which is inferred to represent deep crustal material exposed on the surface (Ohtake et al., 2009).

We adopt CIPW normative calculation to obtain modal abundances of several common minerals stable at 1 atm such as olivine, pyroxenes and anorthite crystallized from the anorthite saturated melts ("residual melt") obtained in the last chapter, because the calculations with the MELTS/pMELTS program are unstable for highly fractionated melt compositions. The results are shown in Table 4.1, in which the volume % of anorthite (An) and the thickness of the crust formed from the residual melt (H_{crust}) are listed. The CIPW normative abundance of anorthite varies from 42 to 57 vol% depending on the initial bulk composition, which decreases with increasing initial FeO and Al_2O_3 contents. The melt with higher initial FeO content crystallizes a larger amount of olivine, which results in a lesser amount of anorthite crystallization. The melt rich in Al_2O_3 (1.5 ×BSE) crystallizes a large amount of spinel and clinopyroxene, and the amount of anorthite crystallized from the residual melt is also small.

The CIPW normative composition and the LMO depth at the appearance of anorthite enable us to calculate the maximum thickness, H_{crust}, of the crust by assuming complete anorthite segregation and no melt trapping in the cumulate pile on the bottom of LMO (Table 4.1). It is evaluated whether obtained thickness satisfies the observed crustal thickness (~53 km). Calculated H_{crust} along with the actual crust thickness are plotted against the initial Al_2O_3 in LMO in Fig. 4.1.1 for a given value of the initial FeO content and four values of X_{scfl}. The calculated crust thickness increases with the increase of initial Al_2O_3 content first, reaches a maximum, and then decreases with further increase, which is most conspicuous when the initial FeO is close to BSE. This is because the Al_2O_3 content of the melt at the anorthite appearance increases with increasing initial Al_2O_3 content up to ~1.5 ×BSE and decreases for further increase in the initial Al_2O_3 content over ~1.5 ×BSE (solid curves in Fig. 3.4a-3.5a). This results in the higher abundance of anorthite at an intermediate value of the initial Al_2O_3

content of the LMO (Fig. 4.1.1). The decrease of the crustal thickness for higher initial Al_2O_3 contents (>1.5 ×BSE) are due to crystallization of spinel at high pressure, which suppresses the increase in Al_2O_3 in the residual melt and thus delays the saturation of anorthite till a lower pressure and higher solidification degree are reached, resulting in the decrease of the thickness of anorthosite crust. Figure 4.1.1 suggests that the lower limit of the initial Al_2O_3 content should be ~0.8 ×BSE regardless of the initial FeO content. The upper limit of the initial Al_2O_3 content depends on the initial FeO content and varies from less than 1.7 to 2.7 ×BSE for the variation of the initial FeO from 2.3 to 1.0 ×BSE, respectively (Fig. 4.1.1). The estimated crustal thickness is not affected by X_{scfl} for low (<1.3 ×BSE) or high (>2.3 ×BSE) initial Al_2O_3 content, but is thinner for the intermediate content of initial Al_2O_3 (Fig. 4.1.1). Thus, the effect of X_{scfl} is not crucial to the initial Al_2O_3 content of LMO constrained by the observed crustal thickness of ~53 km.

Figure 4.1.2 are contour plots of the estimated crustal thickness, H_{crust} for four values of X_{scfl}. Solid lines in Fig. 4.1.2 show contours for the crustal thickness of 53 km, which define acceptable region in the compositional space of the initial Al_2O_3 and FeO contents. The initial LMO should have a composition capable of forming the crust thicker than the observation, that is, segments of the curves above the broken line in Fig. 4.1.1 are acceptable. The acceptable region is colored in red and unacceptable region is colored in blue in Fig. 4.1.2. The constrained regions in Fig. 4.1.2 for X_{scfl} =0.1 and 0.2 are slightly tighter than those for X_{scfl} =0.4.

Table 4.1

Thickness of lunar crust estimated for various initial LMO compositions listed in the first two columns and suspended crystal fraction limit, X_{scfl}, listed in the third column. The solidification degree of the LMO (Φ_{LMO}) at the time of anorthite crystallization is calculated by MELTS/pMELTS program. The amount of minerals that can be crystallized from melts first saturated with anorthite ("residual melts") is estimated by the CIPW normative method because of difficulties in application of the MELTS algorithm to such fractionated melt compositions. The crustal thickness listed in the last column as H_{crust} is regarded as maximum estimates because of several assumptions, such as 100% complete separation of anorthite from the LMO and no melt trapping in the bottom cumulate pile. See the main text for details of the assumptions. Abbreviations; an: anorthite, ol: olivine, opx: orthopyroxene cpx: clinopyroxene, and lar: larnite.

Assumed conditions			Solidification Degree	Amount of minerals fractionated (vol%)					Max. Crust thick.
FeO (×BSE)	Al_2O_3 (×BSE)	X_{scfl}	Φ_{LMO} (wt%)	an	ol	opx	cpx	lar	H_{crust} (km)
1.0	1.0	0.1	77.2	53.5	13.3	18.2	15.0	0.0	65.9
1.0	1.5	0.1	69.4	58.2	16.2	12.1	13.6	0.0	97.5
1.0	2.0	0.1	68.7	56.8	19.9	5.8	17.5	0.0	99.0
1.0	2.5	0.1	77.2	52.5	27.4	0.0	16.8	3.4	65.4
1.0	1.0	0.4	79.3	55.1	14.5	14.7	15.8	0.0	61.5
1.0	1.5	0.4	78.4	57.9	18.0	10.4	13.8	0.0	68.0
1.0	2.0	0.4	77.7	58.2	19.2	6.3	16.3	0.0	70.5
1.0	2.5	0.4	78.6	54.8	25.4	0.0	15.4	4.4	64.1
1.5	1.0	0.1	76.5	50.3	23.5	12.5	13.7	0.0	63.8
1.5	1.5	0.1	68.7	54.7	24.4	7.2	13.7	0.0	94.7
1.5	2.0	0.1	72.0	51.1	31.1	0.0	16.6	1.3	78.3
1.5	2.5	0.1	85.0	41.1	43.0	0.0	8.0	7.9	32.5
1.5	1.0	0.4	79.3	53.6	23.5	10.3	12.6	0.0	59.9
1.5	1.5	0.4	78.5	55.4	23.3	8.6	12.7	0.0	64.8
1.5	2.0	0.4	78.4	53.8	28.7	0.0	17.2	0.3	63.2
1.5	2.5	0.4	84.4	46.6	35.7	0.0	8.8	9.0	38.6
2.0	1.0	0.1	74.9	47.8	32.8	7.0	12.4	0.0	65.0
2.0	1.5	0.1	68.8	50.2	33.5	1.5	14.7	0.0	86.4
2.0	2.0	0.1	77.1	43.0	42.3	0.0	9.0	5.7	53.8
2.0	1.0	0.4	78.8	51.2	32.2	4.7	11.9	0.0	59.0
2.0	1.5	0.4	78.5	50.4	33.6	1.9	14.1	0.0	58.8
2.0	2.0	0.4	80.5	47.0	37.2	0.0	9.6	6.2	48.3

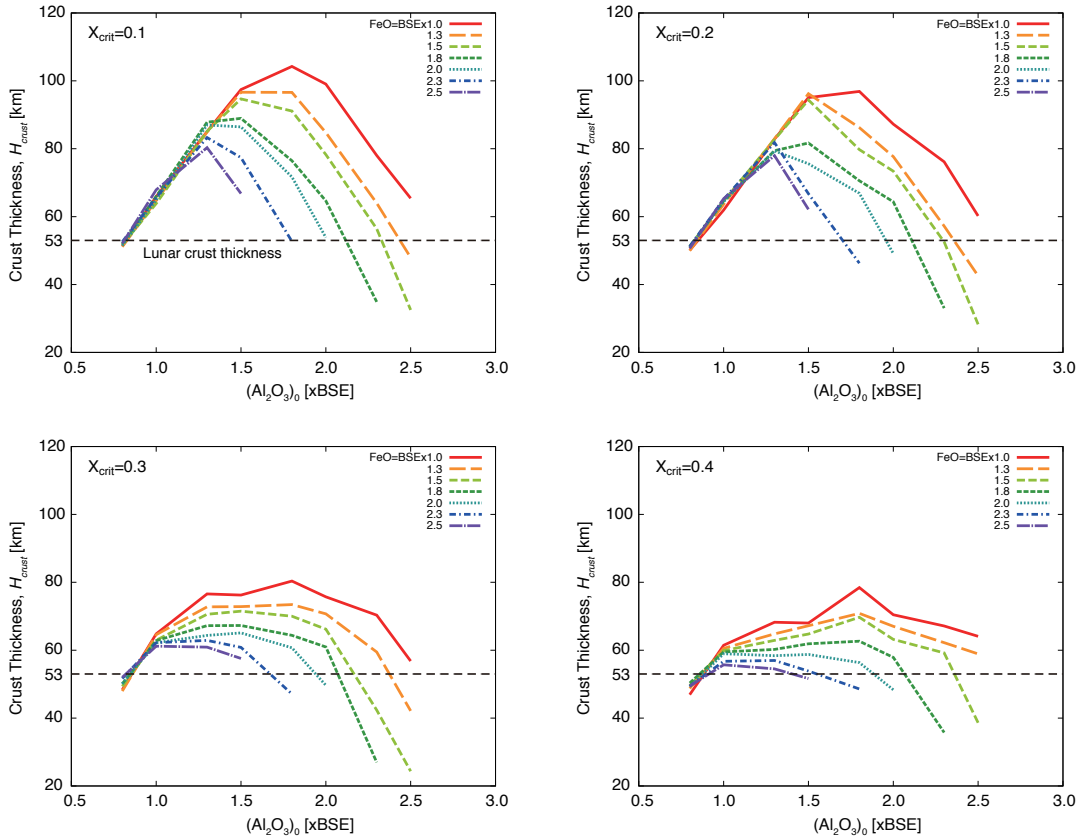

Fig. 4.1.1
Estimated maximum thickness of the lunar crust that consists exclusively of anorthite plotted against Al_2O_3 contents of the initial LMO. Each panel is for different suspended crystal fraction limit, X_{scfl}, and each color and line pattern represents the initial FeO content. Anorthite is assumed to perfectly separate from the LMO. The average crustal thickness of the Moon by the recent exploration of Kaguya (53 km) (Ishihara et al., 2009) is shown by the black broken line. The initial LMO should have a composition capable of forming the crust thicker than the observation, that is, segments of the curves above the broken line are acceptable.

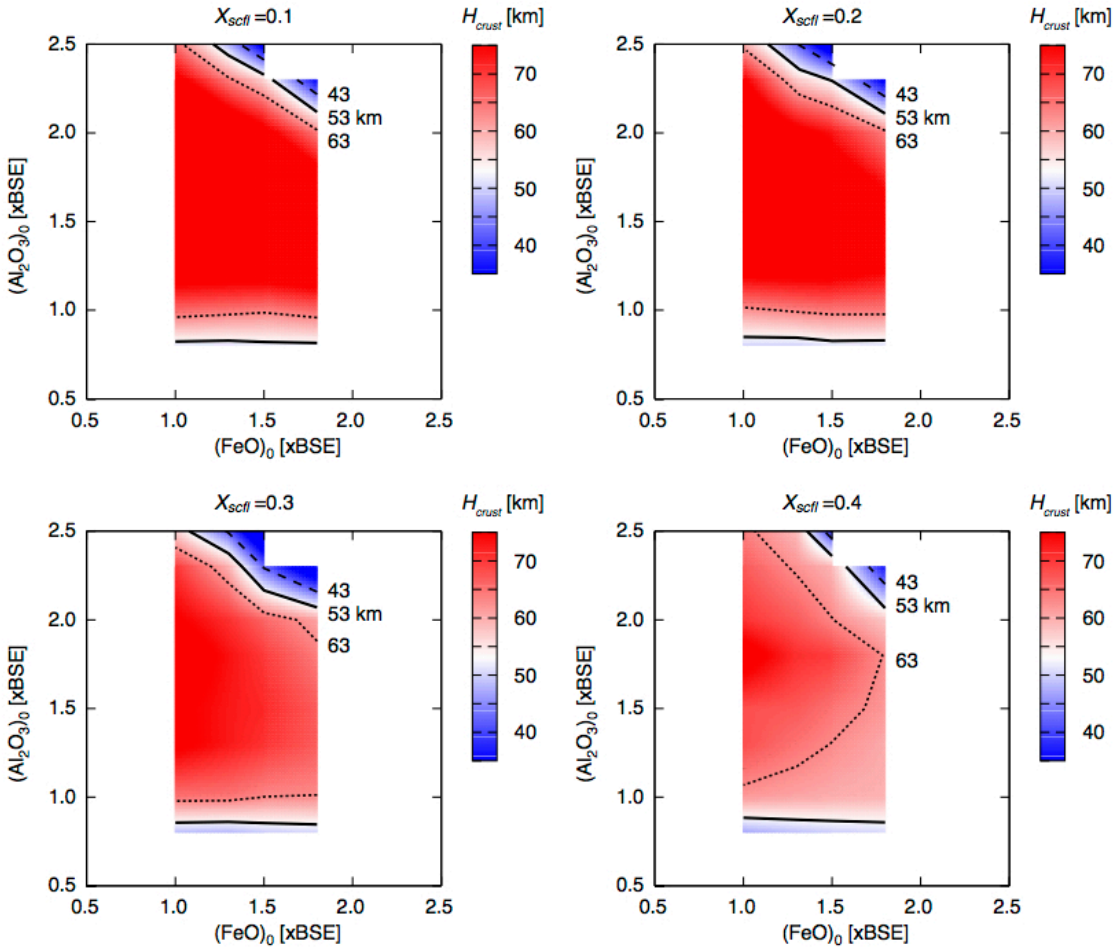

Fig. 4.1.2

Contour plot of calculated crustal thickness, showing a plausible range of FeO and Al_2O_3 contents of the initial LMO (red colored region) constrained by the observed thickness of the lunar crust for four values of suspended crystal fraction limit, X_{scfl}: 0.1, 0.2, 0.3, and 0.4. Color tone represents H_{crust} as shown in the color bars. Blue colored region is unacceptable. Solid lines are the limits of the acceptable region, corresponding to the average thickness of 53km after to the Kaguya lunar exploration. Dotted and dashed curves are ±10km from the average thickness to show sensitivity of the accepted limit.

4.2 Constraint 2: Conditions for anorthite separation in a turbulent LMO

Anorthosite crust formation requires flotation of anorthite in a magma ocean, which implies that at least the LMO melt at the time of anorthite crystallization was denser than anorthite. In order to evaluate this condition, density of the melt at the time of anorthite crystallization for various initial compositions are calculated by using the MELTS program. The results are shown in Table 4.2; the density of the melts at the time of anorthite saturation varies from 2820 to 3110 kg/m^3, which is much greater than the density of anorthite, 2780 kg/m^3. Therefore, anorthite can float to be separated from the LMO if we consider only density as a necessary condition.

This simple density comparison is, however, not enough for the actual crust formation, that is, separation of anorthite from the LMO is not guaranteed when the LMO was vigorously convective. Tonks and Melosh (1990) and Martin and Nokes (1989) discussed that magma ocean in a planetary scale is characterized by an extremely large Rayleigh number (*Ra*) and a small Prantle number (*Pr*), where crystals can be suspended in the melt due to inertial flow independent of the density of melt. The *Ra* and *Pr* of the melt for anorthite crystallization at corresponding temperature and pressure conditions are obtained to be $10^{20\text{-}22}$ and $10^{2\text{-}4}$, respectively. These numbers indicate that the convection even in the late stage of the LMO when anorthite begun to crystallize is as vigorous as the initial LMO. Tonks and Melosh (1990) noted that crystals would separate from a magma ocean only when the convective velocity was much smaller than a terminal velocity of crystals, and discussed the conditions of the crystal separation from LMO. Martin and Nokes (1989), on the other hand, discussed that only crystals that transported to a marginal boundary layer are separated from a turbulent magma body, where the convective velocity becomes nearly zero. The number of crystals exponentially decays in a magma body, if no re-entrainment into the main body takes place and if the temperature of a magma body is kept constant. Solomatov et al. (1993) investigated re-entrainment of crystals in a convective flow based on theoretical consideration and analog experiments, and derived the following condition for crystal entrainment:

$$\left(\frac{\eta\alpha gF}{C_{\mathrm{p}}}\right)^{\frac{1}{2}}\frac{1}{\left|\rho_{\mathrm{melt}}-\rho_{\mathrm{crys}}\right|gD}>0.1 \quad (4.1)$$

where η is the dynamic viscosity, α is the thermal expansion, g is the gravitational acceleration, F is the heat flux at the LMO surface, C_{p} is the isobaric heat capacity, ρ_{melt} and ρ_{crys} are the density of melt and crystal, respectively, and D is the particle diameter.

From eq. (4.1), a critical grain size for separation to the boundary layer of a magma ocean is expressed as follows:

$$D>\frac{10}{\left|\rho_{\mathrm{melt}}-\rho_{\mathrm{crys}}\right|g}\left(\frac{\eta\alpha gF}{C_{\mathrm{p}}}\right)^{\frac{1}{2}}\left(\equiv D_{\mathrm{An}}\right) \quad (4.2)$$

The equation indicates that the minimum size of crystals that separates from a convective LMO is a function of density and viscosity of the magma. Viscosity of the melts at the temperature of anorthite liquidus was calculated based on Shaw (1972), where viscosity is shown by the following equation,

$$\begin{aligned}\ln\eta &= \ln\eta_0+\frac{E}{RT}\\ &= -8.7+\frac{\sum X_i\left(S_i^0\cdot X_{\mathrm{SiO_2}}\right)}{1-X_{\mathrm{SiO_2}}}\left(\frac{10^4}{T}-1.5\right),\end{aligned} \quad (4.3)$$

where X_i is mole fraction of i^{th} component and S_i^0 is an Arrhenius slope for the component (S^0_{SiO2}=0, S^0_{Al2O3}=6.7, S^0_{FeO}=2.1, S^0_{MgO}=3.4, S^0_{CaO}=4.5). Other parameters in eq. (4.2) for LMO are adopted from Solomatov et al. (1993); α=5x10^{-5} K^{-1}, g=1.62 m s^{-2}, ρ_{crys} =2780 kg m^{-3}, F=5x10^5 J m^{-2} s^{-1}, and C_{p}=10^3 J kg^{-1} K^{-1}. The results are also listed in Table 4.2, where viscosity of LMO at the time of anorthite crystallization ranges from ~1 to ~5 Pa s, which are comparative to terrestrial basalts (Bottinga and Weill, 1972; Shaw, 1972).

The critical size for capture of anorthite in the boundary layer, D_{An}, is shown in

Table 4.2 and is plotted against the initial FeO content of LMO in Fig. 4.2.1. The critical size depends on the initial FeO content of the LMO, which is very sensitive to the melt composition with low FeO content (<1.5 ×BSE), because the density of melt with low FeO content is close to that of anorthite (Fig. 3.2c-3c), but not so sensitive for higher FeO content (Fig. 4.2.1). Anorthite crystals with even small size separate from the LMO if the FeO content of the melt is very high. The variation of the initial Al_2O_3 content shifts the relationship between the initial FeO content and D_{An} towards upper right if the initial Al_2O_3 content is in the intermediate range and towards lower left if it is very low or very high in Fig. 4.2.1, although the effect is much smaller than that of the initial FeO content (Fig. 4.2.1). This is attributable to crystallization of anorthite at a lower degree of crystallization for this intermediate range of the initial Al_2O_3 (Fig. 3.2b-3.5b). If fractionation of mafic phases is suppressed, the FeO content in the residual melt becomes lower, which shifts the trend to the right hand side in Fig. 4.2.1 (green dashed curve). Crystallization of spinel at high pressure requires extensive crystallization of mafic minerals to saturate anorthite for higher initial Al_2O_3 of the LMO > 1.5 ×BSE as explained above, which shifts the curve to the left hand side in Fig. 4.2.1 (blue dashed curve).

The results are shown for four values of X_{scfl} in Fig. 4.2.1. They are apparently similar indicating that X_{scfl} does not significantly affects D_{An}. The results show that X_{scfl} does not affect D_{An} if the initial Al_2O_3 is 1.5-2.0 ×BSE, but that an increase in X_{scfl} shifts the trend in Fig. 4.2.1 towards the right hand side by 0.2 if the initial Al_2O_3 is 0.8-1.0 ×BSE or by 0.1 if the initial Al_2O_3 is as high as 2.3 ×BSE.

In order to constrain the FeO content in the initial LMO, we need to know the grain size of anorthite separated from the LMO. Although almost all the highland crustal rocks are heavily brecciated by multiple impacts and the intact grain size of anorthite separated from the residual LMO is hard to know, Wilshire et al. (1972) reported a grain size of anorthite from weakly brecciated Apollo 15 anorthosite 15415, which yields old crystallization age (~4.05±0.15 My). The rock is made of 98 vol% of calcic plagioclase ($An_{\sim 96}$) and shows weak degree of brecciation compared to other highland rocks. The reported maximum size is 1.8cm. The actual grain size of anorthite in the anorthosite might have been increased or reduced through various geological processes. Because size reduction by impact can be identified by mineralogical observation, and because grain reduction by solid-state deformation of the highland

crust is very unlikely, the maximum size in a given anorthosite, which must have been formed by accumulation of anorthite crystals separated from the LMO, can be regarded as maximum value.

Solomatov (1995) theoretically investigated the grain size of crystals in a magma ocean, and concluded that diffusion within melts would be the rate limiting process by fitting the experimental results of dynamic crystallization. The cooling time of LMO before anorthite crystallization has been estimated to be $10^{3\text{-}4}$ yr by Elkins-Tanton et al. (2011), and we have shown the temperature difference from liquidus to anorthite liquidus to be ~400°C in Section 3. Thus, the average cooling rate of LMO before anorthite crystallization is from 10^{-8} to 10^{-9} [K/s]. By applying the Solomatov's model and extrapolating dynamic crystallization experiments in the anorthite-diopside system to this range of cooing rate, we obtain the crystal diameter of $10^{0\text{-}0.5}$ (~ 1-3) cm to be a plausible grain size of anorthite in LMO. These values are roughly equal to the size of 1.8cm estimated in the present work, and it supports the present estimate. Accordingly, without any other critical information, we use the observational size of 1.8 cm in Apollo sample 15415 in the following discussion.

The anorthite grain size of 1.8cm is shown by a horizontal broken line in Fig. 4.2.1. According to the above consideration, anorthite with the size of 1.8 cm could separate from a vigorously convective melt with FeO content below the broken line. In other word, the initial FeO content of the melt should be more than ~1.2-1.4 times of BSE. Figure 4.2.2 are contour plots of the estimated critical size for capture of anorthite in the boundary layer, D_{An}, for four values of X_{scfl}. Solid lines in Fig. 4.2.2 show contours for D_{An} of 1.8 cm, which define an acceptable region in the compositional space of the initial Al_2O_3 and FeO contents. The lower limit of the initial FeO content for anorthite separation is tightly constrained because of the steep slope of the curves for low the initial FeO contents (Figs. 4.2.1 and 4.2.2). As clearly shown by Fig. 4.2.2, the initial Al_2O_3 content and X_{scfl} do not significantly affect this constraint.

The observed crystal size of ~1.8 cm is a conservative estimate, because it is the currently available maximum size in 15415. A smaller grain size of several mm was discussed by Solomatov et al. (1993). If the size of anorthite grains separated from the LMO was smaller than 1.8 cm, the lower limit of the initial FeO content is needed to be much larger. More reliable measurement of anorthite grain size that separated from the LMO to form the lunar crust is needed for stronger constraints.

Table 4.2

Critical size of anorthite separable from a turbulent LMO estimated for various initial LMO compositions listed in the first two columns and suspended crystal fraction limit, X_{scfl}, listed in the third column. The size is estimated by using eq. (4.2) after Solomatov et al. (1993). Input parameters for the eq. (4.2), density and viscosity of the melt at the time of anorthite crystallization, are shown in the 4th and 5th columns, respectively. They are calculated by using the MELTS/pMELTS program and Shaw's equation (Shaw, 1972), respectively.

Assumed conditions			Density of melt	Viscosity of melt	Critical crystal size
FeO (×BSE)	Al_2O_3 (×BSE)	X_{scfl}	ρ (kg/cm^3)	η (Pa s)	D_{An} (cm)
1.0	1.0	0.1	2840	4.2	4.5
1.5	1.0	0.1	2950	2.0	1.0
2.0	1.0	0.1	3030	1.4	0.6
2.5	1.0	0.1	3090	1.1	0.4
1.0	1.5	0.1	2820	3.9	5.6
1.5	1.5	0.1	2910	2.3	1.5
2.0	1.5	0.1	3000	1.6	0.7
2.5	1.5	0.1	3110	1.1	0.4
1.0	2.0	0.1	2830	3.8	4.8
1.5	2.0	0.1	2940	2.1	1.1
2.0	2.0	0.1	3080	1.3	0.5
1.0	1.0	0.4	2820	4.5	7.0
1.5	1.0	0.4	2900	2.4	1.6
2.0	1.0	0.4	2980	1.7	0.8
2.5	1.0	0.4	3030	1.4	0.6
1.0	1.5	0.4	2820	4.1	7.1
1.5	1.5	0.4	2890	2.3	1.7
2.0	1.5	0.4	2980	1.6	0.8
2.5	1.5	0.4	3070	1.3	0.5
1.0	2.0	0.4	2840	3.3	3.6
1.5	2.0	0.4	2910	2.0	1.3
2.0	2.0	0.4	3010	1.9	0.7

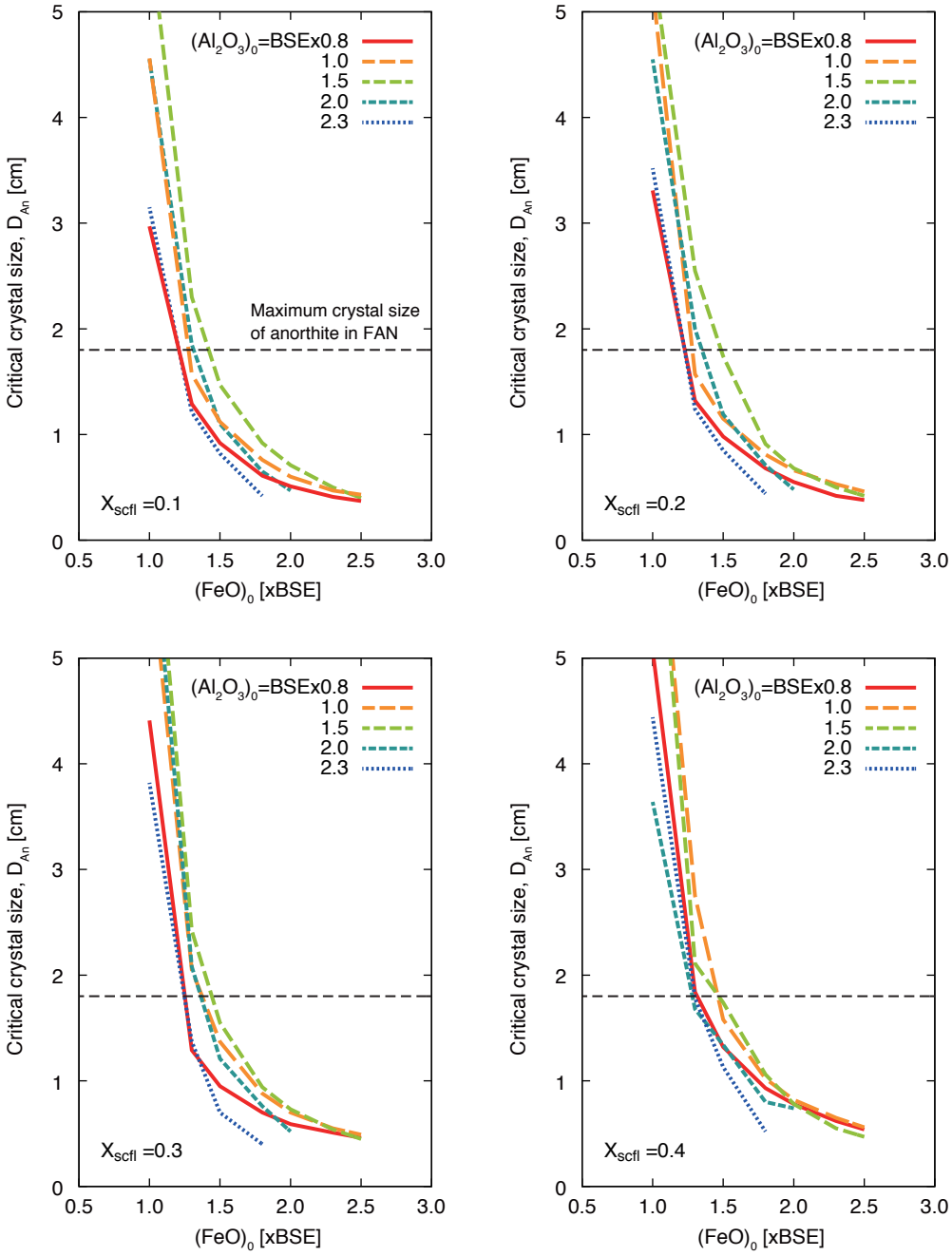

Fig. 4.2.1

Estimated critical crystal size of anorthite, D_{An}, to separate from the convective LMO plotted against FeO contents of the initial LMO. Each panel is for different suspended crystal fraction limit, X_{scfl}, and each color and line pattern represents the initial Al_2O_3 contents. The maximum size of anorthite crystal (1.8 cm) reported so far in the literature (sample 15415: Wilshire et al., 1972) is shown by horizontal broken line. The initial LMO should have a composition capable of forming the anorthosite crust, which requires anorthite flotation. Therefore, segments of the curves below the broken line are acceptable, and the initial melt compositions must be richer in FeO than 1.2 - 1.5 times of BSE for any values of the initial Al_2O_3 content.

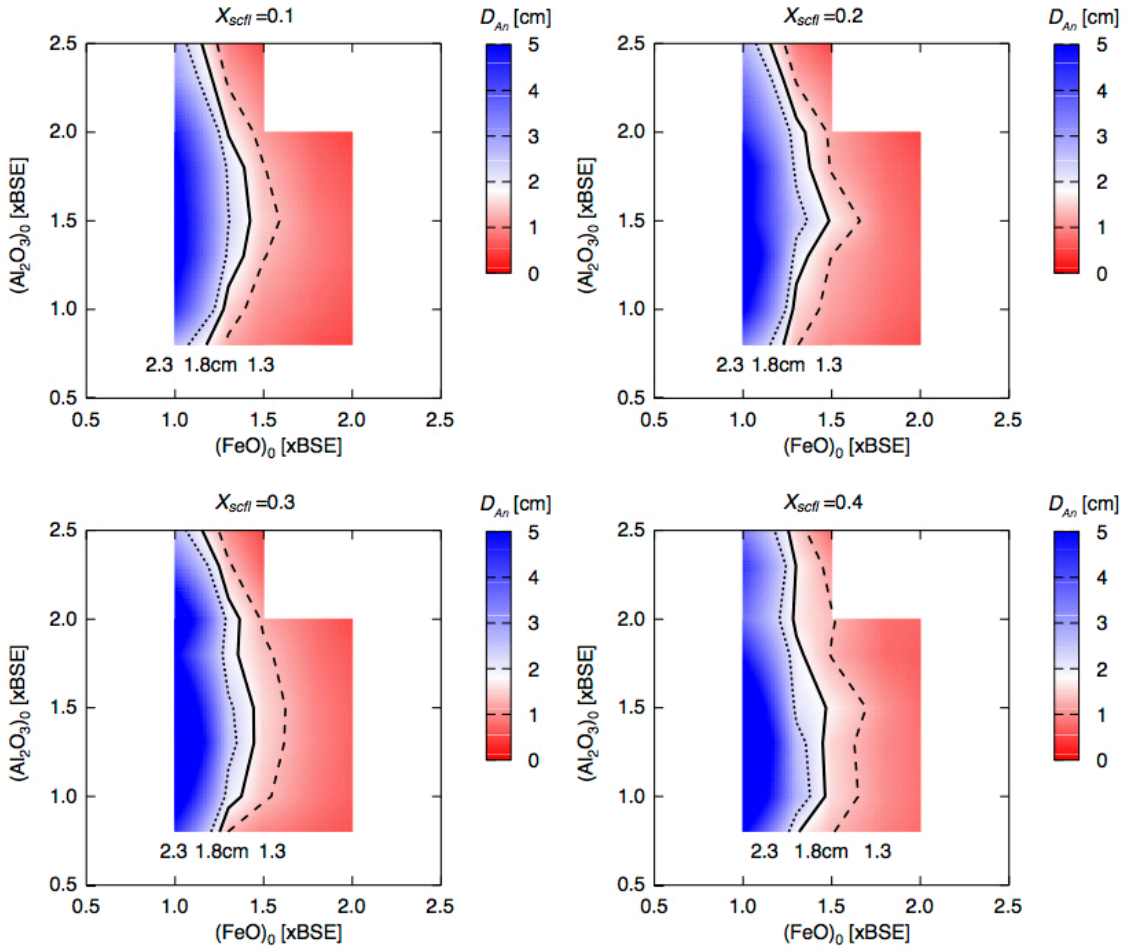

Fig. 4.2.2

Plausible range of FeO and Al_2O_3 contents of the initial LMO (red colored region) constrained by the crystal size of anorthite to separate from the convective LMO (D_{An}) for four values of suspended crystal fraction limit, X_{scfl}: 0.1, 0.2, 0.3, and 0.4. Color tone represents D_{An} as shown in the color bars. Blue colored region is unacceptable. Solid lines are the limits of the acceptable region, corresponding to the maximum anorthite size of 1.8cm after Wilshire et al. (1972). Dotted and dashed curves are ±0.5 cm from the maximum size to show sensitivity of the accepted limit.

4.3 Constraint 3: Major element composition of mafic minerals in crust

The lunar highland crust consists predominantly of anorthite with lesser amounts of mafic minerals including olivine, hypersthene, and augite (Lucey, 2004). These mafic minerals would have crystallized with anorthite in the LMO or from interstitial melt within the crust. The Mg# of the mafic minerals reflects that of the LMO after crystallization of anorthite. Therefore, the Mg# of mafic minerals appeared together with anorthite in the fractional crystallization model should be larger than the observed Mg# of mafic minerals coexisting with anorthosite. The initial LMO compositions listed in Table 2.1 are evaluated whether compositions of mafic minerals crystallize with anorthite is consistent with those observed in the ferroan anorthosite (FAN) suite, which is thought to have formed from the primitive lunar crust due to low abundances of incompatible lithophile elements and very old crystallization age (Borg et al., 1999; Norman et al., 2003).

Table 4.3.1 shows the Mg# of melt at the time of anorthite appearance as a function of initial FeO and Al_2O_3 contents of the LMO. The Mg# of residual melt decreases with increasing initial FeO content, and the dependence on the initial FeO content is larger for larger initial Al_2O_3 content. Moreover, the highest Mg# is attained if the initial Al_2O_3 content of the LMO ranges from 1.3-1.5, which is clearly seen at small X_{scfl} (Fig. 4.3.1 upper left panel). Trends for each initial Al_2O_3 content shifts upwards with decreasing the initial Al_2O_3 from 2.3 ×BSE up to 1.5 ×BSE, but further increase in the initial Al_2O_3 shifts the trend downwards. This is attributable to crystallization of anorthite at a lower degree of crystallization for intermediate range of initial Al_2O_3 (1.3-1.5 ×BSE; Fig. 3.4b-5b). Crystallization of spinel at high pressures requires enhanced crystallization of mafic minerals to saturate anorthite for higher initial Al_2O_3 of the LMO >1.5 ×BSE as explained above. Suppression of fractionation of mafic phases increases the Mg# of the residual melt.

In order to constrain the initial LMO composition, the Mg# of orthopyroxene crystallized with anorthite from the melt is calculated by applying the distribution coefficient of $Kd_{FeO\text{-}MgO}$ ~0.284 between orthopyroxene and melt (Beattie, 1993) (Table 4.3). The calculated value should be higher than that of the most Mg-rich

composition of Mg# ~0.75 of FANs (Warren et al., 1991; Demidova et al., 2007). The Mg# of the melt that crystallizes orthopyroxene with Mg# ~0.75 is ~0.46, which is shown by the horizontal broken line in Fig. 4.3.1. Consequently, Mg# of the LMO that is first saturated with anorthite should be larger than 0.46 in order to crystallize orthopyroxene with Mg# >0.75. If the initial Al_2O_3 content of the LMO is the same as BSE (the orange dashed line), the initial LMO FeO content should be less than 1.5 ×BSE, and if the initial Al_2O_3 content is 1.5 ×BSE (the green line), the FeO content should be less than twice of BSE. These values are conservative constraints, because the previously reported Mg# ~0.75 of orthopyroxene is not necessarily the upper limit and there may be a possibility that the most magnesian orthopyroxene was Mg# >0.75. The recent remote sensing data has reported that the maximum Mg# of mafic minerals in the far-side highland is ~0.75, excepting a rare extreme value of 0.8 (Ohtake et al., 2012). If the orthopyroxene crystallized with anorthite is more magnesian, the allowable range of initial FeO is much tighter than the case of Mg# ~0.75.

The results shown in Fig. 4.3.1 are based on calculations for four values of X_{scfl}. Comparison of the four panels shows that there is essentially no difference if the initial Al_2O_3 content is greater than 1.3 ×BSE. However, Mg# of the anorthite saturated melt increases with increase of X_{scfl}, if the initial Al_2O_3 content is smaller than 1.3 ×BSE. This is explained by the dependence of the FeO content in anorthite saturated melt on X_{scfl} (Fig. 3.6). If X_{scfl} is as high as 0.4-0.6 for a small value of the initial Al_2O_3 content, FeO content of the melt at the anorthite appearance are low and the Mg# is high (Fig. 3.6), because high FeO content corresponds to low Mg# (Fig. 3.2a and 3.3a). This shifts the red solid line towards the right hand side in Fig. 4.3.1 from 1.5 at Mg#=0.46 (X_{scfl} =0.1) to 1.9 ×BSE (X_{scfl} >0.4) in the initial FeO content, but the shift is negligible if the initial Al_2O_3 content is higher than 1.3 ×BSE.

Figure 4.3.2 is a set of contour plots of the estimated Mg# of the melt saturated with anorthite for four values of X_{scfl}. Solid lines in Fig. 4.3.2 show contours for Mg# of the melt of 0.46, which define an acceptable region in the compositional space of the initial Al_2O_3 and FeO contents. The lower upper of the initial FeO content for anorthite separation is tightly constrained because of the steep slope of the curves in Figs. 4.3.1. Thus, the upper limit of the initial FeO content is constrained to be smaller than 1.9 ×BSE for any values of the initial Al_2O_3 and X_{scfl} (Fig. 4.3.2).

Table 4.3
Highest Mg# (Mg/(Mg+Fe)) of orthopyroxene in crustal rocks estimated for various initial LMO compositions listed in the first two columns and suspended crystal fraction limit, X_{scfl}, listed in the third column. The Mg# of melt at the time of anorthite appearance is calculated by our polybaric incremental fractionation model. The Mg# of orthopyroxene crystallized from the melt is estimated by applying the distribution coefficient of $Kd_{FeO\text{-}MgO}$ ~0.284 between orthopyroxene and melt (Beattie, 1993). The value must be highest among crustal rocks, which had been crystallized from magmas underwent various degree of fractional crystallization the anorthite-saturated primitive melt.

Assumed conditions				
FeO (×BSE)	Al_2O_3 (×BSE)	X_{scfl}	Mg# of melt	Mg# of opx
1.0	1.0	0.1	0.60	0.84
1.5	1.0	0.1	0.46	0.75
2.0	1.0	0.1	0.38	0.68
2.5	1.0	0.1	0.34	0.64
1.0	1.5	0.1	0.67	0.88
1.5	1.5	0.1	0.55	0.81
2.0	1.5	0.1	0.45	0.74
2.5	1.5	0.1	0.35	0.65
1.0	2.0	0.1	0.68	0.88
1.5	2.0	0.1	0.52	0.79
2.0	2.0	0.1	0.37	0.67
1.0	1.0	0.4	0.64	0.86
1.5	1.0	0.4	0.52	0.79
2.0	1.0	0.4	0.45	0.74
2.5	1.0	0.4	0.39	0.69
1.0	1.5	0.4	0.66	0.87
1.5	1.5	0.4	0.53	0.80
2.0	1.5	0.4	0.44	0.73
2.5	1.5	0.4	0.38	0.68
1.0	2.0	0.4	0.66	0.87
1.5	2.0	0.4	0.51	0.79
2.0	2.0	0.4	0.45	0.74

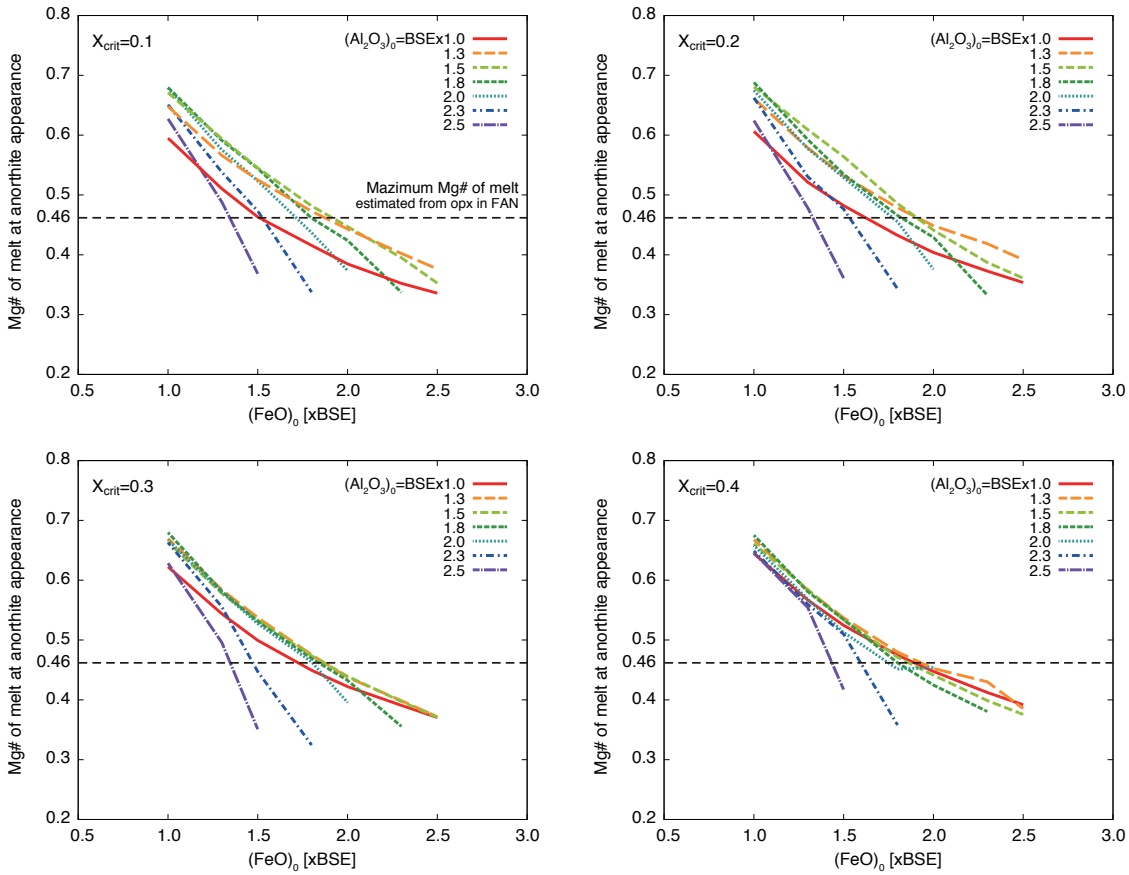

Fig. 4.3.1

Estimated Mg# of the melt at the first appearance of anorthite plotted against various FeO contents of the initial LMO. Each panel is for different suspended crystal fraction limit, X_{scfl}, and each color and line pattern represents the initial Al_2O_3 content. The maximum Mg# of the melt that crystallized orthopyroxene observed in FAN (Mg# = 0.75; Warren et al., 1991; Demidova et al., 2007) is shown by broken line. The initial LMO should have a composition capable of reproducing the highest FAN Mg#. Therefore, segments of the curves above the broken line are acceptable.

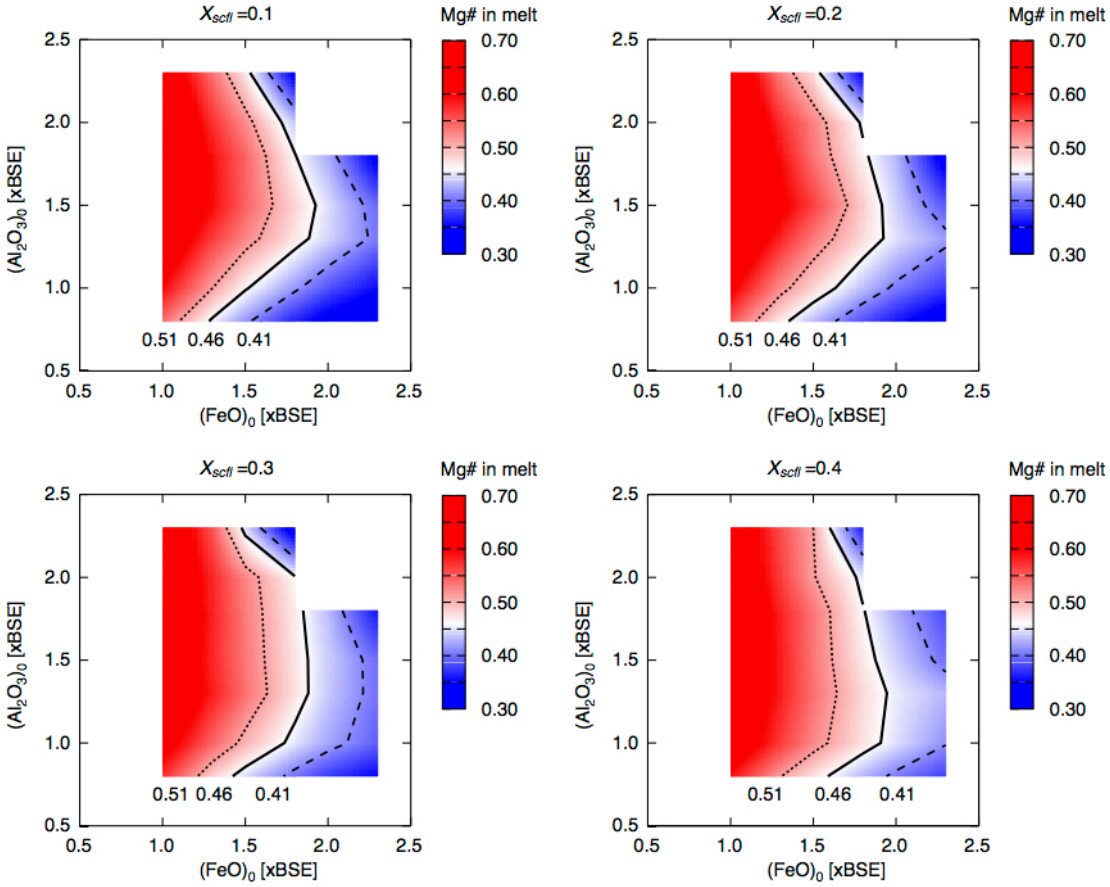

Fig. 4.3.2

Plausible range of FeO and Al_2O_3 contents of the initial LMO (red colored region) constrained by the Mg# of melt at the first appearance of anorthite for LMO for four values of suspended crystal fraction limit, X_{scfl}: 0.1, 0.2, 0.3, and 0.4. Color tone represents Mg# of the melt as shown in the color bars. Blue colored region is unacceptable. Solid lines are the limits of the acceptable region, corresponding to the highest observed Mg# of FAN melt (Warren et al., 1991; Demidova et al., 2007). Dotted and dashed curves are ±0.05 from the highest Mg# to show sensitivity of the accepted limit.

4.4 Constraint 4: Rare earth element composition of anorthite inn ferroan anorthosite (FAN)

本章については、５年以内に雑誌等で刊行予定のため、非公開。

4.5 Summary of constraints

本章については、５年以内に雑誌等で刊行予定のため、非公開。

4.6 Robustness of this model

4.6.1 *Effect of boundary layer fractionation*

The mechanism of chemical differentiation of the cooling LMO adopted in this study is separation of crystals formed in the main part of the vigorously convecting LMO through the bottom flow boundary layers. In this mechanism, efficiency of chemical fractionation depends on efficiency of crystal separation from the main magma body, and we introduced a parameter, suspended crystal fraction limit "X_{scfl}", to model the efficiency of chemical fractionation. The parameter, X_{scfl}, can reproduce any mode of differentiation between pure fractional crystallization and perfect batch crystallization, which are two of the limiting end-member cases for magmatic differentiation in a melt-dominated environment. However, differentiation mechanisms involving double diffusive convection or compositional convection could have been operated in the LMO as proposed by Mores (1982). In this section, we would evaluate roles of compositional convection or double diffusive convection in the chemical evolution of LMO.

In terrestrial magma chambers, separation of residual melt produced within a crystal-dominated wall/bottom/roof boundary layer and mixing with melt in the central magma body is proposed as a crucial process for magmatic differentiation (i.e. “boundary layer fractionation”; Langmuir, 1989; O’Hara and Fry, 1996). Magma chamber is usually formed by emplacement of basaltic melt into continental crust, and located far beneath the surface of the Earth with a few or several dozen kilometers. Several studies of magma chamber demonstrated that the compositional trend of melt generated by boundary layer fractionation is notably different from that formed by crystal separation of a convecting main magma body, which is often called “homogeneous fractionation” (e.g. Langmuir, 1989; Nielsen and DeLong, 1992; Kuritani, 1998, 2004).

Convective exchange of a melt in the main liquid body with a melt in the peripheral mushy layer, driven by density contrast due to compositional difference, was firstly proposed as a plausible differentiation process from laboratory experiments (Huppert and Sparks, 1988; Tait and Jaupart, 1989; Kaneko and Koyaguchi, 2000). Physics of thermal and material transportation in a crystallizing system has been investigated for

various types of thermal boundary conditions such as cooling from the roof, from the floor, or from the side-wall, and various initial conditions, such as a hot heavy liquid suddenly emplaced in a cooler solid with lower melting temperature to simulate a crustal magma chamber. For example, a hot basaltic magma that is emplaced into cold crust to from a magma chamber causes melting of crustal materials at the roof, where silicic magma forms a separate layer with little chemical interaction with the underlying basaltic magma because of their stable density structure (Campbell and Turner, 1987; Huppert and Sparks, 1988). Contrary to this, chimney structures often form in the bottom crystal mush layer and evolved melts can segregate from the boundary layer through chimney and rise through the overlying melt layer as plumes because of its low density. The average composition of the overlying liquid is modified due to mixing with the rising plumes (Tait and Jaupart, 1989; Kaneko and Koyaguchi, 2000).

We will review the experimental study by Kaneko and Koyaguchi (2000) in order to sort out processes involving compositional convection or double diffusive convection and to specify plausible processes operated in the LMO. They conducted experiments with the NH_4Cl-H_2O binary eutectic system to simulate the differentiation of a magma chamber where crystallization of basaltic magma in a main liquid layer is accompanied by melting at both the roof and floor of the magma chamber (Fig. 4.6.1). Their experiments divided into three types: a hot liquid layer is in contact with a cold solid layer at the floor (Exp. 1), the roof (Exp. 2), and both the roof and floor (Exp. 3). In Exp. 1, a mushy layer formed above the solid floor by melting the solid floor and crystallization of the liquid, and the melt generated by melting and crystallization were lighter than the main body of liquid, which drove compositional convection (Fig. 4.6.1A). In Exp. 2, a melt generated by melting of the roof formed a separate layer with negligible mixing with the underlying liquid. The mushy cumulate layer formed at the bottom by separation of the crystals. No convective motion of the interstitial liquid in the bottom mush occurred because of negligible difference of the density between the interstitial melt and the melt in the main body owing to the temperature increase towards the bottom (Fig. 4.6.1B). In Exp. 3, a melt generated by melting of the solid roof formed an upper separate layer without mixing with the underling liquid, and mushy zone generated by melting and crystallization at the floor formed an

underling liquid layer with compositional convection. The compositional convection in the lower liquid region became gradually weaker as the mushy cumulate layer grew, and then, the layers were divided into several double-diffusive convecting layers (Fig. 4.6.1C).

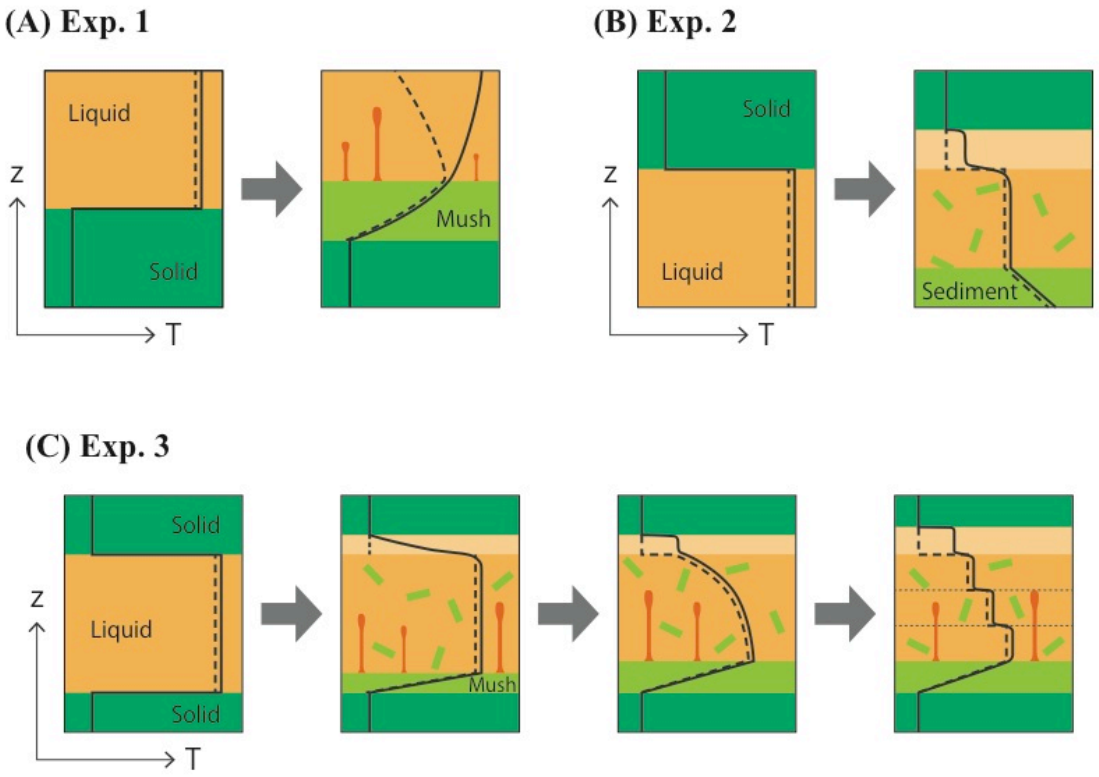

Fig. 4.6.1
Sketch of temperature and compositional profiles of Exp. 1 (A), Exp. 2 (B), and Exp.3 (C), which is modified from Kaneko and Koyaguchi (2000). Solid lines and dashed lines show temperature profiles and liquidus profiles, respectively. A hot liquid layer, shown by obliquely slashed area, is in contact with a cold solid layer, shown by white area, at the floor (Exp. 1), the roof (Exp. 2), and both the roof and floor (Exp. 3). (A) Compositional convection is driven by the evolved melt from the bottom mush layer. (B) Separated layer formed by melting of the solid roof above a main liquid layer. A mushy cumulate layer (shown by shaded area) also formed at the bottom by separation of the crystals. (C) Double-diffusive convection with several layer occurred by melting of the roof and melting and crystallization at the floor after temperature and compositional gradients developed.

The Moon may not have a solid conductive lid until anorthite flotation created the anorthositic crust unless compositional convection forming anorthosite iceberg was operated as proposed by Mores (1982), which may not be the case as discussed below. We may presume that the LMO had a free surface with very thin or no solid layer and was cooled only from the surface. The absence of solid conductive lid is plausible because the Moon-forming giant impact resulted in extremely high temperatures leading to the total melting (Canup, 2004) and because any quenched mafic material would have densities significantly grater than the magma ocean liquids beneath and therefore would sink (Spera, 1992; Elkins-Tanton et al., 2011). The cooling only from surface of the LMO may be reasonable assumption because the extremely high temperature after the giant impact allowed transporting heat in the center of the Moon and storing it there. This tendency is more enhanced if there was core formation. Therefore, the thermal boundary conditions of the LMO are cooling from above through an ephemeral thin basaltic crust and an insulated bottom. The upper boundary condition is similar to that of Exp. 1 of Kaneko and Koyaguchi (2000), which is cooling only from the roof and underlain by mush layer. The bottom boundary condition is rather similar to Exp. 2 of Kaneko and Koyaguchi (2000), which is characterized by hotter mush layer formed by settling and accumulation of crystals.

In this situation, boundary layer fractionation may become effective in the LMO if the following situations relevant to the bottom accumulation zone are satisfied; (1) a mushy layer should stably maintain at the floor boundaries (e.g. Tait and Jaupart, 1989), and (2) low-density fractionated melt is produced by crystallization in the deeper part of a mushy layer, being in significant disequilibrium with the main melt to induce a large density contrast, and is separated and transported through or mixed with the main LMO layer before perfect solidification (e.g. Langmuir, 1989; Kuritani, 1998, 2004; Simura and Ozawa, 2011).

The first condition for the continuous maintenance of mushy layer requires evaluation of initial melt fraction of the mush and rate of compaction. If the initial melt fraction is very small or if compaction is quickly proceeds to squeeze out the trapped melt in the cumulus pile, boundary layer fractionation is totally ineffective. This is the situation that our present model assumes. Initial melt fraction after the crystal accumulation is ~0.5 according to the naturally produced cumulus pile without compaction accompanying deformation of crystals (Simura and Ozawa, 2006).

Therefore, we need to evaluate the time scale of compaction. Approximate estimation can be made according to Richter and McKenzie (1984), who examined compaction of a melt-solid pile with homogeneous initial melt porosity. Important parameters are compaction length (δ_c) defined as follows:

$$\delta_c = \sqrt{\frac{\zeta + \frac{4}{3}\eta}{\mu} k_\phi}\,, \tag{4.6.1}$$

where ζ and η are the bulk and shear viscosities of the solid matrix, μ is the viscosity of the melt, and k_ϕ is the permeability, and compaction time (τ_c) defined as follows:

$$\tau_c = \delta_c \frac{\mu}{k_\phi (1-\phi_0) \Delta\rho g}\,, \tag{4.6.2}$$

where ϕ_0 is the initial melt fraction of the cumulus pile, $\Delta\rho$ is the density contrast of melt and solid, and g is the gravitational acceleration (McKenzie, 1985). For a crystal pile with 50% melt porosity on the depth of 1000km of the LMO, δ_c ~35km and τ_c ~5.0×10^4 yrs are obtained. By using these values, we can estimate the time scale in which melt fraction is reduced to $1/e$ of the initial value is obtained for the depth of cumulus pile with 50% melt porosity of 300, 490, 630, 750 km to be 8, 12, 16, 19 thousands years for X_{scfl} =0.1, 0.2, 0.3, and 0.4, respectively. These time scales are similar or greater than the cooling time scale of the LMO before anorthite crystallization, which is estimated to be on the order of 1000 years (Elkins-Tanton et al., 2011), indicating that cumulus pile is maintained for a long time.

The second condition is difficult to be evaluated because we have little information on physics of evolved melt formation and transportation in the bottom crystal pile of LMO. Therefor, we assume that evolved light melts can be formed and released from the bottom mush. Mores (1982) proposed that evolved melt segregated from the bottom boundary layer was transported through the LMO as compositional plumes without mixing with the host LMO melt in order to realize earlier formation of buoyant iceberg of protocrust. However, the released melt plume from the mush may instantaneously be mixed with vigorously convecting LMO and never reached shallow level as Mores (1982) postulated. Taking these conditions into consideration, we

evaluated effects of boundary layer fractionation by mixing an evolved melt produced in the bottom of the mush and mixed with the overlying LMO melt.

We evaluated roles of the boundary layer fractionation played in chemical evolution of the LMO with a simple model of mass balance (Fig. 4.6.2). Batch crystallization proceeds until a crystal fraction in the LMO reaches the suspended crystal fraction limit, X_{scfl}, as is the case with our incremental fractionation model (Fig. 4.6.2a). The crystals were instantaneously separated to the bottom of the LMO to form a cumulate pile, and the melt trapped by accumulation of crystal was also separated from the main LMO layer (Fig. 4.6.2b). The trapped melt and the main liquid body should have same composition (C_{main}). The amount of the trapped melt is represented by $f_{trap} \times X_{scfl}$ relative to the LMO mass before crystallization, where f_{trap} is a mass ratio of the trapped melt to the total mass of separated crystals ($0 \leq f_{trap} << 1$, near zero). If f_{trap} is zero, then boundary layer fractionation is totally ineffective. The trapped melt was crystallized and fractionated in the mushy layer by cooling, where crystallinity of the trapped melt in the cumulus pile is represented by φ_{trap} (Fig. 4.6.2c) ($0 \leq \varphi_{\mathrm{trap}} \leq 1$). This melt may be partially segregated to the main LMO, but we assume that all the fractionated melt would return to the vigorously convecting LMO and is quickly homogenized, in order to investigate the maximum effect of boundary layer fractionation. Therefore, $(1\text{-}\varphi_{\mathrm{trap}})$ of the trapped melt causes fractionation of the LMO by boundary layer fractionation (Fig. 4.6.2c). For a large value of φ_{trap} (~1), the composition of trapped melt (C'_{trap}) would be significantly fractionated, although it becomes more difficult for the melt to percolate through the mush layer because of the very low melt porosity. For a small value of φ_{trap} (~0), the trapped melt would be little fractionated, which implies that the melt never escaped from the mush layer and stayed there and becomes basaltic component in the lunar mantle.

Simple melt trapping in the bottom cumulus pile without fractionation may also affect the LMO differentiation. This effect would narrow the constrained region determined in this study (Fig. 4.5) along Al_2O_3 axis because of reduction of the amount of CaO and Al_2O_3 needed to form anorthite, the effect of which is essentially the same as to shallow the initial LMO depth. Another effect of melt trapping is tendency to shallow the crystallization depth because of reduction of the amount of residual melt. This would not be so serious because the appearance of anorthosite is governed not only by melt composition but also by pressure as shown in section 3.4.

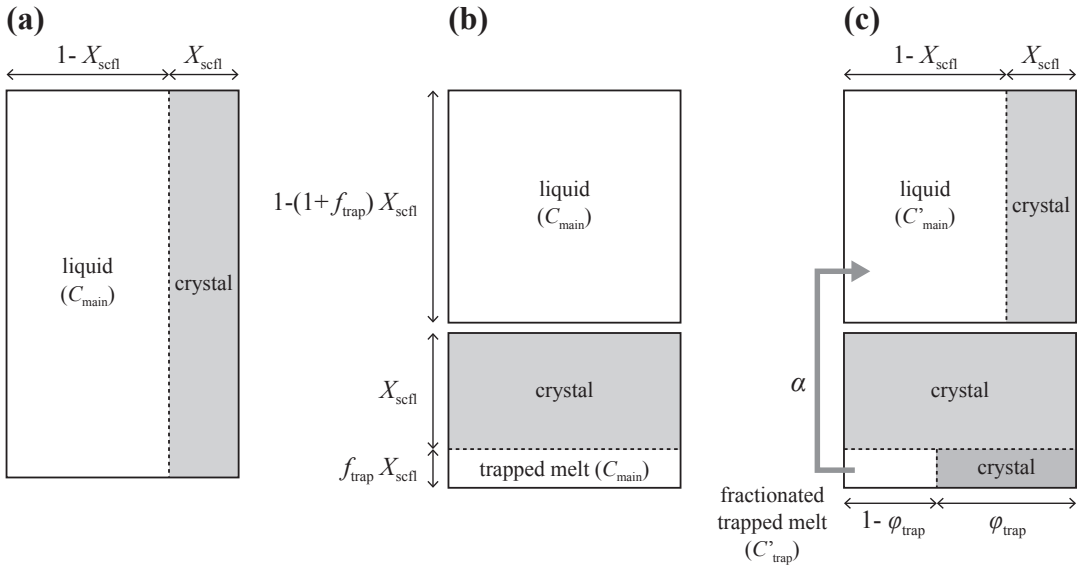

Fig. 4.6.2
Illustration of used calculation scheme to model boundary layer fractionation via cumulus pile on the bottom of the LMO. X_{scfl} is suspended crystal fraction limit, f_{trap} is a mass ratio of the trapped melt to the total mass of separated crystals, φ_{trap} is the crystallinity of the trapped melt in the cumulus pile. See the main text for detail.

Concentration of a component in the main liquid layer (LMO) after the mixing with the fractionated trapped melt (C''_{main}) segregated from the cumulate pile is given by:

$$C''_{\mathrm{main}} = \frac{f_{\mathrm{trap}} X_{scfl}\left(1-\varphi_{\mathrm{trap}}\right)C'_{\mathrm{trap}} + \alpha\left(1-X_{scfl}\right)\left\{1-\left(1+f_{\mathrm{trap}}\right)X_{scfl}\right\}C'_{\mathrm{main}}}{f_{\mathrm{trap}} X_{scfl}\left(1-\varphi_{\mathrm{trap}}\right) + \alpha\left(1-X_{scfl}\right)\left\{1-\left(1+f_{trap}\right)X_{scfl}\right\}}, \qquad (4.6.3)$$

where α is the efficiency of segregation of the trapped melt ($0 \le \alpha \le 1$). Here, we set α to be unity to evaluate the maximum effect of boundary layer fractionation. Figure 4.6.3 shows the effect of the boundary layer fractionation on the chemical evolution of the initial LMO for BSE composition and X_{scfl} =0.4 (black solid line). It is assumed that fractionated melts formed at the bottom of each cumulus pile returns to the LMO, for first and second accumulation stages at 40 and 64% solidification, respectively, are examined (Fig. 4.6.3). We assume that fractionation took place only at the bottom of the boundary layer to see the maximum effect.

The composition of the interstitial melt (C'_{trap}) in mushy layer, which was trapped from the main liquid layer at Φ_{LMO} = 40%, is strongly fractionated with crystallization in the mushy layer (= φ_{trap}) at the bottom of LMO (purple solid lines in Figs. 4.6.3). From eq. (4.6.3), the effect of the boundary layer fractionation on the composition of the main liquid layer can be evaluated (color solid lines; red for a volume ratio of the trapped melt to the total mass of separated crystals, f_{trap}, =0.1, orange for 0.2, light green for 0.3, light blue for 0.4, and blue for 0.5).

The FeO content in LMO with boundary layer fractionation would become richer than that of homogeneous fractionation because of the fractionated melt formed in the cumulate pile is very high in FeO (Fig. 4.6.3a). The Al_2O_3 content in LMO affected by boundary layer fractionation is lower than that of homogeneous fractionation because of the crystallization of garnet in the bottom mush layer (Fig. 4.6.3c). These effects suggest that the constrained region for the bulk composition of the Moon obtained in this study would shift towards the FeO-poor side and narrowing along the Al_2O_3 axis by the involvement of boundary layer fractionation.

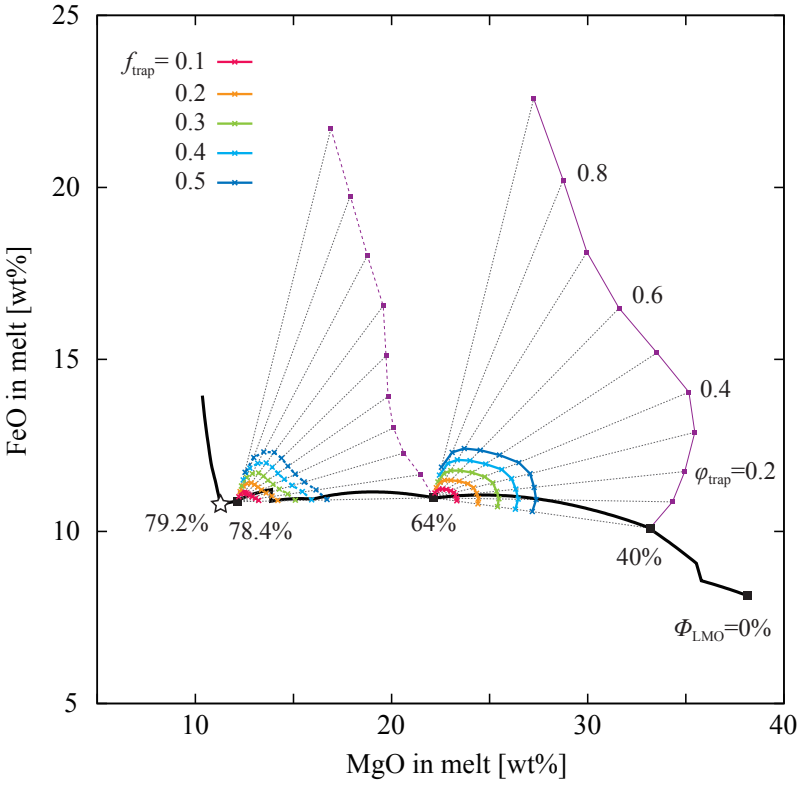
FeO in melt [wt%]
MgO in melt [wt%]
f_{trap}= 0.1
0.2
0.3
0.4
0.5
0.8
0.6
0.4
φ_{trap}=0.2
79.2%
78.4%
64%
40%
Φ_{LMO}=0%

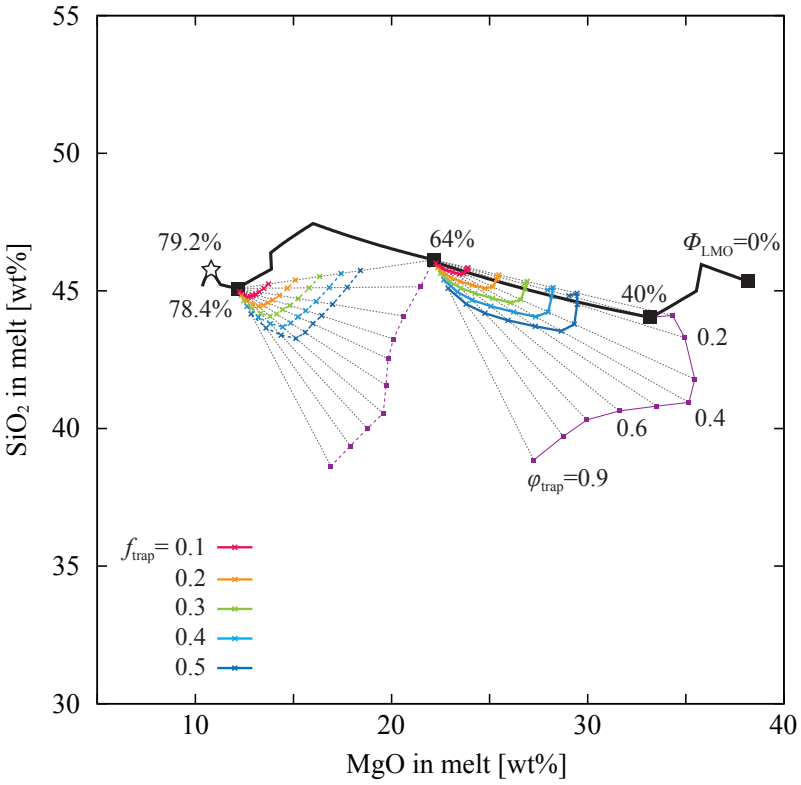
SiO_2 in melt [wt%]
MgO in melt [wt%]
79.2%
78.4%
64%
Φ_{LMO}=0%
40%
0.2
0.4
0.6
φ_{trap}=0.9
f_{trap}= 0.1
0.2
0.3
0.4
0.5

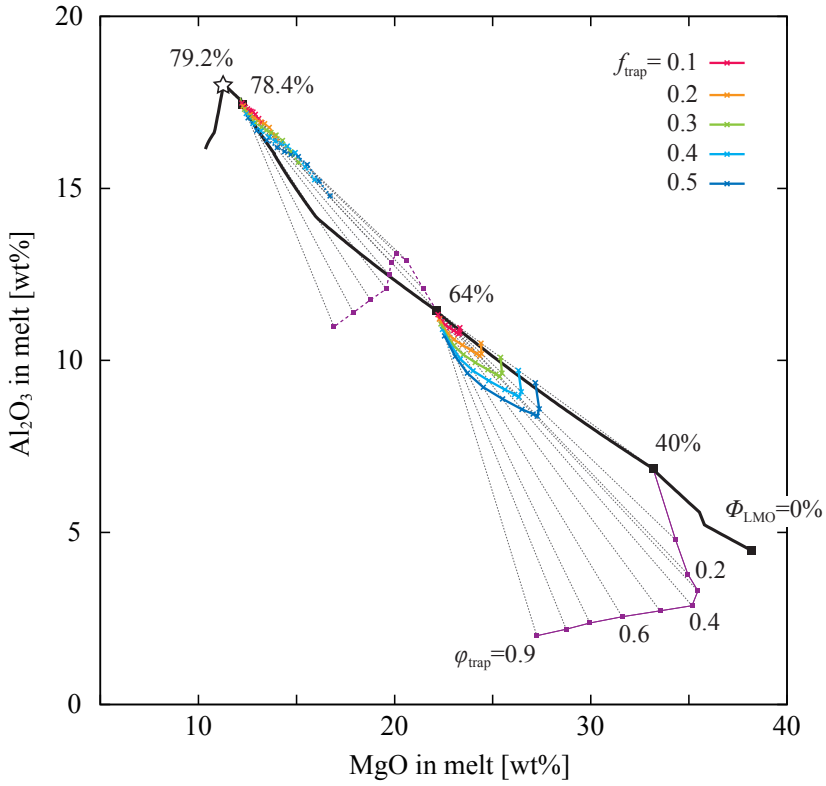
20
15
10
5
0
10
20
30
40
Al2O3 in melt [wt%]
MgO in melt [wt%]
79.2%
78.4%
64%
40%
Φ_LMO=0%
f_trap= 0.1
0.2
0.3
0.4
0.5
φ_trap=0.9
0.6
0.4
0.2

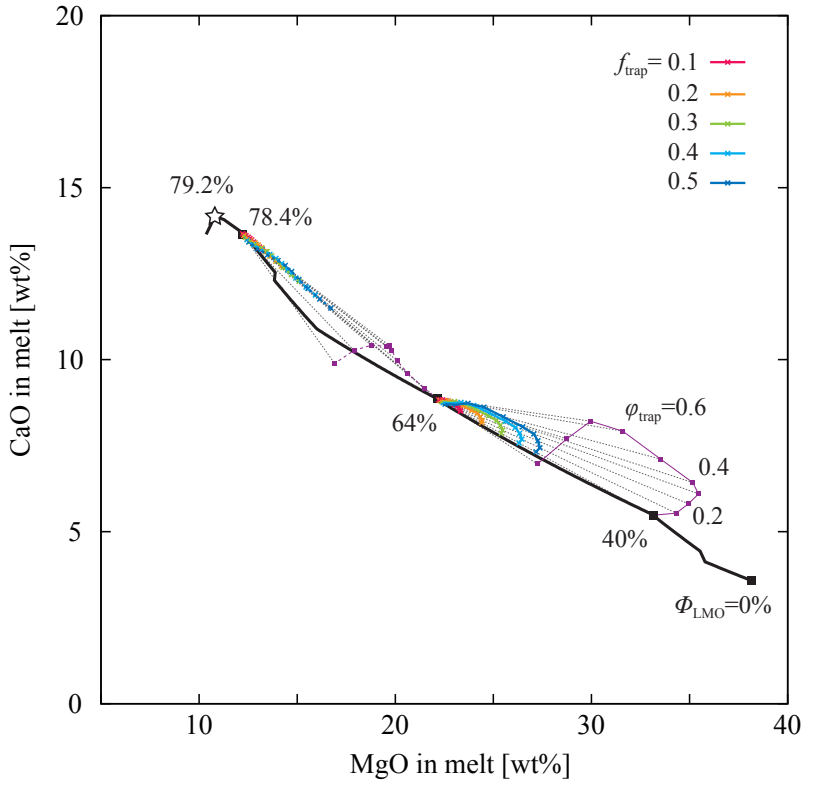
20
15
10
5
0
10
20
30
40
CaO in melt [wt%]
MgO in melt [wt%]
79.2%
78.4%
64%
40%
Φ_LMO=0%
f_trap= 0.1
0.2
0.3
0.4
0.5
φ_trap=0.6
0.4
0.2

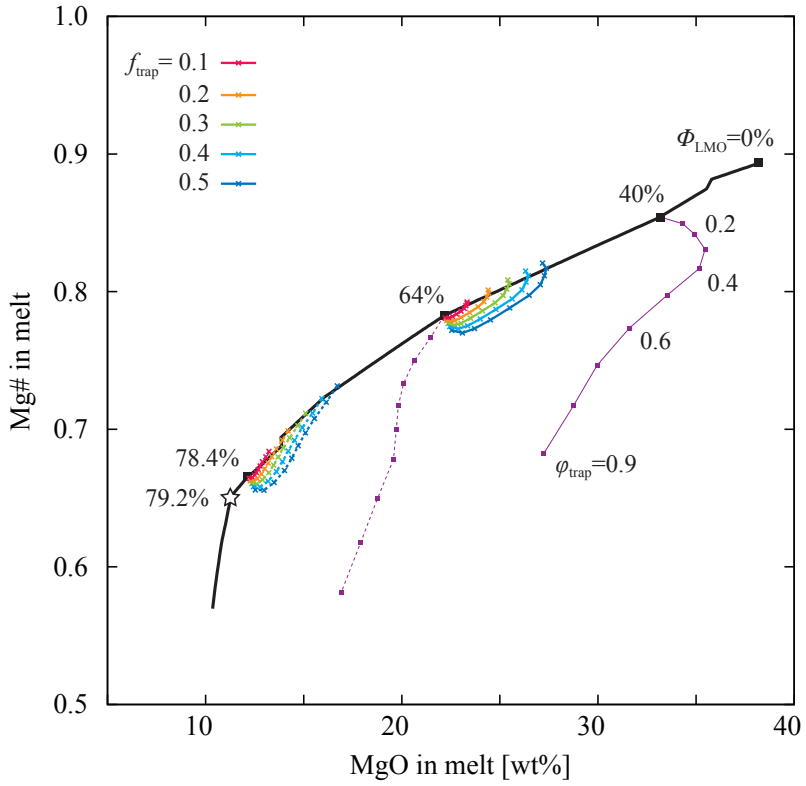

Fig. 4.6.3a,b,c,d,e

Chemical composition of the LMO melt plotted on FeO, SiO_2, Al_2O_3, CaO, and Mg# vs. MgO diagrams. Thick solid line is for polybaric incremental fractional crystallization without boundary layer fractionation, which is the model examined in this study. The star indicates first crystallization of anorthite. Purple lines marking degree of crystallization in the cumulus pile (10% increment) branches out from the solid line at 40 (purple solid line) and 64% (purple dotted line) crystallization of the LMO. They are trends for batch crystallization at the bottom of the cumulus pile formed by instantaneous separation from the LMO. They are mixed with the LMO melt at 64 and 78.4% crystallization along thin black dotted lines. Crosses on the mixing line represent melt composition after complete mixing of the LMO melt with the fractionated melt from the cumulus pile for different values of trapped melt fraction from 0.1 to 0.5 shown by colors.

4.6.2 *Uncertainty of MELTS/pMELTS calculations*

There are several sources for uncertainly of estimation made in this study. One of large uncertainties comes from the chemical equilibrium calculation with MELTS/pMELTS. Although MELTS/pMELTS have been widely used, significant inconsistency has been pointed out for FeO-rich melt (Hirschmann et al., 1998; Ghiorso et al., 2002; El Maarry et al., 2009), and MELTS/pMELTS gives liquidus temperature of orthopyroxene higher by ~100 °C than experimental results for Martian magma (Bertka and Holloway, 1994). If we lower the liquidus temperature of orthopyroxene by 100°C, the density and viscosity of melt would raise by <1 % and ~50 %, respectively for the most FeO rich compositions. The lowering of density and viscosity would change the present estimation by <10 %; for instance, 1.5 xBSE changes to 1.4-1.6 xBSE. Consequently, the error in the MELTS/pMELTS does not alter our conclusion that the FeO content of the initial LMO is higher than that of BSE. The uncertainties in the observations such as the Mg# of pyroxenes in the crust and the grain size of anorthite separated from the turbulent residual LMO, as explained above, shift the constrained region towards the Fe-rich side but never to the Fe-poor side in Fig. 4.5. Again, it does not change the conclusion of high FeO content in the initial LMO.

Chapter 5. Implications

5.1 Origin of the Moon

It has been widely accepted that the Moon was formed by a collision between a protoplanet and the proto Earth (Hartman and Davis, 1975; Cameron and Ward, 1976), which well explains dynamics of the Earth-Moon system, such as the angular momentum and very small inclination of the Moon orbit. The small core of the Moon is also interpreted to be the selective accretion of the core of the impactor to the Earth (Benz et al., 1986, 1987, 1989; Cameron and Benz, 1991; Canup et al., 2001; Canup, 2004). The detail geophysical and geochemical processes of the giant impact, however, still remain unknown, such as the composition of a protoplanet and the proto Earth, physics of impact, and chemical evolution during the formation of the Moon from the circum-Earth disk. Three dynamical models have been suggested for the giant impact: *standard model* (Canup, 2004), *fast-spin model* (Ćuk and Stewart, 2012) and *sub-Earth model* (Canup, 2012). The circum-Earth disk in the standard model is estimated to be partly (~ 20%) evaporated, which originated from the impactor, whereas in other two models, the disk is estimated to be evaporated to significant degree (~80-90%) and the materials are from the upper mantle of the proto Earth. (Nakajima and Stevenson, 2014). The LMO composition, FeO-rich and BSE-like Al_2O_3 contents, constrained in the present study (Fig. 4.5), has important implications for the formation processes of the Moon and the composition of impactor.

Evaporation/condensation in the circum-Earth disk:

The bulk composition of the Moon has been estimated on the basis of the geochemical characteristics. Taylor et al. (2006b) discussed Al_2O_3 enrichment in the Moon on the basis of U and Th concentrations in the crust, and proposed that the refractory elements were enriched during evaporation and condensation processes in a

circum-Earth disk. However, our conclusion is that the Al_2O_3 content of the bulk Moon is similar to that of the Earth's mantle, which is neither consistent with the model by Taylor et al. (2006b) nor requiring any processes to enrich the refractory components. Another our conclusion of selective enrichment of FeO in the Moon cannot be explained by chemical fractionation processes in the circum-Earth disk, either, because the volatility of Fe is similar to Si and Mg (Table 2.2) and selective enrichment of Fe is difficult. Therefore, the bulk composition of the Moon constrained by this study supports the standard model, in which most of the disk materials were derived from the impactor. Suppression of chemical fractionation between highly refractory and moderately refractory elements in the circum-Earth disk is consistent with the results of fluid dynamic numerical simulation for the evolution of a circum planetary disk (Machida and Abe, 2004; Wada et al., 2006). The higher the amount of gas in the disk, the smaller the mass of a satellite. If the disk is evaporated to more than ~70 %, no Moon is formed from the disk since the disk materials fall to the Earth or escape within a few days due to high temperature. Consequently, the fast-spin and sub-Earth models that inevitably produce a vapor rich disk as high as ~ 80 - 90 % are not preferable for our conclusion, and the standard model is appropriate for the Moon formation.

Chemical composition and origin of the impactor:

Previous numerical simulation on the giant impact of lunar formation based on the standard model shows that ~80 % of the material in the circum-Earth disk was derived from the impactor body (Benz et al., 1987; Canup et al., 2001; Canup, 2004), suggesting that the bulk composition of the Moon should reflect that of the impactor body. The bulk composition of the Moon obtained in the present study is compared with that of the Earth and Mars (Wänke and Dreibus, 1994; Lodders and Fegley, 1997; Lodders, 2000) in order to understand the origin of the impactor in Fig. 4.5. The estimated bulk composition of the Moon lies between that of the Earth and Mars, which is rather closer to the Earth (Fig. 4.5). Although the chemical distribution of the protoplanetary disk is still one of the most crucial issues in planetary science, it has been proposed that the degree of oxidation would have increased with distance from the sun on the basis of equilibrium condensation temperature of elements (Wasson and Wetherill, 1979; Wasson, 1988). The hypothesis for the gradual compositional

change of the oxidation state in the protoplanetary disk would imply that the impactor that formed the Moon was originally in the orbit between those of the Earth and Mars.

According to traditional theory of planetary formation, the compositional diversity among the terrestrial planets in the current solar system is the consequence of the systematic radial distribution of the elements in the protoplanetary disk and the mixing of the material during the collision and accumulation of planetesimals and planet embryos. Gravitational interactions between a planet and a protoplanetary disk or a giant planet, however, change the planet's orbit, causing the planet to migrate inward or away from the sun. It is not precisely known how individual planets had experienced orbital changes and where they were initially located. The bulk composition of the Moon constrained in our study should reflect the orbit of the impactor that collided the proto-Earth at the latest stage of planet formation, and will make significant contribution to the future work for the compositional distribution and mixing process in the protoplanetary disk.

5.2 Interior structure after LMO evolution

The LMO composition constrained in the present study also has implications for the interior structure after the solidification of LMO. Figure 5 shows the interior structure formed by the differentiation of the LMO with the typical composition in the constrained region (1.3 ×BSE for FeO and 0.9 ×BSE for Al_2O_3 shown as Table 4.5). The mantle formed before the crystallization of anorthite is estimated by the differentiation model with MELTS calculations, and the shallower part formed after the anorthite saturation is estimated with the CIPW norm calculation. Formation of this mantle accompanies the following constraints: (1) the maximum crustal thickness of ~57 km, which is thicker than the necessary value of ~52 km, (2) the minimum crystal size floated in the LMO of ~ 1.6 cm, which is smaller than the currently obtained maximum size of 1.8 cm, (3) Mg# of the melt at the first appearance of anorthite of ~0.50, which is higher than the present constraint of 0.46, and (4) the amount of crystallized and separated clinopyroxene before the crust formation of ~2.8 wt%, which is lower than the upperlimit of the present work of 4 wt%.

The estimated interior structure shown in Fig. 5 serves as the initial condition for the late stage lunar evolution, such as mantle overturn and mare magmatism. The mantle overturn has been proposed from the age gap between mare basalts and highland rocks (Nyquist and Shih, 1992; Hiesinger et al., 2000, 2003, 2010) and from the inverse correlation between the Ti concentration and depth of source region of the mare Ti basalts (Ringwood and Kesson, 1977; Shearer and Papike, 1993; Hess and Parmentier, 1995; Zhong et al., 2000). Although dynamics of the mantle overturn cannot be quantitatively discussed without the mode and flux of heat transport, the presently modeled internal structure just after the LMO solidification is characterized by a large density gap between the light upper most mantle (~3200 kg/m^3) and heavier overlying crust (~3500 kg/m^3) (Fig. 5) and can be a trigger for the mantle overturn. Titanium, which is not considered in this study, tends to accentuate the density gap and thus enhance the overturn because of the crystallization of heavy oxide minerals, such as ilmenite, in the latest stage of LMO solidification. The interior structure described in the present LMO differentiation model would give crucial constraints for future studies on the later lunar evolution.

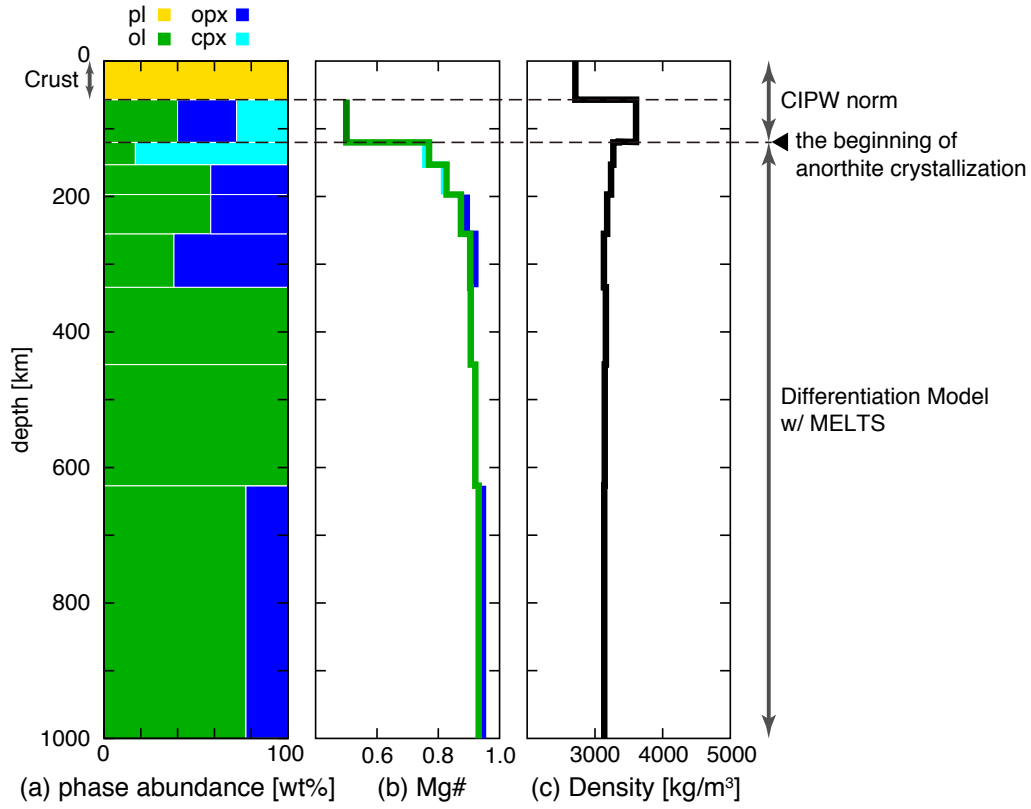

Fig. 5

Expected interior structure formed by the differentiation of the LMO with the typical composition in the constrained region (1.3 ×BSE for FeO and 0.9 ×BSE for Al_2O_3 as listed in Table 4.5) in terms of phase proportion (a), Mg# of mafic minerals (b), and density (c). The main deeper part formed before anorthite begins to crystallize is estimated by our differentiation model with MELTS calculations, and the shallower part formed after the appearance of anorthite is estimated by the CIPW norm calculations.

Chapter 6. Conclusions

To evaluate a plausible range of the initial composition of the lunar magma ocean, we have developed a fluid dynamic and thermodynamic model and investigated a broad range of initial LMO composition with special focus on the FeO and Al_2O_3 contents. The efficiency of crystal separation from LMO affects the chemical composition, extent of mafic phase crystallization and fractionation, and the depth of the LMO at the first appearance of anorthite if the initial Al_2O_3 is smaller than 1.3 ×BSE. With increasing initial Al_2O_3 content in the LMO, the amount of mafic minerals crystallized before saturation in the anorthite component decreases (0.8-1.5 ×BSE), but increases by further increase in the initial Al_2O_3 content (> 1.5 ×BSE), which is attributable to spinel crystallization at high pressure to decrease Al_2O_3 content in the melt.

The results of thermodynamic calculation were evaluated for the following observations; (1) the amount of anorthite, which crystallized from the residual melt, is abundant enough to form the lunar crust, (2) composition of the orthopyroxene coexisting with anorthite is consistent with that of lunar highland rocks, (3) anorthite separated from the turbulent LMO, and (4) the rare earth elements (REE) composition of the LMO is consist with that observed in the parent magma of the lunar highland rocks. A allowable range of FeO and Al_2O_3 contents of the bulk LMO is successfully constrained to be FeO-rich and BSE-like Al_2O_3 contents, where the lower limit of the initial FeO content is ~1.3 ×BSE from the condition of the anorthite separation from the turbulent LMO. The upper limit of the initial FeO content is constrained to be less than 1.9 ×BSE for any values of the initial Al_2O_3 and the mode of differentiation from the condition of the maximum Mg# of orthopyroxene in FAN. The lower limit of the initial Al_2O_3 of the LMO is constrained to be more than 0.8 ×BSE in order to reproduce the observed lunar crustal thickness. The upper limit of the initial Al_2O_3 content is constrained to be less than 1.1 ×BSE from the condition of the REE pattern of the parent melt of FAN rocks. The FeO content is constrained to be more than 1.3 ×BSE and less than 1.8 ×BSE, if the Al_2O_3 content of the Moon is comparable to that of the Earth. These upper and lower limits of the FeO contents are positively correlated with X_{scfl}.

In summary, the range of the FeO and Al2O3 content of the LMO constrained in this study is 1.2-1.8 ×BSE for FeO and 0.8-1.1 ×BSE for Al_2O_3 and lies between that of the Earth and Mars. This emphasizes an importance of simultaneous estimation of the bulk abundances of FeO and Al_2O_3, significance of which has been overlooked in most of the previous studies. The bulk composition of the Moon constrained in our study may provide the possibility of the estimate for the orbit of the impactor that collided the proto-Earth at the last stage of the planet formation.

References

Allègre, C.J., Poirier, J.-P., Humler, E., Hofmann, A.W., 1995. The chemical composition of the Earth. Earth and Planetary Science Letters 134, 515-526.

Anders, E., Grevesse, N., 1989. Abundances of the elements: Meteoritic and solar. Geochimica et Cosmochimica Acta 53, 197-214.

Andrade, E.d.C., 1952. Viscosity of liquids. Proceedings of the Royal Society of London. Series A, Mathematical and Physical Sciences, 36-43.

Asimow, P.D., Ghiorso, M.S., 1998. Algorithmic modifications extending MELTS to calculate subsolidus phase relations. American Mineralogist 83, 1127-1132.

Beattie, P., 1993. Olivine-melt and orthopyroxene-melt equilibria. Contributions to Mineralogy and Petrology 115, 103-111.

Benz, W., Cameron, A., Melosh, H., 1989. The origin of the Moon and the single-impact hypothesis III. Icarus 81, 113-131.

Benz, W., Slattery, W., Cameron, A., 1986. The origin of the Moon and the single-impact hypothesis I. Icarus 66, 515-535.

Benz, W., Slattery, W., Cameron, A., 1987. The origin of the Moon and the single-impact hypothesis, II. Icarus 71, 30-45.

Bertka, C.M., Holloway, J.R., 1994. Anhydrous partial melting of an iron-rich mantle I: subsolidus phase assemblages and partial melting phase relations at 10 to 30 kbar. Contributions to Mineralogy and Petrology 115, 313-322.

Borg, L., Norman, M., Nyquist, L., Bogard, D., Snyder, G., Taylor, L., Lindstrom, M., 1999. Isotopic studies of ferroan anorthosite 62236: a young lunar crustal rock from a light rare-earth-element-depleted source. Geochimica et cosmochimica acta 63, 2679-2691.

Borg, L., Shearer, C., Nyquist, L., Norman, M., 2002. Isotopic constraints on the origin of lunar ferroan anorthosites, Lunar and Planetary Institute Science Conference Abstracts, p. 1396.

Bottinga, Y., Weill, D.F., 1972. The viscosity of magmatic silicate liquids; a model calculation. American Journal of Science 272, 438-475.

Boyet, M., Carlson, R.W., 2007. A highly depleted moon or a non-magma ocean origin for the lunar crust? Earth and Planetary Science Letters 262, 505-516.

Buck, W.R., Toksoz, M.N., 1980. The bulk composition of the Moon based on geophysical constraints, Lunar and Planetary Science Conference Proceedings, pp. 2043-2058.

Cameron, A., Benz, W., 1991. The origin of the Moon and the single impact hypothesis IV. Icarus 92, 204-216.

Cameron, A.G., Ward, W.R., 1976. The origin of the Moon, Lunar and Planetary Institute Science Conference Abstracts, p. 120.

Campbell, I., Turner, J., 1987. A laboratory investigation of assimilation at the top of a basaltic magma chamber. The Journal of Geology, 155-172.

Canup, R.M., 2004. Simulations of a late lunar-forming impact. Icarus 168, 433-456.

Canup, R.M., 2012. Forming a Moon with an Earth-like composition via a giant impact. Science 338, 1052-1055.

Canup, R.M., Ward, W.R., Cameron, A., 2001. A scaling relationship for satellite-forming impacts. Icarus 150, 288-296.

Carlson, R.W., Lugmair, G.W., 1988. The age of ferroan anorthosite 60025: oldest crust on a young Moon? Earth and Planetary Science Letters 90, 119-130.

Ćuk, M., Stewart, S.T., 2012. Making the Moon from a fast-spinning Earth: A giant impact followed by resonant despinning. Science 338, 1047-1052.

Demidova, S.I., Nazarov, M.A., Lorenz, C.A., Kurat, G., Brandstätter, F., Ntaflos, T., 2007. Chemical composition of lunar meteorites and the lunar crust. Petrology 15, 386-407.

Dingwell, D., Courtial, P., Giordano, D., Nichols, A., 2004. Viscosity of peridotite liquid. Earth and Planetary Science Letters 226, 127-138.

Dowty, S., Keil, K., Prinz, M., Gros, J., Takahashi, H., 1976. Meteorite-free Apollo 15 crystalline KREEP, Lunar and Planetary Science Conference Proceedings, pp. 1833-1844.

El Maarry, M.R., Gasnault, O., Toplis, M.J., Baratoux, D., Dohm, J.M., Newsom, H.E., Boynton, W.V., Karunatillake, S., 2009. Gamma-ray constraints on the chemical composition of the martian surface in the Tharsis region: A signature of partial melting of the mantle? Journal of Volcanology and Geothermal Research 185, 116-122.

Elardo, S.M., Draper, D.S., Shearer Jr, C.K., 2011. Lunar Magma Ocean crystallization

revisited: Bulk composition, early cumulate mineralogy, and the source regions of the highlands Mg-suite. Geochimica et Cosmochimica Acta 75, 3024-3045.

Elkins-Tanton, L.T., 2012. Magma Oceans in the Inner Solar System. Annual Review of Earth and Planetary Sciences 40, 113-139.

Elkins-Tanton, L.T., Burgess, S., Yin, Q.-Z., 2011. The lunar magma ocean: Reconciling the solidification process with lunar petrology and geochronology. Earth and Planetary Science Letters 304, 326-336.

Floss, C., James, O.B., McGee, J.J., Crozaz, G., 1998. Lunar ferroan anorthosite petrogenesis: Clues from trace element distributions in FAN subgroups. Geochimica et Cosmochimica Acta 62, 1255-1283.

Gans, R.F., 1972. Viscosity of the Earth's core. Journal of Geophysical Research 77, 360-366.

Ghiorso, M.S., Hirschmann, M.M., Reiners, P.W., Kress, V.C., 2002. The pMELTS: A revision of MELTS for improved calculation of phase relations and major element partitioning related to partial melting of the mantle to 3 GPa. Geochemistry, Geophysics, Geosystems 3, 1-35.

Ghiorso, M.S., Sack, R.O., 1995. Chemical mass transfer in magmatic processes IV. A revised and internally consistent thermodynamic model for the interpolation and extrapolation of liquid-solid equilibria in magmatic systems at elevated temperatures and pressures. Contributions to Mineralogy and Petrology 119, 197-212.

Green, T., Blundy, J., Adam, J., Yaxley, G., 2000. SIMS determination of trace element partition coefficients between garnet, clinopyroxene and hydrous basaltic liquids at 2-7.5 GPa and 1080-1200 C. Lithos 53, 165-187.

Hart, S.R., Dunn, T., 1993. Experimental cpx/melt partitioning of 24 trace elements. Contributions to Mineralogy and Petrology 113, 1-8.

Hartmann, W.K., Davis, D.R., 1975. Satellite-sized planetesimals and lunar origin. Icarus 24, 504-515.

Haskin, L., Warren, P., 1991. Lunar chemistry. Lunar sourcebook, 357-474.

Haskin, L.A., Lindstrom, M.M., Salpas, P.A., Lindstrom, D.J., 1981. On compositional variations among lunar anorthosites, Lunar and Planetary Science Conference Proceedings, pp. 41-66.

Hess, P., Parmentier, E., 1995. A model for the thermal and chemical evolution of the

Moon's interior: Implications for the onset of mare volcanism. Earth and Planetary Science Letters 134, 501-514.

Hiesinger, H., Head, J., Wolf, U., Jaumann, R., Neukum, G., 2010. Ages and stratigraphy of lunar mare basalts in Mare Frigoris and other nearside maria based on crater size‐frequency distribution measurements. Journal of Geophysical Research: Planets (1991–2012) 115.

Hiesinger, H., Head, J., Wolf, U., Jaumann, R., Neukum, G., 2003. Ages and stratigraphy of mare basalts in oceanus procellarum, mare nubium, mare cognitum, and mare insularum. Journal of Geophysical Research: Planets (1991–2012) 108.

Hiesinger, H., Jaumann, R., Neukum, G., Head, J.W., 2000. Ages of mare basalts on the lunar nearside. Journal of Geophysical Research: Planets (1991-2012) 105, 29239-29275.

Hirschmann, M.M., Ghiorso, M.S., Wasylenki, L.E., Asimow, P.D., Stolper, E.M., 1998. Calculation of peridotite partial melting from thermodynamic models of minerals and melts. I. Review of methods and comparison with experiments. Journal of Petrology 39, 1091-1115.

Huppert, H.E., Sparks, R.S.J., 1988. Melting the roof of a chamber containing a hot, turbulently convecting fluid. Journal of Fluid Mechanics 188, 107-131.

Ida, S., Canup, R.M., Stewart, G.R., 1997. Lunar accretion from an impact-generated disk. Nature 389, 353-357.

Ishihara, Y., Goossens, S., Matsumoto, K., Noda, H., Araki, H., Namiki, N., Hanada, H., Iwata, T., Tazawa, S., Sasaki, S., 2009. Crustal thickness of the Moon: Implications for farside basin structures. Geophysical Research Letters 36.

Johnson, K.T., 1998. Experimental determination of partition coefficients for rare earth and high-field-strength elements between clinopyroxene, garnet, and basaltic melt at high pressures. Contributions to Mineralogy and Petrology 133, 60-68.

Jolliff, B.L., Gillis, J.J., Haskin, L.A., Korotev, R.L., Wieczorek, M.A., 2000. Major lunar crustal terranes: Surface expressions and crust‐mantle origins. Journal of Geophysical Research: Planets (1991-2012) 105, 4197-4216.

Jones, J.H., Delano, J.W., 1989. A three-component model for the bulk composition of the Moon. Geochimica et Cosmochimica Acta 53, 513-527.

Kamata, S., Sugita, S., Abe, Y., Ishihara, Y., Harada, Y., Morota, T., Namiki, N., Iwata, T., Hanada, H., Araki, H., 2013. Viscoelastic deformation of lunar impact basins:

Implications for heterogeneity in the deep crustal paleo‐thermal state and radioactive element concentration. Journal of Geophysical Research: Planets.

Kaneko, K., Koyaguchi, T., 2000. Simultaneous crystallization and melting at both the roof and floor of crustal magma chambers: Experimental study using NH_4Cl-H_2 O binary eutectic system. Journal of Volcanology and Geothermal Research 96, 161-174.

Keihm, S., Langseth, M., 1977. Lunar thermal regime to 300 km, Lunar and Planetary Science Conference Proceedings, pp. 499-514.

Khan, A., Maclennan, J., Taylor, S.R., Connolly, J.A.D., 2006. Are the Earth and the Moon compositionally alike? Inferences on lunar composition and implications for lunar origin and evolution from geophysical modeling. Journal of Geophysical Research 111.

Khan, A., Mosegaard, K., Rasmussen, K.L., 2000. A new seismic velocity model for the Moon from a Monte Carlo inversion of the Apollo lunar seismic data. Geophysical Research Letters 27, 1591-1594.

Kokubo, E., Yoshinaga, K., Makino, J., 1998. On a time‐symmetric Hermite integrator for planetary N‐body simulation. Monthly Notices of the Royal Astronomical Society 297, 1067-1072.

Korotev, R.L., 2000. The great lunar hot spot and the composition and origin of the Apollo mafic ("LKFM") impact‐melt breccias. Journal of Geophysical Research: Planets (1991-2012) 105, 4317-4345.

Kraichnan, R.H., 1962. Turbulent thermal convection at arbitrary Prandtl number. Physics of Fluids 5, 1374.

Kuritani, T., 1998. Boundary layer crystallization in a basaltic magma chamber: evidence from Rishiri Volcano, northern Japan. Journal of Petrology 39, 1619-1640.

Kuritani, T., 2004. Magmatic differentiation examined with a numerical model considering multicomponent thermodynamics and momentum, energy and species transport. Lithos 74, 117-130.

Kushiro, I., 1969. The system forsterite-diopside-silica with and without water at high pressures. Am. J. Sci 267, 269-294.

Kushiro, I., 1986. Viscosity of partial melts in the upper mantle. Journal of Geophysical Research 91, 9343-9350.

Kushiro, I., 2001. Partial melting experiments on peridotite and origin of mid-ocean ridge

basalt. Annual Review of Earth and Planetary Sciences 29, 71-107.

Kuskov, O., Kronrod, V., 1998. Constitution of the Moon: 5. Constraints on composition, density, temperature, and radius of a core. Physics of the earth and planetary interiors 107, 285-306.

Langmuir, C.H., 1989. Geochemical consequences of in situ crystallization. Nature 340, 199-205.

Langseth, M.G., Keihm, S.J., Peters, K., 1976. Revised lunar heat-flow values, Lunar and Planetary Science Conference Proceedings, pp. 3143-3171.

Lodders, K., 2000. An oxygen isotope mixing model for the accretion and composition of rocky planets, From Dust to Terrestrial Planets. Springer, pp. 341-354.

Lodders, K., 2003. Solar system abundances and condensation temperatures of the elements. The Astrophysical Journal 591, 1220.

Lodders, K., Fegley Jr, B., 1997. An oxygen isotope model for the composition of Mars. Icarus 126, 373-394.

Lognonné, P., 2005. Planetary seismology. Annu. Rev. Earth Planet. Sci. 33, 571-604.

Lognonné, P., Gagnepain-Beyneix, J., Chenet, H., 2003. A new seismic model of the Moon: implications for structure, thermal evolution and formation of the Moon. Earth and Planetary Science Letters 211, 27-44.

Longhi, J., 1977. Magma oceanography: II. Chemical evolution and crustal formation, Lunar and Planetary Science Conference Proceedings, pp. 601-621.

Longhi, J., 1981. Preliminary modeling of high pressure partial melting: Implications for early lunar differentiation, Lunar and Planetary Science Conference Proceedings, pp. 1001-1018.

Longhi, J., 1992. Origin of picritic green glass magmas by polybaric fractional fusion, Lunar and Planetary Science Conference Proceedings, pp. 343-353.

Longhi, J., 2003. A new view of lunar ferroan anorthosites: Postmagma ocean petrogenesis. Journal of Geophysical Research 108.

Longhi, J., 2005. Temporal stability and pressure calibration of barium carbonate and talc/pyrex pressure media in a piston-cylinder apparatus. American Mineralogist 90, 206-218.

Longhi, J., 2006. Petrogenesis of picritic mare magmas: Constraints on the extent of early lunar differentiation. Geochimica et Cosmochimica Acta 70, 5919-5934.

Lucey, P.G., 2004. Mineral maps of the Moon. Geophysical Research Letters 31.

Lyubetskaya, T., Korenaga, J., 2007. Chemical composition of Earth's primitive mantle and its variance: 1. Method and results. Journal of Geophysical Research 112.

Machida, R., Abe, Y., 2004. The evolution of an impact-generated partially vaporized circumplanetary disk. The Astrophysical Journal 617, 633.

Marsh, B., 1981. On the crystallinity, probability of occurrence, and rheology of lava and magma. Contributions to Mineralogy and Petrology 78, 85-98.

Martin, D., Nokes, R., 1989. A fluid-dynamical study of crystal settling in convecting magmas. Journal of Petrology 30, 1471-1500.

McDonough, W.F., Sun, S.-S., 1995. The composition of the Earth. Chemical geology 120, 223-253.

McKenzie, D., 1985. The extraction of magma from the crust and mantle. Earth and Planetary Science Letters 74, 81-91.

Morse, S., 1982. Adcumulus growth of anorthosite at the base of the lunar crust. Journal of Geophysical Research: Solid Earth (1978-2012) 87, A10-A18.

Nakajima, M., Stevenson, D.J., 2014. Investigation of the Initial State of the Moon-Forming Disk: Bridging SPH Simulations and Hydrostatic Models. arXiv preprint arXiv:1401.3036.

Nakamura, Y., Lammlein, D., Latham, G., Ewing, M., Dorman, J., Press, F., Toksöz, N., 1973. New seismic data on the state of the deep lunar interior. Science 181, 49-51.

Nielsen, R.L., DeLong, S.E., 1992. A numerical approach to boundary layer fractionation: application to differentiation in natural magma systems. Contributions to Mineralogy and Petrology 110, 355-369.

Norman, M.D., Borg, L.E., Nyquist, L.E., Bogard, D.D., 2003. Chronology, geochemistry, and petrology of a ferroan noritic anorthosite clast from Descartes breccia 67215: clues to the age, origin, structure, and impact history of the lunar crust. Meteoritics & Planetary Science 38, 645-661.

Nyquist, L., Bansal, B., Wooden, J., Wiesmann, H., 1977. Sr-isotopic constraints on the petrogenesis of Apollo 12 mare basalts, Lunar and Planetary Science Conference Proceedings, pp. 1383-1415.

Nyquist, L., Shih, C.-Y., 1992. The isotopic record of lunar volcanism. Geochimica et Cosmochimica Acta 56, 2213-2234.

Nyquist, L., Wiesmann, H., Bansal, B., Shih, C.-Y., Keith, J., Harper, C., 1995. 146Sm-142Nd formation interval for the lunar mantle. Geochimica et

cosmochimica acta 59, 2817-2837.

Nyquist, L.E., Shih, C.-Y., Reese, Y., Park, J., Bogard, D., Garrison, D., Yamaguchi, A., 2010. Lunar crustal history recorded in lunar anorthosites, Lunar and Planetary Institute Science Conference Abstracts, p. 1383.

O'HARA, M., Fry, N., 1996. Geochemical effects of small packet crystallization in large magma chambers—further resolution of the highly compatible element paradox. Journal of Petrology 37, 891-925.

O'neill, H.S.C., 1991. The origin of the Moon and the early history of the Earth—A chemical model. Part 1: The Moon. Geochimica et Cosmochimica Acta 55, 1135-1157.

Ohtake, M., Matsunaga, T., Haruyama, J., Yokota, Y., Morota, T., Honda, C., Ogawa, Y., Torii, M., Miyamoto, H., Arai, T., Hirata, N., Iwasaki, A., Nakamura, R., Hiroi, T., Sugihara, T., Takeda, H., Otake, H., Pieters, C.M., Saiki, K., Kitazato, K., Abe, M., Asada, N., Demura, H., Yamaguchi, Y., Sasaki, S., Kodama, S., Terazono, J., Shirao, M., Yamaji, A., Minami, S., Akiyama, H., Josset, J.L., 2009. The global distribution of pure anorthosite on the Moon. Nature 461, 236-240.

Ohtake, M., Takeda, H., Matsunaga, T., Yokota, Y., Haruyama, J., Morota, T., Yamamoto, S., Ogawa, Y., Hiroi, T., Karouji, Y., Saiki, K., Lucey, P.G., 2012. Asymmetric crustal growth on the Moon indicated by primitive farside highland materials. Nature Geoscience 5, 384-388.

Ozawa, K., Shimizu, N., 1995. Open-system melting in the upper mantle: Constraints from the Hayachine-Miyamori ophiolite, northeastern Japan. Journal of geophysical research 100, 22315-22322,22335.

Pahlevan, K., Stevenson, D.J., 2007. Equilibration in the aftermath of the lunar-forming giant impact. Earth and Planetary Science Letters 262, 438-449.

Papike, J., Fowler, G., Shearer, C., 1997. Evolution of the lunar crust: SIMS study of plagioclase from ferroan anorthosites. Geochimica et Cosmochimica Acta 61, 2343-2350.

Papike, J.J., Ryder, G., Shearer, C.K., 1998. Lunar samples. Reviews in Mineralogy and Geochemistry 36, 5.1-5.234.

Philpotts, A.R., Carroll, M., 1996. Physical properties of partly melted tholeiitic basalt. Geology 24, 1029-1032.

Presnall, D., Dixon, J., O'donnell, T., Dixons, S., 1979. Generation of mid-ocean ridge

tholeiites. Journal of Petrology 20, 3-35.

Presnall, D., Dixon, S.A., Dixon, J.R., O'donnell, T., Brenner, N., Schrock, R., Dycus, D., 1978. Liquidus phase relations on the join diopside-forsterite-anorthite from 1 atm to 20 kbar: their bearing on the generation and crystallization of basaltic magma. Contributions to Mineralogy and Petrology 66, 203-220.

Pritchard, M., Stevenson, D., 2000. Thermal aspects of a lunar origin by giant impact. Origin of the Earth and Moon 1, 179-196.

Richter, F.M., McKenzie, D., 1984. Dynamical models for melt segregation from a deformable matrix. The Journal of Geology, 729-740.

Ringwood, A., 1989. Significance of the terrestrial Mg/Si ratio. Earth and planetary science letters 95, 1-7.

Ringwood, A., Kesson, S., 1977. Basaltic magmatism and the bulk composition of the Moon. The Moon 16, 425-464.

Ringwood, A.E., 1979. Origin of the Earth and Moon. New York, Springer-Verlag New York, Inc., 1979. 307 p. 1.

Rutter, E., Neumann, D., 1995. Experimental deformation of partially molten Westerly granite under fluid‐absent conditions, with implications for the extraction of granitic magmas. Journal of Geophysical Research: Solid Earth (1978-2012) 100, 15697-15715.

Ryder, G., 1982. Lunar anorthosite 60025, the petrogenesis of lunar anorthosites, and the composition of the Moon. Geochimica et Cosmochimica Acta 46, 1591-1601.

Sakai, R., Kushiro, I., Nagahara, H., Ozawa, K., Tachibana, S., 2010. Chemical Composition of Lunar Magma Ocean Constrained by High Pressure Experiments, Lunar and Planetary Institute Science Conference Abstracts, p. 2066.

Sakai, R., Nagahara, H., Ozawa, K., Tachibana, S., 2014. Composition of the lunar magma ocean constrained by the conditions for the crust formation. Icarus 229, 45-56.

Sato, H., 2005. Viscosity measurement of subliquidus magmas: 1707 basalt of Fuji volcano. Journal of Mineralogical and Petrological Sciences 100, 133-142.

Shaw, H., 1972. Viscosities of magmatic silicate liquids; an empirical method of prediction. American Journal of Science 272, 870-893.

Shearer, C., Papike, J., 1993. Basaltic magmatism on the Moon: A perspective from volcanic picritic glass beads. Geochimica et Cosmochimica Acta 57, 4785-4812.

Shih, C.-Y., 1977. Origins of KREEP basalts, Lunar and Planetary Science Conference

Proceedings, pp. 2375-2401.

Simura, R., Ozawa, K., 2006. Mechanism of crystal redistribution in a sheet-like magma body: constraints from the Nosappumisaki and other shoshonite intrusions in the Nemuro peninsula, Northern Japan. Journal of Petrology 47, 1809-1851.

Simura, R., Ozawa, K., 2011. Magmatic Fractionation by Compositional Convection in a Sheet-like Magma Body: Constraints from the Nosappumisaki Intrusion, Northern Japan. Journal of Petrology 52, 1887-1925.

Smith, J.V., Anderson, A.T., Newton, R.C., Olsen, E.J., Crewe, A.V., Isaacson, M.S., Johnson, D., Wyllie, P.J., 1970. Petrologic history of the moon inferred from petrography, mineralogy and petrogenesis of Apollo 11 rocks. Geochimica et Cosmochimica Acta Supplement 1, 897.

Smith, P.M., Asimow, P.D., 2005. Adiabat_1ph: A new public front-end to the MELTS, pMELTS, and pHMELTS models. Geochemistry Geophysics Geosystems 6, Q02004.

Snyder, G.A., Taylor, L.A., Neal, C.R., 1992. A chemical model for generating the sources of mare basalts: Combined equilibrium and fractional crystallization of the lunar magmasphere. Geochimica et Cosmochimica Acta 56, 3809-3823.

Solomatov, V., 2000. Fluid dynamics of a terrestrial magma ocean. Origin of the Earth and Moon 1, 323-338.

Solomatov, V.S., 1995. Batch crystallization under continuous cooling: Analytical solution for diffusion limited crystal growth. Journal of crystal growth 148, 421-431.

Solomatov, V.S., Olson, P., Stevenson, D.J., 1993. Entrainment from a bed of particles by thermal convection. Earth and planetary science letters 120, 387-393.

Solomatov, V.S., Stevenson, D.J., 1993. Nonfractional crystallization of a terrestrial magma ocean. Journal of Geophysical Research 98, 5391-5406.

Solomon, S., Chaiken, J., 1976. Thermal expansion and thermal stress in the moon and terrestrial planets-Clues to early thermal history, Lunar and Planetary Science Conference Proceedings, pp. 3229-3243.

Solomon, S., Longhi, J., 1977. Magma oceanography: I. Thermal evolution, Lunar and Planetary Science Conference Proceedings, pp. 583-599.

Spera, F.J., 1992. Lunar magma transport phenomena. Geochimica et cosmochimica acta 56, 2253-2265.

Tait, S., Jaupart, C., 1989. Compositional convection in viscous melts.

Takahashi, E., 1986. Melting of a dry peridotite KLB‐1 up to 14 GPa: Implications on the Origin of peridotitic upper mantle. Journal of Geophysical Research: Solid Earth (1978-2012) 91, 9367-9382.

Taylor, S., Bence, A., 1975. Evolution of the lunar highland crust, Lunar and Planetary Science Conference Proceedings, pp. 1121-1141.

Taylor, S.R., 1982. Planetary science: A lunar perspective. Lunar and Planetary Institute Houston, Texas.

Taylor, S.R., Jakes, P., 1974. The geochemical evolution of the Moon, Lunar and Planetary Science Conference Proceedings, pp. 1287-1305.

Taylor, S.R., Pieters, C.M., MacPherson, J.G., 2006a. Earth-Moon System, Planetary Science, and Lessons Learned. Reviews in Mineralogy and Geochemistry 60, 657-704.

Taylor, S.R., Taylor, G.J., Taylor, L., 2006b. The moon: a Taylor perspective. Geochimica et cosmochimica acta 70, 5904-5918.

Tonks, W.B., Melosh, H.J., 1990. The physics of crystal settling and suspension in a turbulent magma ocean. Origin of the Earth 1, 151-174.

Van Orman, J.A., Grove, T.L., 2000. Origin of lunar high-titanium ultramafic glasses: Constraints from phase relations and dissolution kinetics of clinopyroxene-ilmenite cumulates. Meteoritics and Planetary Science 35, 783-794.

Wada, K., Kokubo, E., Makino, J., 2006. High-resolution simulations of a Moon-forming impact and postimpact evolution. The Astrophysical Journal 638, 1180.

Wänke, H., Dreibus, G., 1994. Chemistry and accretion history of Mars. Philosophical Transactions of the Royal Society of London. Series A: Physical and Engineering Sciences 349, 285-293.

Warren, P.H., 1985. The magma ocean concept and lunar evolution. Annual Review of Earth and Planetary Sciences 13, 201-240.

Warren, P.H., 1990. Lunar anofthosites and the magma-ocean plagioclase-flotation hypothesis: Importance of FeO enrichment in the parent magma. American Mineralogist 75, 46-58.

Warren, P.H., 1993. A concise compilation of petrologic information on possibly pristine nonmare Moon rocks. American Mineralogist 78, 360-376.

Warren, P.H., 2005. “New” lunar meteorites: Impact melt and regolith breccias and large‐scale heterogeneities of the upper lunar crust. Meteoritics & Planetary Science 40,

989-1014.

Warren, P.H., Haack, H., Rasmussen, K.L., 1991. Megaregolith insulation and the duration of cooling to isotopic closure within differentiated asteroids and the Moon. Journal of Geophysical Research: Solid Earth (1978-2012) 96, 5909-5923.

Warren, P.H., Wasson, J.T., 1979. The origin of KREEP. Reviews of Geophysics 17, 73-88.

Wasson, J., Wetherill, G., 1979. Dynamical chemical and isotopic evidence regarding the formation locations of asteroids and meteorites. Asteroids 1, 926-974.

Wasson, J.T., 1985. Meteorites: Their record of early solar-system history. New York, WH Freeman and Co., 1985, 274 p. 1.

Wasson, J.T., 1988. The building stones of the planets. Mercury, 622-650.

Wieczorek, M.A., Jolliff, B.L., Khan, A., Pritchard, M.E., Weiss, B.P., Williams, J.G., Hood, L.L., Righter, K., Neal, C.R., Shearer, C.K., 2006. The constitution and structure of the lunar interior. Reviews in mineralogy and geochemistry 60, 221-364.

Wieczorek, M.A., Neumann, G.A., Nimmo, F., Kiefer, W.S., Taylor, G.J., Melosh, H.J., Phillips, R.J., Solomon, S.C., Andrews-Hanna, J.C., Asmar, S.W., 2013. The crust of the Moon as seen by GRAIL. Science 339, 671-675.

Wieczorek, M.A., Zuber, M.T., 2001. The composition and origin of the lunar crust: Constraints from central peaks and crustal thickness modeling. Geophysical Research Letters 28, 4023-4026.

Wilshire, H., Schaber, G., T SILVER, L., Phinney, W., D JACKSON, E., 1972. Geologic setting and petrology of Apollo 15 anorthosite (15415). Geological Society of America Bulletin 83, 1083-1092.

Wood, J.A., Dickey Jr, J., Marvin, U.B., Powell, B., 1970. Lunar anorthosites and a geophysical model of the moon. Proc. Apollo 11 Lunar Sci. Conf., 965-988.

Zhong, S., Parmentier, E., Zuber, M.T., 2000. A dynamic origin for the global asymmetry of lunar mare basalts. Earth and Planetary Science Letters 177, 131-140.